Research on optical properties of porous materials activated by luminescence centers

Sa chu rong gui

(Degree)
博士（工学）

(Date of Degree)
2014-03-25

(Date of Publication)
2015-03-01

(Resource Type)
doctoral thesis

(Report Number)
甲第6086号

(URL)
https://hdl.handle.net/20.500.14094/D1006086

Doctoral Dissertation

Research on optical properties of porous materials activated by luminescence centers

発光センタをドーピングした多孔質材料の光学特性に関する研究

January, 2014

Graduate School of Engineering

Kobe University

Sa chu rong gui

Contents

Chapter 1

Introduction

1.1 Porous materials

1.1.1 Porous silicon thin films

1.1.1.1 Why porous silicon thin film

Porous silicon (Si) is a three dimensional network of Si nanocrystals, which is first discovered by Uhlir in 1956 [1]. Since porous Si is compatible with Si processes, it is known to be the most important material in Si based photonics. Since the discovery of multicolor room temperature emission from nanoporous Si, porous Si has further evoked intense interest [2-4]. The emission wavelength can be extended to the near infrared region by thermal oxidation. However, the emission hardly covers the optical telecommunication wavelengths (from 1.0 to 1.6 μm) [5]. In general, luminescence center doping is an effective way to extend the application in communication technology. Porous Si is a very suitable host material for luminescence center doping because it consists of many open pores, and has large surface area. Luminescence centers can be doped very easily during or after the growth of porous Si. Another important advantage of porous Si as a host is ability to sensitize luminescence centers.

On the other hand, thin film integrated optics are becoming more and more important in optical communication technology. The technology for the fabrication of passive devices such as planar optical waveguides is well developed [6]. One next step is the development of waveguide optical amplifiers that can be integrated in passive devices. Since the refractive index of porous Si can be changed over a wide range by controlling the porosity, waveguide interconnection can be produced by porous Si. Recently, rare earth ions doped porous Si has attracted great interest as a candidate material for waveguide optical amplifier [7,8]. For example, Er^{3+} doped porous Si shows emission at 1530 nm, the wavelength coincides well with the low loss window of silica based optical fibers. However, with the rapid development

of the optical fiber communication networks in recent years, broader gain bandwidth in the telecommunication window is required. Very recently, Fujimoto and Nakatsuka [9] reported a novel infrared luminescence from bismuth (Bi) doped silica-based glasses ranging from 1.0 μm to 1.6 μm. Since the report of optical amplification in Bi doped silica glass, Bi doped various materials have been intensively studied [10-16]. In first part of this work, we focus on porous Si as a host material to study the optical properties of Bi-doped oxidized porous Si thin films for developing a broadband optical amplifier at the telecommunication wavelengths. This part summarizes the optical properties of porous Si based on the past reports, and then elucidates the purpose of this work.

1.1.1.2 Preparation of porous silicon

Generally, porous Si is prepared by electrochemical anodisation (electrochemical etching) of bulk Si wafers in a solution of aqueous or ethanoic hydrofluoric acid (HF). Schematic diagram of porous Si formation set up was shown in Figure 1.1. By contacting the anodizing electrolyte, the porous Si is only formed on the surface of Si wafer. During the past years, several mechanisms for pore formation in Si substrate have been proposed [17,18]. Figure 1.2 shows a proposed porous Si formation mechanism by Lehmann and Gösele [18]. During the anodisation process, the positively charged Si surface is oxidized by F^- ions followed by the formation SiF_6^{2-} and $2H^+$ complex. After the anodisation, ethanol is added to remove the H_2 bubbles from the sample surface. Various kinds of porous Si can be simply prepared by controlling the preparation conditions, such as type of Si wafer, HF concentration and the acidity (PH value) in anodisation solution, the anodisation current density and anodisation time, and so on [19-22].

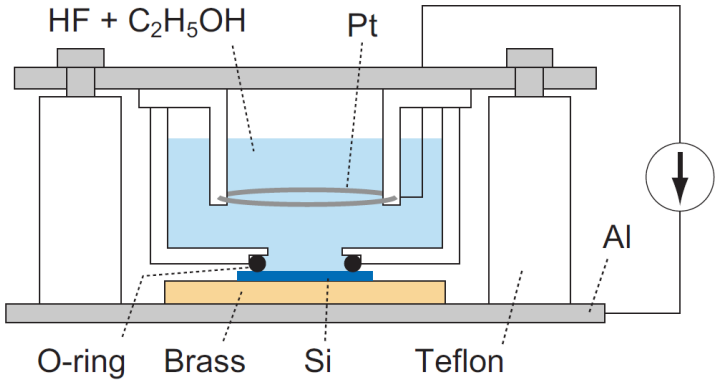

Figure1.1: Anodisation cell used for the fabrication of porous Si thin film.

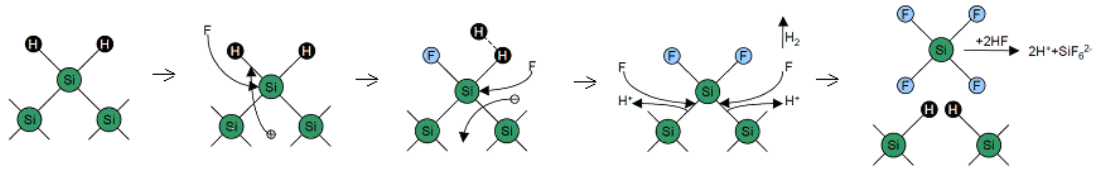

Figure1.2: Suggested mechanism for the electrochemical dissolution of Si [18].

1.1.1.3 Morphology of porous silicon

During the past years, the microstructure of porous Si has been widely studied by many groups by means of microscopy techniques [19-24]. The pore type, pore size, porosity and porous thickness are known to be the main structural parameters of the porous Si. Based on the size of pores in porous Si, porous Si can be divided into three categories: microporous (less than 2 nm), mesoporous (between 2 to 50 nm), and macroporous (larger than 50 nm). To study the structure of porous Si, field emission- scanning electron microscopy (FE-SEM), transmission electron microscopy (TEM), atomic force microscopy (AFM) measurements etc are commonly used. As shown in Figure 1.3, detailed information about pore size and morphology can be seen from the cross-sectional SEM image [25].

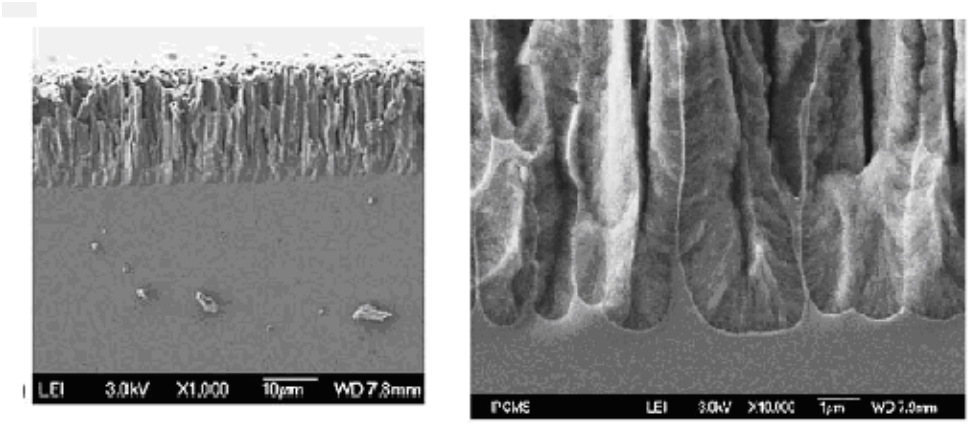

Figure 1.3: Cross sectional SEM image of porous Si [25].

Furthermore, the surface structure of oxidized porous Si was observed by TEM in our group [26]. Figure 1.4 shows (a) plain-view TEM images of as-prepared porous Si and plain-view TEM images of porous Si oxidized at (b) 800 ^{o}C, (c) 900 °C and (d) 1000 °C. In Figure 1.4, the dark regions correspond to porous Si skeletons, while the bright regions correspond to pores. We can see that the pore size (diameter of the pores) is several tens of

nanometers. The pore size decreases with increasing annealing temperatures. When annealed at the highest temperature, that is, 1000 ^{o}C, although pores still remain, the size is much smaller than that in the as-prepared sample.

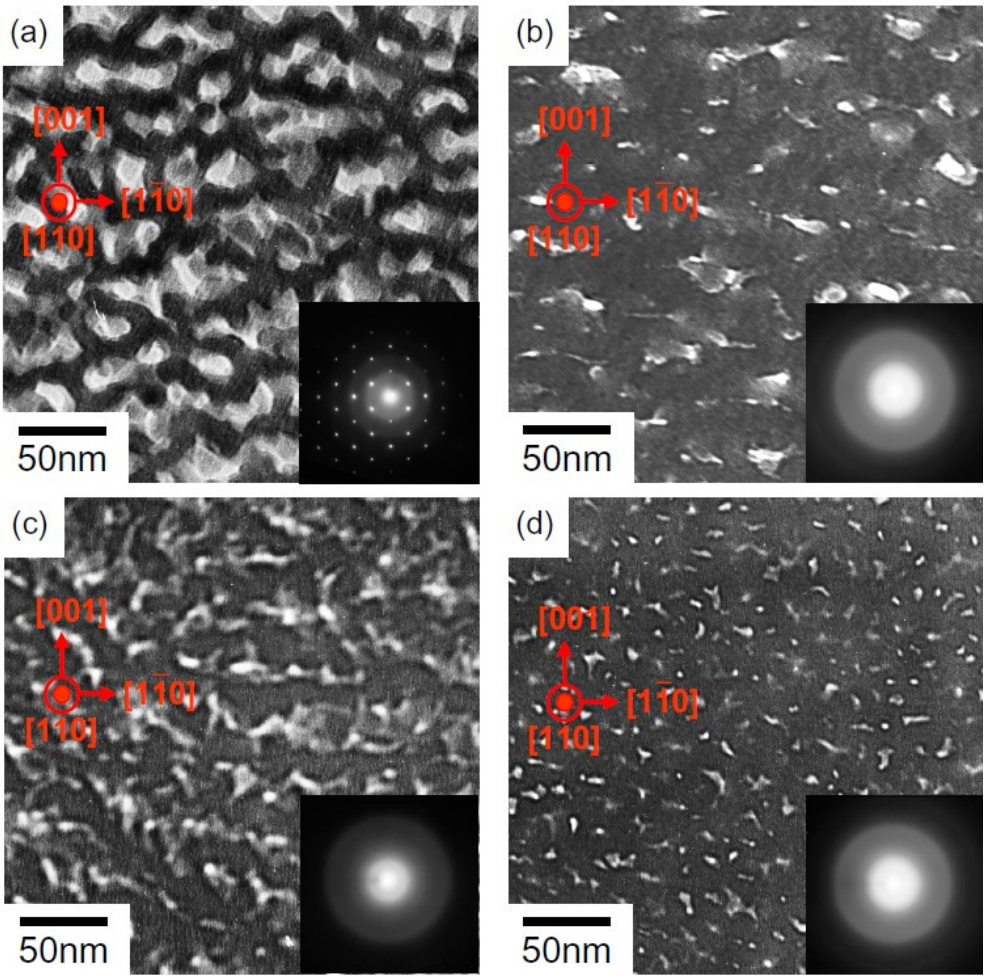

Figure 1.4: (a) Cross-sectional and (b) plain-view TEM images of as-prepared porous Si *and plain-view TEM images of* porous Si *oxidized at (c) 900 °C and (d) 1000 °C [26].*

1.1.1.4 Luminescence of porous silicon

Since the first report on the room temperature luminescence in the visible range by L. T. Canham in 1990, porous Si has evoked much interest [27]. After then, further study on the luminescence properties by the group indicated that porous Si contains quantum size crystalline structures responsible for the visible emission [28]. Recently, luminescence properties of porous Si are widely investigated. Usually, porous Si is terminated with Si–H bonds. Due to the weak bonding in the hydrogen termination, non-radiative defect centers can be formed under light illumination, making porous Si not so stable. One way to solve the problem is thermal oxidation or electrochemical oxidation [5, 29, 30].

Porous Si shows near infrared (NIR) luminescence after thermal treatment. Photoluminescence (PL) properties of porous Si at the oxidation temperature from 0 to 1200 ^{o}C were investigated by Nakamura et al. [5]. It was found that NIR luminescence can be observed in the high temperature annealed oxidized porous Si. As shown in Figure 1.5, the peak position and intensity of the oxidized porous Si strongly depend on the oxidation temperature. Visible luminescence is observed in the as prepared sample and the samples annealed at low temperature. The PL intensity in the NIR region is steeply quenched after annealing at 300 ^{o}C, and recovered at above 700 ^{o}C. XPS measurement suggests that the formation of thick high-quality SiO_2 layer under high temperature annealing results in the PL intensity recovery. It is concluded that the thickness and quality of SiO_2 layer play a crucial role in the PL properties of the thermally oxidized porous Si.

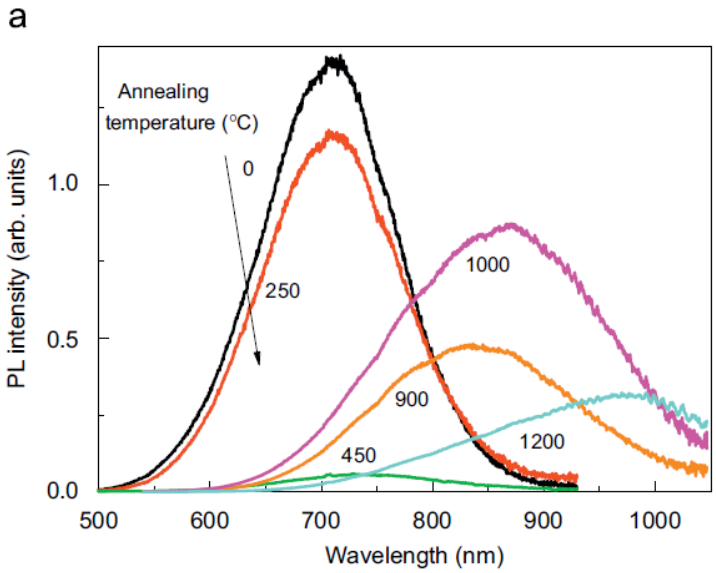

Figure 1.5: PL spectra of the porous Si powders oxidized from 0 to 1200 ^{o}C [5].

1.1.1.5 Applications of porous silicon

Various excellent characteristics of porous Si have given rise to a variety of potential applications, such as Si-on-insulator (SOI), light emitting diodes (LEDs), waveguide and so on. A full wafer SOI structure based on porous Si can be easily formed. For example, a porous Si layer is prepared in a Si wafer and thereafter is anodically oxidized in the same cell for the preparation of the porous layer using an oxidant electrolyte solution without HF. The anodic oxidation can lead to the formation of an oxide layer located only at the bottom of the porous layer, the result being a structure porous Si/ anodic oxide/Si substrate. A following

high temperature annealing can densify the anodic oxide and introduce re-crystallization of the remaining porous Si layer. The process lead to an SOI structure [31-33]. During the 1980's, many research on porous Si were carried out to develop SOI technology for device isolation in integrated circuits. A method is based on the oxidized porous Si to isolate pre-defined islands of crystalline Si from the bulk Si substrate. Compared to conventional methods, the full isolation by oxidized porous Si method offered the advantages of higher speed, lower power consumption, higher packing density and a reduced number of fabrication steps [34]. Another advantage is the simplicity of processing and low leakage current [35].

LEDs based on Si would find many applications, such as very large scale integration and display technology. However, Si normally shows only very weak infrared luminescence. Since the discovery of multicolor visible luminescence from porous Si, it has generated much interest. In 1990's many porous Si LEDs were proposed [36-38]. L. Pavesi et al demonstrated a porous Si LED based on a resonant planar microcavity [36]. They found that the porous Si LED offered a few advantages compare to conventional LED: higher efficiency, narrower band emission, higher directionality of the emission pattern, and higher stability.

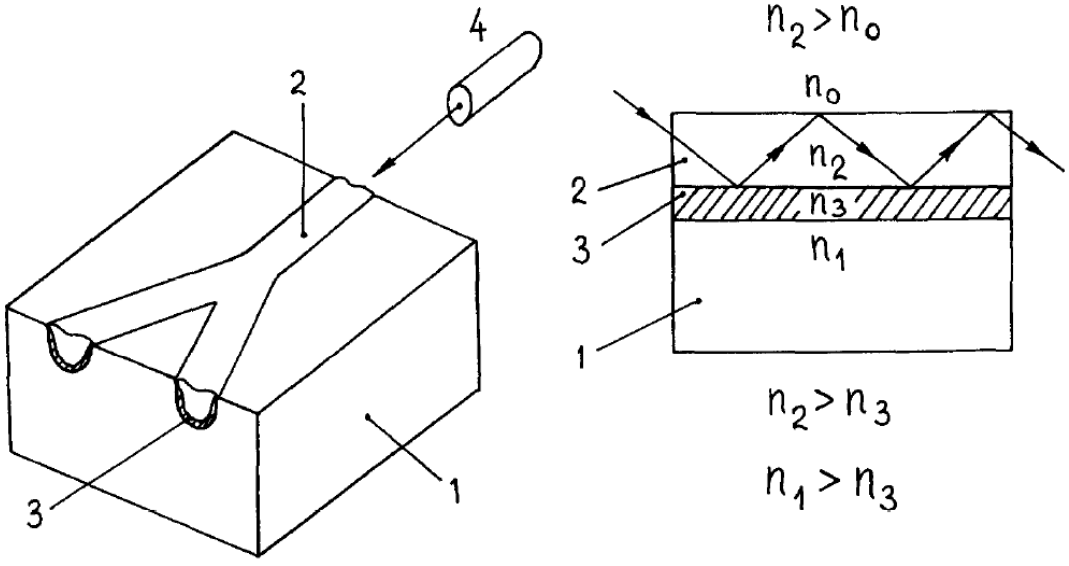

Figure 1.6: Schematic view of optical waveguide based on oxidized porous Si. 1 - Si substrate; 2 - oxidized porous Si; 3 - Si oxide layer; 4 - light source [39].

Since the refractive index of porous Si can be tuned in wide range, by varying the porosity, it is worth considering the material to form waveguide interconnects. In 1995, optical waveguiding has been observed in oxidized porous Si on SiO_2 isolating layer on Si substrate. The schematic view of the optical waveguide based on oxidized porous Si is shown in Figure

1.6 [39]. Since then, many approaches to manufacture active porous Si layers based waveguides operating from visible to infrared wavelengths have been demonstrated [39-42]. In Ref. [42] it was found that it is possible to produce integrated optical waveguides based on oxidized porous Si. The fabrication process is compatible with the traditional Si technology and consists of the formation of local layers of porous Si followed by thermal oxidation of the layers. Active waveguide devices in telecommunication wavelengths can be obtained by introducing luminescence centers into the waveguide channel. Er^{3+} is of special interest for this purpose, since its main emission band with peak wavelength at 1530 nm corresponds to minimum loss of the quartz fiber [40,41,43]. Recently, Er^{3+} doped oxidized porous Si waveguides were extensively investigated, an optical losses and internal gain in Er doped porous Si waveguide reached 2dB/cm and 5.8 dB/cm at a pumping power of 65 mW, respectively [40]. The gain is much larger than that in Er^{3+} doped Si rich silica waveguide (0.58 dB/cm) at low power pumping [44]. In first part of this work, the broadband NIR luminescence from Bi doped oxidized porous Si thin film is studied, aiming for its potential application in broadband optical waveguide amplifier at optical telecommunication wavelengths.

1.1.2 Zeolites

1.1.2.1 Why zeolite

Zeolite is a highly crystalline porous material, which has many excellent features, such as microporous uniformity, structural symmetry, and topological variety. These properties result in high surface areas, thermal stability, and the ability to sieve molecules based on size and shape-selectivity. Zeolites have been widely used in applications such as gas separation and selectively absorption, ion exchange, catalysis, and have been suggested for use as chemical sensors, membrane reactors, and low dielectric constant materials for semiconductors.

The porous structure and large surface areas of zeolites enable them to act as hosts for molecules and ions or as templates for nanostructures synthesis [45]. Recently, zeolites acting as host materials for luminescence centers have attracted considerable attention for constructing functional materials designed at nanosized levels. Luminescence centers (rare earth (RE) ions, Bi, and so on) can be simply doped in zeolite by a simple ion exchanging. Optically activated zeolites show various potential applications, such as fiber amplifiers, LEDs, biological probes, lighting, laser materials, and so on [46-49]. In addition, zeolite is one of the most suitable host materials for the formation of metal clusters. Metal clusters are known to be chemically stable in the nano-sized pores in the cage, and can be formed by a simple ion exchange process followed by a thermal treatment. In second part of this work,

photosensitization of RE ions by silver clusters/ions in zeolites is studied. This part summarizes the optical properties of zeolite based on past reports, and then elucidates the purpose of this work.

1.1.2.2 Structure

Zeolites are aluminoslilicate crystalline nanoporous material with small pores (1-20 Å diameter). The aluminosilicate framework consists of corner sharing orthosilicate (SiO_4) and orthoaluminate (AlO_4) tetrahedra units by sharing oxygen between every two consecutive units, and cations located inside channels or cavities to balance negative charges in the framework [50]. Zeolite is defined as crystalline structure due to its regular porous shape and size. Zeolites can be prepared with a wide range of shapes and pores size, and the composition can be modified during preparation, in order to tailor the properties. Zeolites also can be prepared with various silica to alumina ratios, but the constraints are that the sum of the number of Si atoms and the number of Al atoms equals 192 and that the total charge of the cations equals the number of Al atoms [51,52].

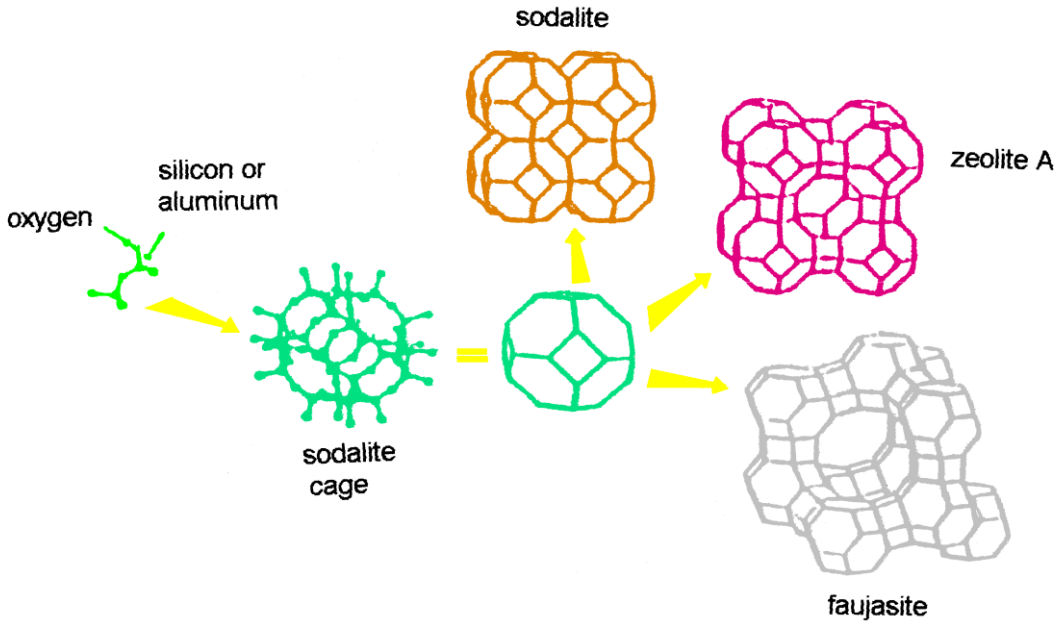

Figure 1.7: basic building block of zeolite [53].

As shown in Figure 1.7, the sodalite cage (or β cage) is known to be the basic building block of zeolites [53]. The sodalite cage has both four-membered and six-membered rings in its structure. By fusing together the four-membered rings, sodalite is formed and which is a naturally occurring material. By bridging the four-membered rings, zeolite A is formed. This

does not occur in nature, but is industrially produced on a massive scale. If the six-membered rings are bridged (prism), then possibly the most important zeolite structure, zeolite X and Y (faujasite (FAU) type zeoltie) is formed. The X and Y are divided by the ratio of silicon/aluminum. This structure has very large microporous spaces, allowing organic molecules to diffuse in and out. Another important class is the pentasil zeolites, named so because they are constructed of five-membered rings. The most important example is that of ZSM-5. FAU type zeoltie is one of the most widely used zeolite (Figure 1.8 (a)). The diameter of the entrance to the supercage is about 7.5 Å, whereas the diameter of the supercage itself is about 12 Å. In contrast, the diameter of the sodalite cage is 6.6 Å and that of the hexagonal prism is 1.8 Å. On the other hand, zeolite A exhibits the LTA (Linde Type A) structure (Figure 1.8 (b)). It has a 3-dimensional pore structure with pores running perpendicular to each other in the x, y, and z planes. The pore diameter is defined by an eight member oxygen ring and is small at 4.2 Å. This leads to a larger cavity of minimum free diameter of 11.4 Å (diameter of supercage). Zeolite A has a void volume fraction of 0.47, with a Si/Al ratio of 1.0. The water molecules in the zeolite structure can be removed by dehydration and their number is variable [45]. Actually, a typical feature of zeolites is that they can absorb and lose water without damage to their crystal structures.

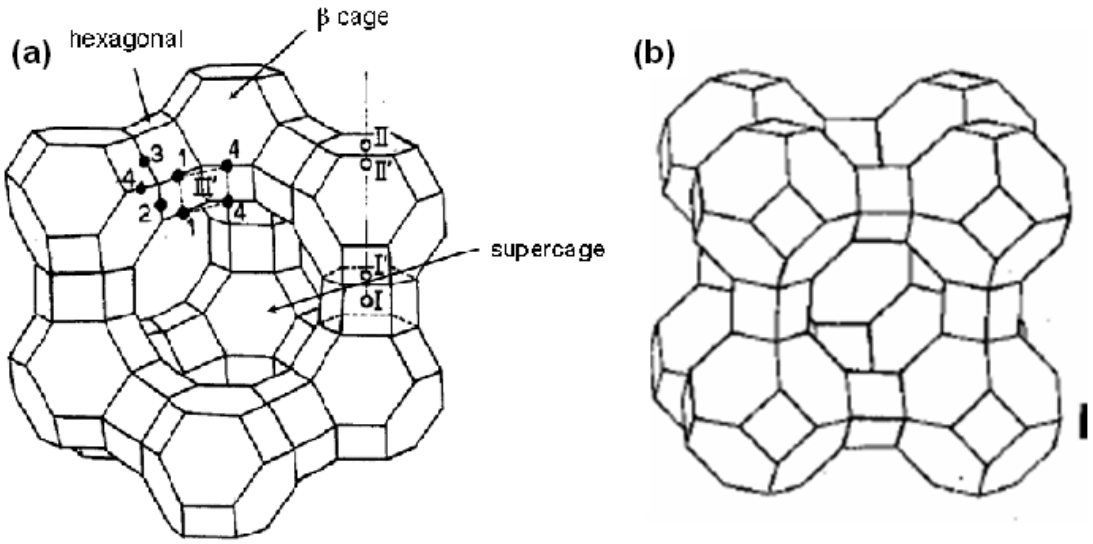

Figure 1.8: Structure of FAU type (a) and LTA type (b) zeolite [54].

1.1.2.3 Applications

Zeolites have uniform pore dimensions, high internal surface area, ion exchange ability, and high thermal stability. These properties make zeolites unique among other inorganic oxides. Zeolites have been accepted in a variety of applications, such as separation, catalysis

and ion exchange [53-57]. The porous structure enables the zeolites to selectively admit some molecules while excluding those that are too large to fit into the pores. This leads to its molecular sieve properties. Zeolite as a molecular sieve was derived by McBain in 1932 [55]. The dimensions of zeolites' channels and their ability to adsorb gases and water have made zeolite molecular sieves suitable for a number of applications such as in the areas of refinery fuel processing, production of chemicals and environmental pollution control [56,57].

Zeolites are also known as a shape selective catalyst. The possible shape selectivity of zeolites was illustrated in Figure 1.9. There are reactant selectivity, product selectivity and transition selectivity [53]. On the other hands, efficient optical properties of optically activated zeolites show various potential applications, such as fiber amplifiers, LEDs, biological probes, lighting, laser materials, and so on. In second part of this work, the photosensitization of RE ions by Ag clusters/ions in zeolites is studied, aiming for its potential application in white LEDs.

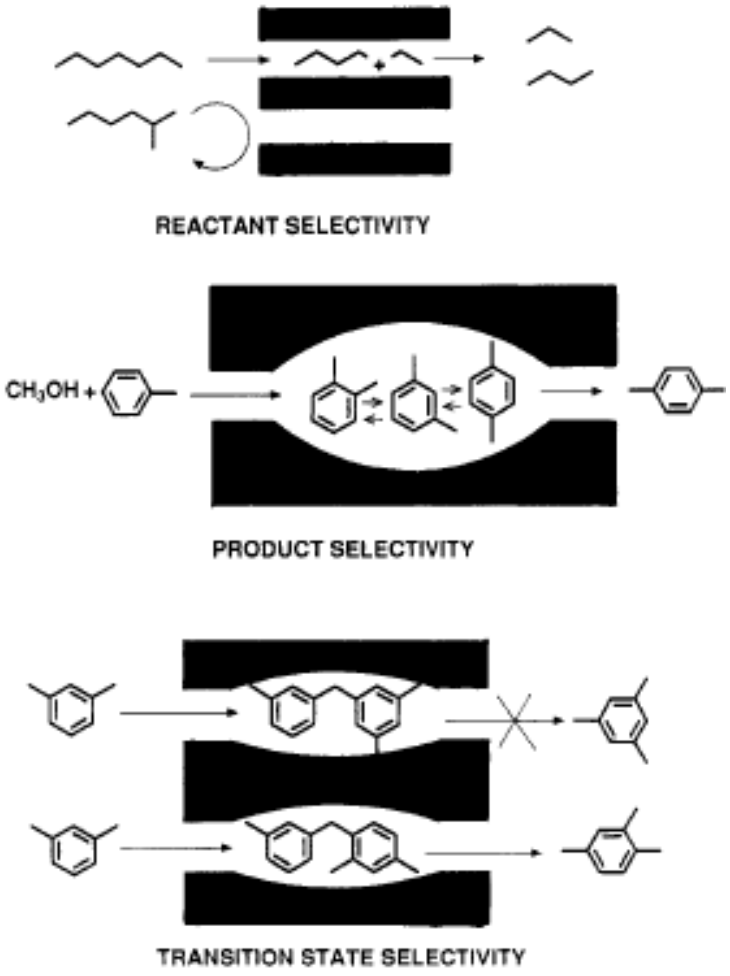

Figure 1.9: Schematic illustrations of shape selectivity exhibited by zeolites [53].

1.2 Luminescence centers in porous materials

1.2.1 Near infrared luminescence of Bi and rare earth ions in porous materials

1.2.1.1 NIR PL of rare earth ions in porous silicon

One of the most considered host material is Si because of its relevance in the microelectronic and telecommunications industries. A promising alternative to the conventional Si doping procedures is to use porous Si layers as host. The large surface area allows the penetration of the luminescence centers into the matrix and the oxidation of the porous layers, which are necessary for the ion activation [58-61]. Porous Si is a very suitable host material for RE ions to utilize the sensitization effect of Si-ncs because it consists of many open pores. RE ions can be doped very easily during the growth of porous Si and also after the growth. Several doping techniques such as ion implantation [58], spin-on [59], dip coating [60] and electrochemical [61] methods were used to incorporate RE ions into porous Si.

Recently, Er^{3+} doped porous Si has been studied intensively because the luminescence wavelength exactly coincides with the optical telecommunication wavelength [39-43]. Thus, Er^{3+} doped porous Si waveguide has been extensively investigated for optical amplifier applications. It shows many advanced properties, such as broad range of light transmission; porous Si makes Er^{3+} to be optically active; technology of Er^{3+} doped oxidized porous Si waveguides is compatible with standard Si microelectronic technology [39-43]. For example, V. P. Bondarenko [39] et al. investigated Er^{3+} doped oxidized porous Si for integrated optical waveguides, indicating that electrochemical deposition of Er in porous Si following the oxidation of the porous layer makes it possible to introduce Er into the core of the waveguide channel and preserve the waveguide properties of oxidized porous Si. It was also shown that Er^{3+} in the waveguide was in optically active state. PL at 1532 nm from Er^{3+} in optical waveguides can be observed by light pumping. Afterwards M. Balucani et al. reported Er-doped channel oxidized porous Si waveguides prepared from n-type Si by two-step anodisation process [43]. It is found that the Er^{3+} doped oxidized porous Si waveguides can achieve the amplification effect by optimizing Er^{3+} concentration and refractive index of porous Si. These indicate that porous Si provides the possibility of fabricating a small size optical amplifier which can be integrated in thin film optical devices.

1.2.1.2 NIR PL of Bi in porous materials

The two useful wavelengths for optical communication in Si based material were shown in the Figure 1.10. One is minimum dispersion region of silica glass fiber at 1300 nm, the other is the maximum transparency wavelength of silica glass fiber at 1540 nm [62,63]. A

method to solve the problem of lacking efficient silicon-based light source in optoelectronic integration on Si is luminescence centers doping. Considerable works have been contributed to develop optical fiber amplifiers to revolutionize the telecommunication systems, such as Erbium doped fiber amplifiers, Ytterbium doped fiber amplifiers, thulium doped fiber amplifiers, Praseodymium doped fiber amplifiers, and so on.

With the rapid development of the optical fiber communication networks in recent years, the wavelength division multiplexing system demands fiber amplifiers with broader gain bandwidth in the telecommunication window. The gain bandwidth of RE doped fiber amplifier is less then 100 nm, due to the restriction of the forbidden f-f transition. Great efforts have been devoted to explore and synthesize new gain media which possess much broader luminescence bands than conventional rare earth ions doped gain media [64-66]. One successful example is Bi doped silica-based glasses. Broad NIR luminescence from Bi in silica glass was first discovered by Murata et al. in 1956. Since realization of optical amplification in the 1.0 to 1.6 μm region in Bi doped silica-based glasses by Fujimoto and Nakatsuka in 2003, Bi doped silica-based glasses have attracted great attention [66]. As shown in Figure 1.11, the NIR emissions of Bi in silicate glass cover whole telecommunication wavelengths [67].

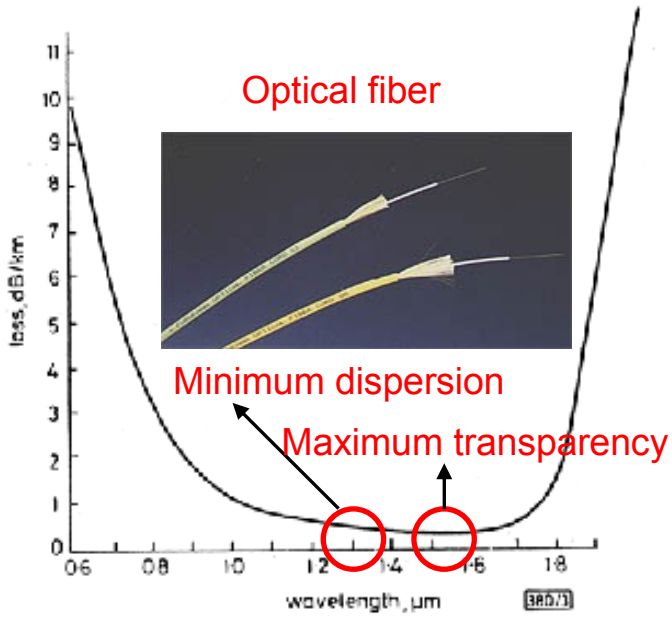

Figure 1.10: Optical loss of silica glass fiber [62,63].

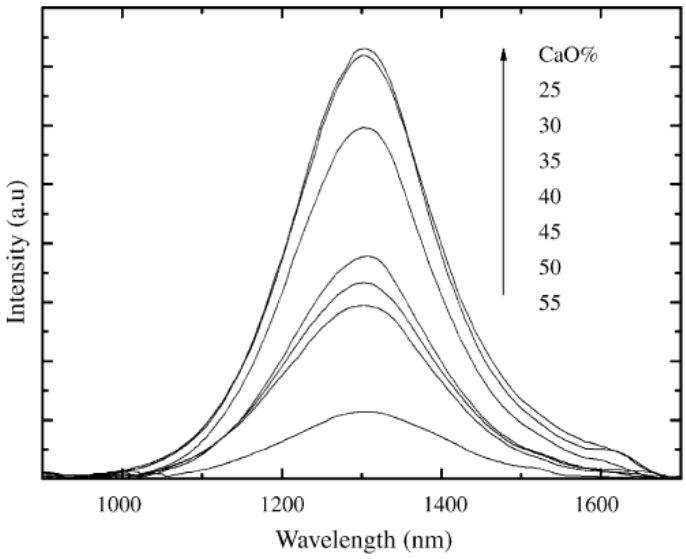

Figure 1.11: NIR emission spectra of Bi-doped silicate glass [67].

Recently, tremendous research on NIR luminescence from Bi ion has been carried out in different host materials, such as glasses, crystals, ionic liquids, optical devices, and so on [66-70]. Very recently, the family of Bi doped material is extended to porous materials: such as zeolite and porous glass [47, 70-78]. For example, Bi doped zeolites are intensively investigated by our group [71-75]. Bi doped zeolite is simply prepared by an ion-exchange process and subsequent high-temperature annealing under Ar atmospheric conditions [47]. As shown in Figure 1.12, the Bi doped high silica zeolite (FAU type) shows strong, air-stable, long-lived, ultra-broadband (with a FWHM larger than 160 nm) NIR luminescence. The PL covers the whole telecommunication windows of O (1260–1360 nm), E (1360–1460 nm), and S (1460–1530 nm) bands, and even the C (1530–1565 nm) and L (1565–1625 nm) bands, being much broader than those of RE ions. They find that the NIR PL displays spectral tunability by tailoring the excitation wavelength, and the PL intensity significantly depends on the annealing temperature. Owing to the excellent optical properties of these activated zeolites and the mature zeolite assembly techniques developed, they suggested that these materials are promising for applications as the active media of broadly tunable micro- or nano-optical sources and devices. Further investigations of the Bi doped zeolite indicated that intensity and lifetime of the Bi NIR PL can be tuned by Bi concentration and co-dopant of Al [74,75].

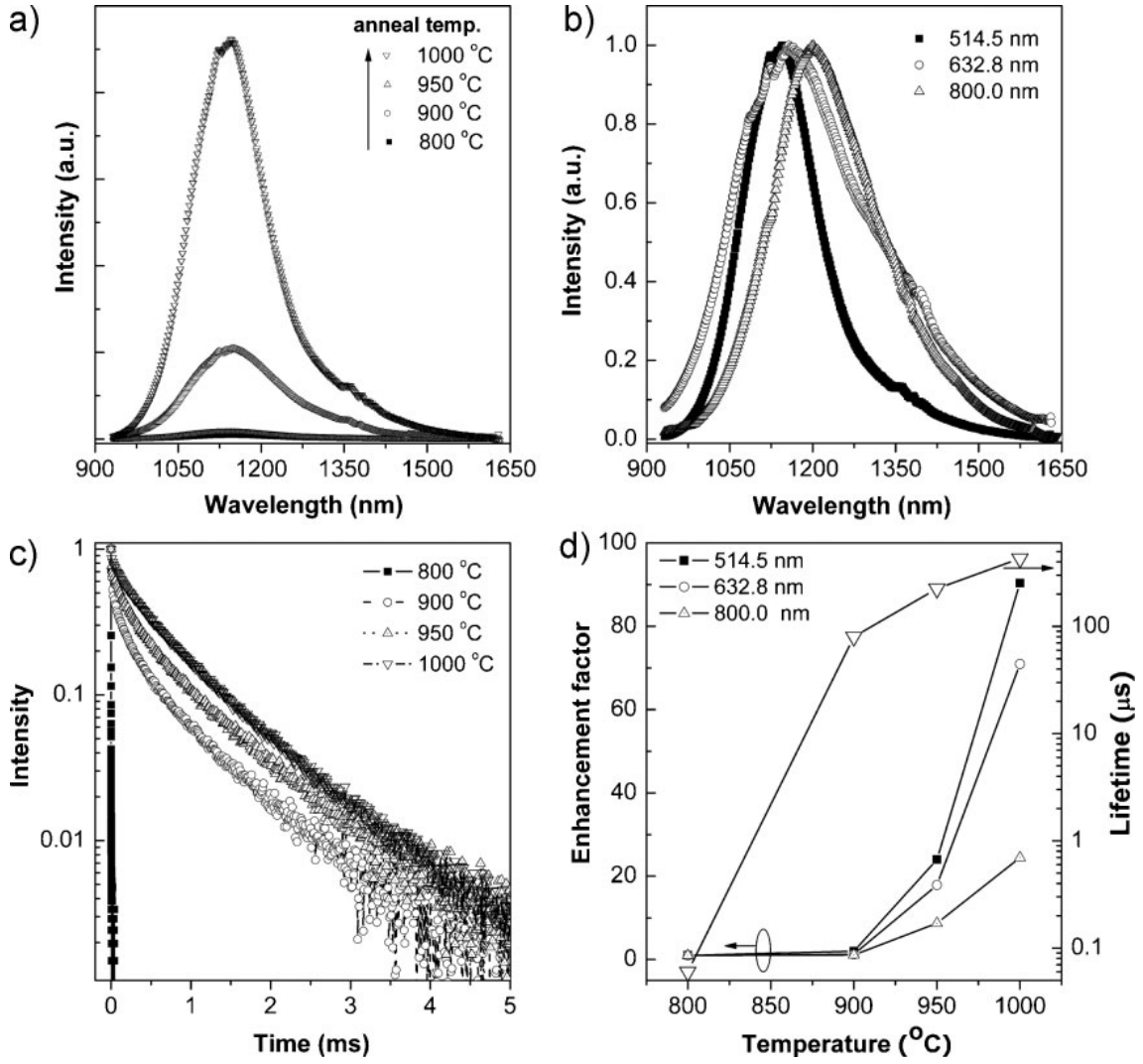

Figure 1.12: a) Ultra-broadband NIR PL spectra of zeolites annealed at the indicated temperatures in an Ar atmosphere, which were excited by the 514.5nm line of an Art laser. b) Normalized NIR PL of the sample annealed at 1000 °C under 514.5, 632.8, and 800 nm excitation. c) Fluorescence-decay curves of the annealed samples at room temperature. d) Left axis: annealing temperature dependence of enhancement factor of PL when excited at 514.5, 632.8, and 800 nm. Enhancement factors at different excitation wavelengths were calculated by dividing integrated PL intensities at different temperatures by that at 800 oC. Right axis: temperature dependence of 1/e lifetime at 1145 nm [47].

On the other hands, the NIR PL of Bi was reported in alumino-silicate nanoporous glass. Luminescence from blue-green, to orange, red, and even to ultra-broadband infrared (IR)

luminescence were observed in the Bi doped nanoporous glass thermally treated in Ar atmosphere [76]. As shown in Figure 1.13, both the visible and the IR luminescence significantly depend on the excitation wavelengths. The author suggested that the multicolored nanoporous glass can be potential wide-spectrum light source. For many years, it is believed the introduction of extra elements such as Al is indispensable to obtain NIR emission from Bi-doped silica glasses [66, 68]. However, very recently Razdobreev et al. [77] demonstrated that Bi doped pure porous silica glass can exhibit broadband NIR luminescence. The experimental results reveal the existence of at least two different types of Bi NIR active centers and clearly demonstrate that the presence of other dopant in the glass matrix is not necessary to obtain the NIR PL from Bi in silicate glass.

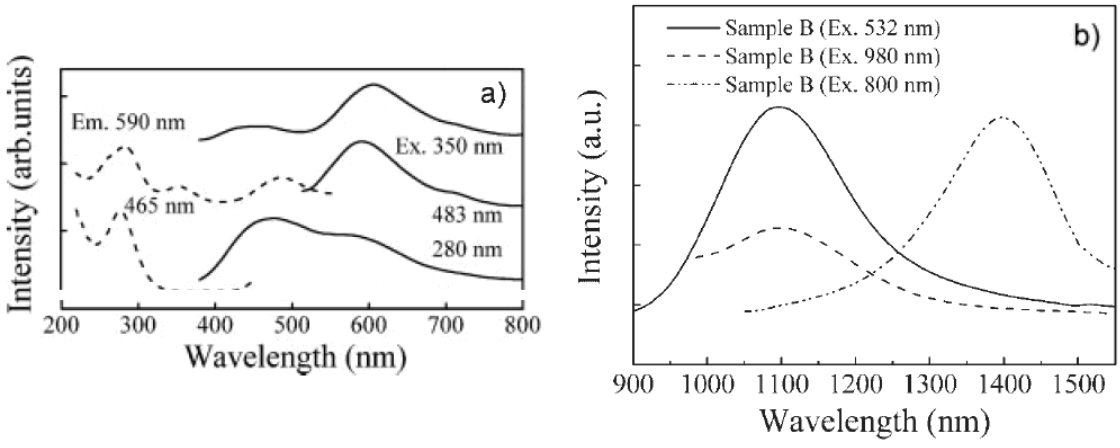

Figure 1.13: (a) PL and PL excitation of Bi doped nanoporous glass in visible region under various excitations. (b) Infrared luminescence from Bi doped nanoporous glass under various excitations [77].

Unfortunately, the origin of Bi-related broadband luminescence is still controversial, because Bi ions may take the form of multiple valence states in different hosts, such as Bi^{5+}, Bi^{3+}, Bi^{2+}, and Bi^{+} [47, 70, 79-81]. Significant differences in absorption, emission, and life time of emission among the Bi^{2+}, Bi^{3+} and Bi NIR active centers indicate that the broadband NIR PL probably does not originate from Bi^{2+} and Bi^{3+} [80,81]. On the other hand, the high temperature annealing may be able to be ruled out the origin from Bi^{5+}, because Bi^{5+} is not stable at high temperature [79]. Sun et al. studied annealing atmosphere and temperature dependence of Bi NIR PL in zeolite, they suggest that Bi^{+} is the most probable origin of the Bi NIR luminescence. Very recently, interstitial negative-charged Bi dimers, Bi^{-}_{2} and Bi^{2-}_{2}, are also suggested as a model of broadband NIR luminescence active centres in Bi doped

glasses [70]. The model (Figure 1.14) was proposed based on quantum-chemical calculations of equilibrium configurations, absorption, luminescence and luminescence excitation spectra of the dimers in an alumosilicate glass network. Above controversial results indicate that further investigation on Bi NIR luminescence for clarifying the origin is necessary.

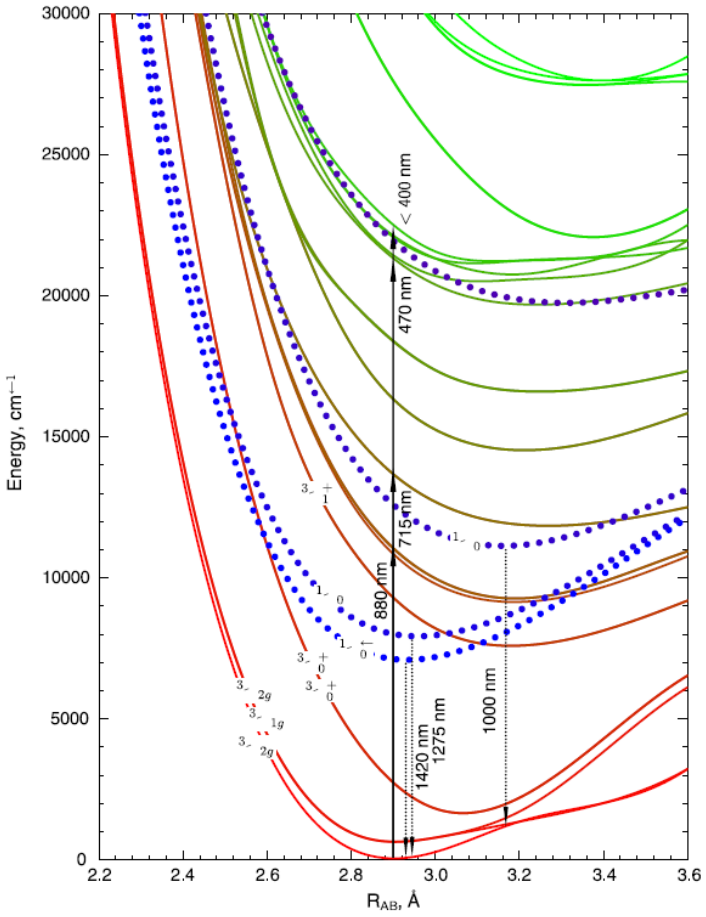

Figure 1.14: Total energy curves for low-lying states of Bi^{2-}_2 dimer [70].

1.2.2 Ag clusters in zeolites

1.2.2.1 Tunable luminescence of Ag species in zeolites

Zeolite is one of the most suitable host materials for the formation of metal clusters. Metal clusters are known to be chemically stable in the nano-sized pores in the cage, and can be formed by a simple ion exchange process followed by a thermal treatment [82-84]. Geoffrey A. Ozin et al. [83] investigated the Ag atoms and small Ag clusters stabilized in zeolite Y by optical spectroscopy measurement. The investigation suggests that under low loading conditions, isolated Ag atoms are located in site I (Figure 1.8 (a)). Higher Ag loading causes the formation of an Ag_2^+ cluster which appears to be best described as a Ag atom in site I

interacting with a Ag ion in site I'. Ag_3^{2+} clusters from the existing Ag_2^{+} cluster by occupying the vacant site I' adjacent to the Ag atom in site I can be formed in completely Ag exchanged zeolite Y annealed in oxygen at high temperature 400-480 ^{o}C. Ag exchanged Na-A zeolite under γ irradiation or H_2 reducing was studied by J. Michalic and L. Kevan [84]. Depending on Ag concentration, Ag_3 and Ag_6 can be formed in the sodalite cage.

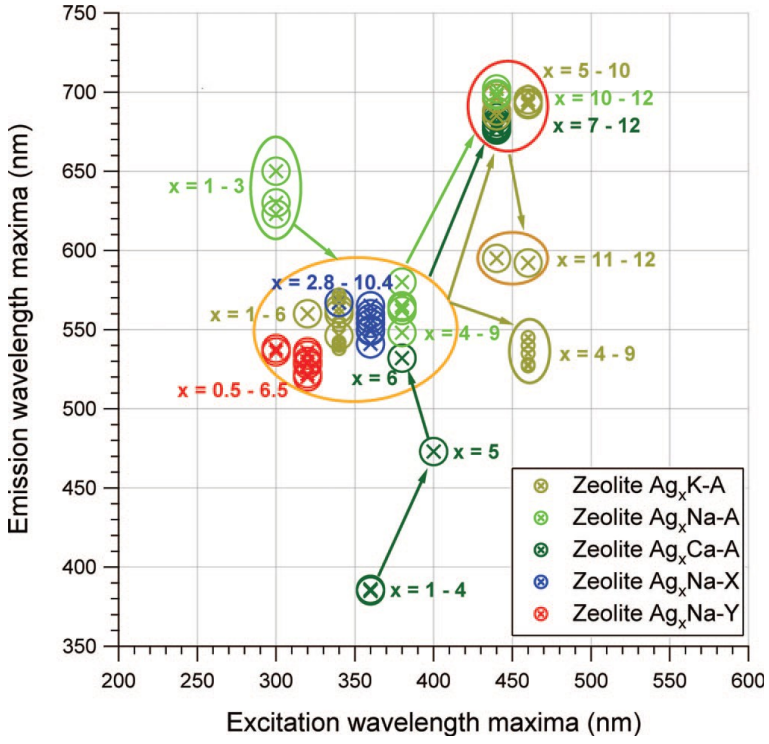

Figure 1.15: Position of the most pronounced luminescence bands of the heattreated silver-exchanged zeolites. For each set of samples, the global trends upon increasing the silver loading are highlighted by the colored arrows. The resolution of the excitation maxima is 20 nm [82].

Very recently, tunable fluorescent of Ag exchanged various zeolites were reported [82]. Depending on the zeolite topology, the presence of specific cation, and the Ag concentration, various emissions shown in Ag doped zeolites annealed in air. In the Ref [82], various concentrations of Ag in different types of zeolites were prepared. Tunable emission-excitation bands were observed, the positions of the most intense luminescence bands for the different samples are summarized in Figure 1.15, where *x* represents the amount of Ag atoms in the unit cell. The emission position strongly depends on Ag concentration and zeolite type. Based on luminescence properties and ESR measurements, the origin of yellow and red emission

was ascribed to Ag_3^+ and Ag_6^+ cluster, respectively. In the further work of this group, they analyzed the appearance of Ag_3 cluster in zeolite A and Y [85]. Triatomic Ag clusters were found to be located inside the sodalite cages for LTA zeolites, while in FAU-type zeolites the Ag_3^{n+} is located at the hexagonal prisms, as indicated in Figure 1.16. Furthermore, the external quantum efficiency (EQE %) of Ag doped zeolites was measured by integrated sphere [86]. In Figure 1.17, EQE dependence of the Ag concentration in zeolites was analyzed. As shown in Figure 1.17, higher EQE was observed in zeolite FAU type zeolites, the EQE of LTA is lower than that in FAU type zeolites.

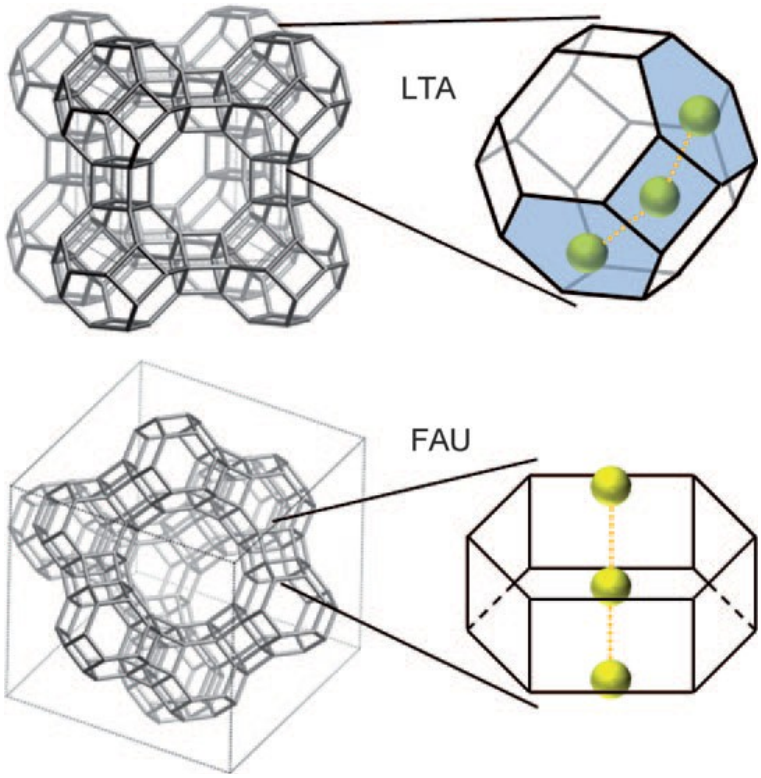

Figure 1.16: Location of triatomic silver clusters in LTA and FAU type zeolites. In LTA zeolites, the bent Ag_3^{n+} cluster is located inside the cuboctaheral sodalite cages, with the outer silver atoms at the hexagonal windows. In FAU type zeolites the Ag_3^{n+} cluster is linear and located at the hexagonal prisms [85].

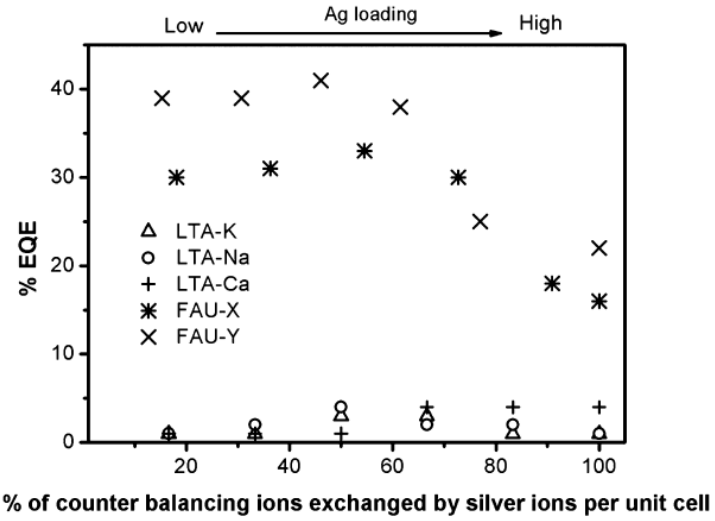

Figure 1.17: EQE of silver-clusters zeolite composites as a function of silver loading [86].

Optical properties of Ag ions in zeolites were also extensively investigated [87-89]. It shows blue emission with a UV excitation [87]. R. Seifert at el. [88] studied the UV-visible absorption spectra of hydrated and vacuum activated Ag^+ of zeolite A from room temperature to 200 ^oC. The concentration dependence of absorption and activation conditions was reported. It was found that the Ag^+ coordinated to 6- and 8-ring oxygens gives rise to electronic transitions in the near-UV region. The electronic transition is denoted as $Ag^+(5s)\rightarrow O(n)$. An absorption in the visible region at 22000 cm^{-1} appeared in the yellow colored vacuum activated sample when increasing Ag concentration. Furthermore, the red colored sample with high concentration of Ag shows absorption band at 19 000 cm^{-1}. The absorptions of Ag ions in dehydrated and hydrated zeolite Y are also shown in the report. A band at about 34000 cm^{-1} appeares in Ag doped zeolite Y upon dehydration and vanishs upon rehydration. The above researches indicate that zeolites are suitable host material for the formation of Ag clusters and stabilization of Ag ions.

1.2.2.2 Ag species act as sensitizer for rare earth ions

LEDs have been developed for application in many fields, such as lighting, displays, and devices indicators, etc [90-92]. Especially, white LEDs lightings have attracted considerable attention and have already partially been put into practical use.

In 1997, the first white LEDs became commercially available [93]. There are three typical ways to obtain white LEDs. The first type is the combination of a blue LED with a yellow powder phosphor, blending the blue light from the LED and yellow light from the phosphor results in white light. This is the most commonly adopted type for industry due to

its low cost and mass production adaptability. The second type is combining blue, green and red LEDs to obtain white emission. The third type is to use ultraviolet (UV) light to excite the red, green and blue phosphors to generate the white emission. Figure 1.18 shows the common emission spectrum of a white LED composed of a blue LED chip and a cerium doped yttrium aluminum garnet [$Y_3Al_5O_{12}:Ce^{3+}$ ($YAG:Ce^{3+}$)] yellow powder phosphor coating with a silicone resin on the blue LED chip surface [94]. However, the device based on $YAG:Ce^{3+}$ phosphor exhibits a poor color rendering index (Ra~ 70-80) and a high correlated color temperature (CCT~ 7750 K) because of lacking a red light contribution [94,95].

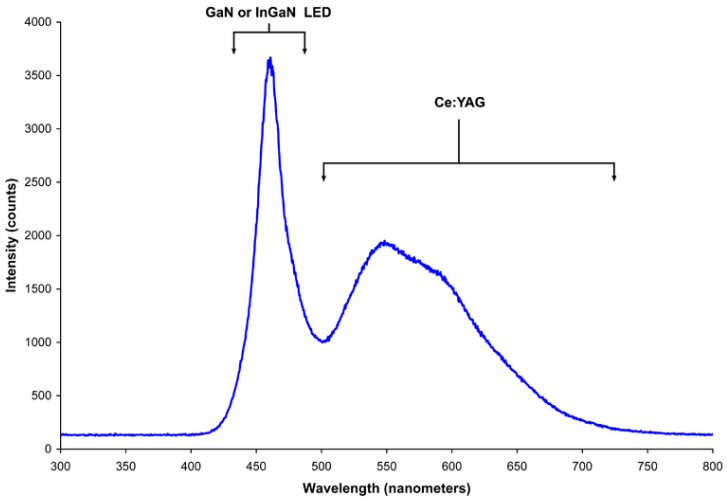

Figure 1.18: White emission spectrum of the w-LED consisting of $YAG:Ce^{3+}$ yellow phosphors and a blue LED chip [94].

Another effective way for obtaining white light is mixing the three monochromatic sources (blue, green, and red) [96]. Very recently, a crystal $BaMg_2Al_6Si_9O_{30}:Eu^{2+}$, Tb^{3+}, Mn^{2+} for white LEDs was reported. White light can be abtained by coupling the blue emission of Eu^{2+}, green emission of Tb^{3+} and red emission of Mn^{2+} (as shown in Figure 1.19). By properly controlling the relative composition of Tb^{3+}/Mn^{2+}, chromaticity coordinates of (0.31, 0.30), high color rendering index (Ra = 90), and correlated color temperature (CCT = 5374 K) can be achieved upon UV excitation. The report indicates that UV white LED can easily be achieved by combining three monochromatic sources.

RE ions activated phosphors have attracted great interest [94, 96]. The Eu^{3+} and Sm^{3+} activated phosphors are good choice for red emitting phosphors in white LEDs [97]. On the other hand, Dy^{3+} is another good activator and a report of Dy^{3+}-activated YPO_4 indicate that it is a potential white phosphor because of the yellow ($^4F_{9/2}$-$^6H_{13/2}$) and blue ($^4F_{9/2}$ -$^6H_{15/2}$)

emissions of Dy^{3+}. By controlling the yellow-to-blue intensity ratio appropriately, it is possible to obtain near-white emission [98]. Recently, RE ions activated zeolites have been studied. It has been shown that they are promising phosphors, lasers and NIR emitters [47, 99-102]. The location dependence of the Eu^{3+} on the heat treatment temperatures from 0 to 200 ^{o}C in zeolite Y was investigated by Berry et al. [99]. It is found that the Eu^{3+} ions are located in the supercage until annealed at 100 ^{o}C. Then they are moved into sodalite cage while annealed up to 200 ^{o}C. S.B. Hong et al. [100] investigated the variation of the cation location and occupancy at different sites in Tb^{3+} doped Na-Y zeolites as a function of treatment temperature. The results demonstrate that most of the Tb^{3+} ions exchanged into the supercages, the Tb^{3+} ions migrate first to sodalite cages at temperatures lower than 473 K and then migrate to hexagonal prisms between 473 and 523 K. Furthermore, S.B. Hong et al.[101] observed that the intra migration of Tb^{3+} ions arising from thermal treatments in FAU-type zeolites is strongly depend on the framework ratio of Si to A1. For a low-silica FAU zeolite (Si/A1 = 1.37), most of the Tb^{3+} ions are exchanged into the supercages. They begin to migrate directly to hexagonal prisms at 423 K without staying at sodalite cages. In contrast, the cations in a high-silica FAU zeolite (Si/A1 = 3.40) move first to sodalite cages at 373 K and then turn to hexagonal prisms at temperatures higher than 373 K. The luminescence properties of hydrated Eu^{3+} exchanged zeolite A at 4.2 K were reported [102]. They suggested that Eu^{3+} ions are located in two sites (supercage and outside of the zeolite) in the zeolite A at low temperature.

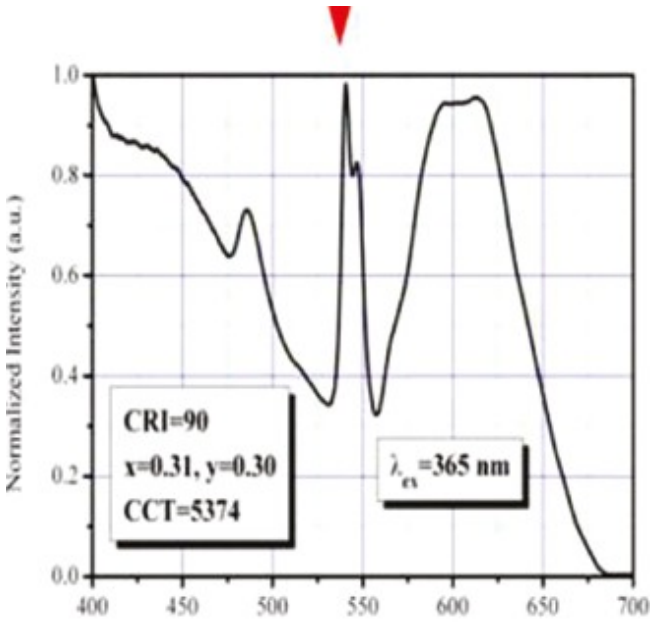

Figure 1.19: The PL spectra of a single composition BMAS: 0.04Eu^{2+}, 0.08Tb^{3+}, 0.16Mn^{2+} phosphor under 365 nm excitation [96].

However, the optical absorption of the RE^{3+} ion is very week due to the forbidden nature of intra-4f transitions. Sensitization by surface Plasmon resonance or energy transfer process is an attractive way to obtain efficient emission from RE ions. Many researches on sensitization of RE ions are reported. S. Yan et al. [103] reported an observation of enhanced red emission at 613 nm originating from $^5D_0$ - $^7F_2$ transition of Eu^{3+} in $CaMoO_4$ by co-doping Bi^{3+}. Strongly enhanced red emission from Eu^{3+} is obtained by adding Bi^{3+} instead of increasing the Eu^{3+} concentration. Lifetime and diffuse reflection spectra measurements indicate that the red emission enhancement is due to the enhanced transition probabilities from the ground state to $^5L_6$ and $^5D_2$ states of Eu^{3+} in the distorted crystal field and an energy transfer from Bi^{3+} to Eu^{3+}. They concluded that the material is a promising red-emitting phosphor for white light diodes with near-UV/blue GaN-based chips. Enhanced PL of Dy^{3+} based phosphor by Li^+ doping was also reported [104]. The incorporation of Li^+ ions into the Ga_2O_3:Dy^{3+} film have enlarged the grain size and enhanced the PL intensities.

One of the most important properties of Ag species is acting as sensitizer for RE ions. During the past years, RE ions sensitized by Ag species are extensively reported. For example, PL of RE ions in silicate glasses can be significantly enhanced by metal clusters (Ag and Au) precipitated by synchrotron X-ray irradiation. The enhancement is found to be caused by energy transfer from metal clusters to RE ions. The excitation and emission bands are located in the UV (325-375 nm) and bluish-green (450-700 nm) regions, respectively [105]. It has been also reported that, in oxyflouride glass, doping of Ag ions (Ag^+) can greatly enhance the PL of RE ions, due to the energy transfer from Ag^+ to RE ions [106]. The significant enhancement was observed under the excitation in the UV region. Furthermore, A. Pillonnet et al. reported that RE ions coupled with Ag nanoparticles (NPs) have been investigated. It is generally accepted that sensitized luminescence occurs due to the local surface plasmon resonance effect of Ag NPs. The resonant wavelength is around 400 nm, depending on the size and the dielectric constant of surrounding materials [107]. RE ions coupled with Ag species such as Ag clusters, Ag ions, and Ag particles are very promising for the realization of UV LED based white light sources which possess a wide range of color temperature tunability. These researches indicate that metal clusters/ions have great potential to enhance the effective excitation cross section of RE ions.

1.3 Chapter Overview and Goal of this thesis

1.3.1 Photoluminescence properties of Bi doped oxidized porous silicon

The goal of the first part of this thesis is to achieve Bi NIR luminescence in porous Si thin films, to clarify the conditions of Bi NIR luminescence in porous Si thin films, and to investigate the mechanism of the NIR luminescence. In chapter 2, Luminescence properties of Bi-doped porous Si thin films are studied for the first time. The samples are prepared by a solution based method, consisting of conventional anodizing etching of Si wafer and dip coating. Two broadband NIR luminescence bands are observed in the Bi doped porous Si by pre-oxidizing porous Si thin film and annealing in N_2 at high temperature. The PL spectra depended on the Bi concentration and oxidation temperature. The oxidation temperature dependence revealed that oxidation of Si into silica is indispensable to activate the Bi NIR active centers in oxidized porous Si. A detailed analysis of the 3D plot of PL intensities versus excitation and emission wavelengths revealed that these luminescence bands arise from at least two different kinds of Bi luminescence centers. The NIR luminescence depended strongly on the annealing atmosphere and temperature. It is found that annealing in N_2 is necessary for activating NIR emission from Bi in pure porous silica thin films. To reveal the origin of the NIR luminescence, comprehensive PL studies including steady state and time-resolved PL measurements at 8–300 K in wide excitation (250–500 nm) and detection (400–1550 nm) wavelength ranges are performed. It is revealed that multiple Bi luminescence centers, such as Bi^{3+}, Bi^{2+}, Bi^{+}, and Bi dimer, are stabilized in porous silica.

1.3.2 Photosensitization of Eu^{3+} by silver clusters in zeolite Y

The goal of second part of this thesis is to obtain photosensitization of RE^{3+} ions by Ag clusters/ions in zeolites. In Chapter 3, the effect of Ag clusters on the PL properties of Eu^{3+} ions in zeolite Y is investigated. Ag cluster can be formed in zeolite Y by ion exchange and thermal treatment procedure. A new absorption band and the enhancement in the PL of Eu^{3+} ions for the sample containing Ag clusters are observed. Dependence of PL intensity on Ag concentration revealed that the enhancement factor of the Eu-PL reaches as high as 27. Excitation wavelength dependence of the PL intensity coincides well with the absorption spectrum of the Ag clusters, indicating that the energy transfer from Ag clusters to Eu^{3+} ions is responsible for the enhancement of the PL of Eu^{3+} ions. The results suggest that zeolite is a promising host material for the sensitization of RE ions by metal clusters.

1.3.3 Enhanced red luminescence of Sm^{3+} in zeolite A by silver ions

The goal of chapter 4 of this thesis is to investigate the sensitization of RE ions (Sm) by Ag ions in zeolite A. In chapter 4, it is shown that the PL of Sm^{3+} is significantly enhanced by the presence of Ag ions in UV excitation wavelength region. The PL results indicate that the enhancement factor of the Sm-PL reaches as high as 30 without further annealing steps. The

excitation wavelength dependence of the PL intensity in co-doped sample coincides well with the absorption spectrum of the Ag ions, indicating that the energy transfer from Ag^{+} ions to Sm^{3+} ions is responsible for the enhancement of the PL of Sm^{3+}. It is expected that the present RE and Ag co-doped zeolites have potential application in white LEDs.

References

[1] Uhlir. Bell Syst. Tech. J. **35**, 333 (1956).

[2] L. T. Chanham, Appl. Phys. Lett. **57**, 1046 (1990).

[3] A. G. Cullis, L. T. Chanham, and P. D. J. Calcott, J. Appl. Phys. **82**, 909 (1997).

[4] U. Gosele, V. Lehmann, Mter. Chem. and Phys. **40**, 253 (1995).

[5] T. Nakamura, T. Ogawa, N. Hosoya, S. Adachi, Journal of luminescence, **130**, 682 (2010).

[6] P. Nebolova , J. Spirkova , V. Perina , I. Jirka , K. Mach ,G. Kuncova, Solid State Ionics. **141**, 609 (2001).

[7] M. Balucani, V. Bondarenko, G. Lamedica, A. Ferrari, L. Dolgyi, N. Vorozov, V. Yakovtseva, S. Volchek, V. Petrovich, N. Kazuchits, Thin Solid Films. **396**, 201 (2001) .

[8] E.J.TEO, A.A.Bettiol, P.Yang, M.B.H.Breese, G.Z.Mashanovich, W.R.Headley, and G.T.Reed, Opt. Lett. **34**, 659 (2006).

[9] Y. Fujimoto, M. Nakatsuka, Appl. Phys. Lett. **82**, 3325 (2003).

[10] M. Peng, J. Qiu, D. Chen, X. Meng, I. Yang, X. Jiang, C. Zhu, Opt. Lett. **29**, 1998 (2004).

[11] V. Sokolov, V. Plotnichenko, E. Dianov, Opt. Lett. **33**, 1488 (2008).

[12] B. Denker, B. Galagan, V. Osiko, S. Sverchkov, E. Dianov, Appl. Phys. B **87**, 135 (2007).

[13] S. Zhou, G. Feng, J. Bao, H. Yang, J. Qiu, J. Mater. Res. **22** (6), 1435 (2007).

[14] M. Peng, D. Chen, J. Qiu, X. Jiang, C. Zhu, Opt. Mater. **29**, 556 (2007).

[15] H. Sun, Y. Sakka, M. Fujii, N. Shirahata, and H. Gao, Opt. Lett. **36**, 100 (2011).

[16] Z. Bai, H. Sun, T. Hasegawa, M. Fujii, F. Shimaoka, Y. Miwa, M. Mizuhata, and S. Hayashi, Opt. Lett. **35**, 1926 (2010).

[17] R. L. Smith, and S. D. Collins, J. Appl. Phys. **71**, R1 (1992).

[18] V. Lehmann, and U. Gösele, Appl. Phys. Lett. **58**, 856 (1991).

[19] R. Herino, G. Bomchil, K. Barla, and C. Bertrand, J. Electrochem. Soc. **134**, 1994 (1987).

[20] M. J. J. Theunissen, J. Electrochem. Soc. **119**, 351 (1972).

[21] H. Foll, M. Christophersen, J. Carstensen, and G. Hasse, Mater. Sci. and Engin. R **39**, 93 (2002).

[22] J. Kanungo, S. Maji, A. K. Mandal, S. Sen, E. Bontempi, A. K. Balamurugan, A. K. Tyagi, K. Uvdal, S. Saha, and S. Basu, J. Appl. Surf. Sci. **256**, 4231 (2010).

[23] B. Hamiton, Semicond. Sci. Technol. **10**, 1187 (1995).

[24] I. Berbezier, and A. halimaoui, J. Appl. Phys. **74**, 5421 (1993).

[25] J. Dian, A. Macek, D. Niznansky, I. nemec, V. Vrkoslav, T. Chvojka, I. Jelinek, Appl. Surf. Sci. **238**, 169 (2004).

[26] S. Shichi, M. Fujii, and S. Hayashi, Opt. Lett. **36**, 1 (2011).
[27] L. T. Chanham, Appl. Phys. Lett. **57**, 1046 (1990)
[28] A. G. Cullis, L. T. Chanham, and P. D. J. Calcott, J. Appl. Phys. **82**, 909 (1997).
[29] P.Y.Y. Kan, T.G. Finsttad, Mater. Sci. and Engineering, B**115**, 289 (2005).
[30] A. Bsiesy, J.C.Vial, F. Gaspard, R. Herino, M. Ligeon, F. Muller, R.Romestain, A. Wasiela, Surf. Sic., **254**, 195 (1991).
[31] G. Bomchil, A. Halimaui, Microelectronic Engineering, **8**, 293 (1988).
[32] G. Bomchil, A. Halimaui, Appl. Surf. Sci. **41-42**, 604 (1989).
[33] S. Konaka, M. Tabe, T. Sakai, Appl. Phys. Lett. **41**, 86 (1982).
[34] N. J. Thomas, J. R. Davis, J. M. Keen, J. G. Castledine, D. Brumhead, M. Goulding, J. Alderman, J. P. G. Farr, L. G. Earwaker, J. L. Ecuyer, I. M. Stirland and J. M. Cole, IEEE Electron device letters, **10**, 129 (1989).
[35] R. T. Collins, P. M. Fauchet and M. A. Tischler, Physics Today, **50**, 24 (1997).
[36] L. Pavesi, R. Guardini and C. Mazzoleni, Solid State Communications, **97**, 1051 (1996).
[37] N. Lalic, J. Linnros, Thin Solid Films, **276**, 155 (1996).
[38] Y. Kanemitsu, Physics Reports, **263**, 1 (1995).
[39] V.P.Bondarenko, A.M.Dorofeev, and N.M.Kazuchits, Microelectronic Engineering, **28**, 447 (1995).
[40] A. Najar, J. Charrier, H. Ajlani, N. Lorrain, S. Haesaert, M. Oueslati, L. Haji, Materials Science and Engineering, B **146**, 260 (2008).
[41] A. Najar, J. Charrier, N. Lorrain, L. Haji, M. Oueslati, Appl. Phys. Lett. **91**, 121120 (2007).
[42] A.M. Dorofeev, N.V. Gaponenko, V.P. Bondarenko, J. App. Phys. **77**, 2679 (1995).
[43] M. Balucani, V. Bondarenko, G. Lamedica, A. Ferrari, L. Dolgyi, N. Vorozov, V. Yakovtseva, S. Volchek, V. Petrovich, N. Kazuchits, Thin Solid Films,**396**, 201 (2001).
[44] D. Navarro-Urrios, M. Melchiorri, N. Daldosso, L. Pavesi, C. Garcıa, P. Pellegrino, B. Garrido, G. Pucker, F. Gourbilleau, R. Rizk, J. Lumin. **121**, 249 (2006).
[45] K. Binnemans, Chem. Rev. **109**, 4283 (2009).
[46] U. Kynast, V. Weiler, Adv. Mater. **6**, 937 (1994).
[47] H. Sun, A. Hosokawa, Y. Miwa, F. Shimaoka, M. Fujii, M. Mizuhata, S. Hayashi, S.Deki, Adv. Mater. **21**, 3694 (2009).
[48] D. Sendor, U. Kynast, Adv. Mater. **14**, 1570 (2002).
[49] Z. Bai, M. Fujii, Y. Mori, Y. Miwa, M. Mizuhata, H. Sun, and S. Hayashi, Opt. Lett. **6**, 36 (2011).

[50] R. M. Barrer, Zeolites and Clays as Sorbents and Molecular Sieves; Academic Press: London, (1978).
[51] P. K. Dutta, D. C. Shieh, J. Phys. Chem. **90**, 2331 (1986).
[52] P. K. Dutta, D. C. Shieh, M. Puri, J. Phys. Chem. **91**, 2332 (1987).
[53] M. E. Davis, Ind. Eng. Chem. Res. **30**, 1675 (1991).
[54] T. Sun, and k. Seff, Chem. Rev. **94**, 857 (1994).
[55] McBain, J. W., *The Sorption of Gases and Vapors by Solids* (Routledge, London) (1932).
[56] P. Enzel, T. Bein, J. Phys. Chem. **93**, 6270 (1989).
[57] M. E. Davis, P. F. Lobo, Chem. Mater. **4**, 756 (1992).
[58] F. Namovar, F. Lu, C.H. Perry, A. Cremins, N.M. Kalhorau, J.T. Daly, R.A. Soref, Mater. Res. Soc. Symp. Proc. **358**, 375 (1995).
[59] M. Balucani, V. Bodarenko, G. Lamedica, A. Ferrari, L. Dolgyi, N. Vorozov, V. Yakovtseva, S. Volcheck, V. Petrovich, N. Kazuchits, Thin Solid Films, **396**, 201 (1996).
[60] A. Moadhen, H. Elhouichet, M. Oueslati, M. Fe´rid, J. Lumin. **99**, 13 (2002).
[61] T. Kumura, A. Yokoi, H. Horigrechi, R. Saito, T. Ikoma, A. Sato, Appl. Phys. Lett. **65**, 983 (1994).
[62] T. J. Whitley, J. Ligthwave Technol. **13**, 744 (1995).
[63] W. Miniscalco, J. Ligthwave Technol. **9**, 234 (1991).
[64] H. Kidorf, K. Rottwitt, M. Nissov, M. Ma, E. Rabarijaona, Photonics Technology Letters. **11**, 530 (1999).
[65] C. R. S. Fludger, V. Handerek, R. J. Mears, Journal of Lightwave Technology. **19**, 1140 (2001).
[66] Y. Fujimoto, M. Nakatsuka, Appl. Phys. Lett. **82**, 3325 (2003).
[67] J. Ren, J. Qiu, D. Chen, X. Hu, X. Jiang, and C. Zhu, Journal of Alloy and Compound, **463**, L5 (2008).
[68] X. Meng, J. Qiu, M. Peng, D. Chen, Q. Zhao, X. Jiang, C. Zhu, Opt. Express **13**,1635 (2005).
[69] M. Peng, D. Chen, J. Qiu, X. Jiang, C. Zhu, Opt. Mater. **29**, 556 (2007).
[70] V. O. Sokolov, V. G. Plotnichenko, V. V. Koltashev and E. M. Dianov, J. Phys. D: Appl. Phys. **42**, 095410 (2009).
[71] H. Sun, Y. Miwa, F. Shimaoka, M. Fujii, A. Hosokawa, M. Mizuhata, S. Hayashi, S. Deki, Opt. Lett. **34**, 1219 (2009).
[72] H. Sun, Y. Sakka, Y. Miwa, N. Shirahata, M. Fujii, H. Gao, Appl. Phys. Lett. **97**,131908 (2010).

[73] H. Sun, M. Fujii, Y. Sakka, Z. Bai, N. Shirahata, L. Zhang, Y. Miwa, H. Gao, Opt.Lett. **35**, 1743 (2010).

[74] H. Sun, T. Hasegawa, M. Fujii, F. Shimaoka, Z. Bai, M. Mizuhata, S. Hayashi, S.Deki, Opt. Express. **17**, 6239 (2009).

[75] Z. Bai, M. Fujii, T. Hasegawa, K. Imakita, Y. Miwa, M. Mizuhata, S. Hayashi, Microporous and Mesoporous Materials, **145**, 21 (2011).

[76] S. Zhou, N. Jiang, B. Zhu, H. Yang, S. Ye, G. Lakshminarayana, J. Hao, and J. Qiu, Adv. Funct. Mater **18**, 1407 (2008).

[77] I. Razdobreev, H. El Hamzaoui, V. Ivanov, E. Kustov, B. Capoen, and M. Bouazaoui1, Opt. Express. **35**, 1341 (2010).

[78] L. I. Bulatov, V. V. Dvoyrin, V. M. Mashinsky, E. M. Dianov, A. P. Suhorukov, A. A. Umnikov, and A. N. Guryanov, Bulletin of the Russian Academy of Sciences: Physics, **72**, 98 (2008).

[79] Y. Fujimoto, M. Nakatsuka, Jpn. J. Appl. Phys. **40**, L279 (2001).

[80] G. Boulon, B. Moine, and J. Bourcet, Phys. Rev. B. **22**, 1163 (1980).

[81] G. Blasse, A. Meuerink, M. Nommes, and J. Zuidema, J. Phys. Chem. Solids. **22**,171 (1994).

[82] G.D. Gremer, E. Coutino-Gonzalez, M. B. J. Roeffaers, B. Moens, J. Ollevier, M. V. Auwerear, R. Scoonheydt, P. A. Jacobs, F. C. D. Schryver, J. Hofkens, D. E. D. Vos, B. F. Sels, T. Vosch, J. Am. Chem. Soc. **131**, 3049 (2009).

[83] G. A. Ozln, and F. Hugues, J. Phys. Chem. **87**, 94 (1983).

[84] J. Michalic and L. Kevan, J. Am. Chem. Soc. **108**, 4247 (1986).

[85] G.D. Gremer, E. Coutino-Gonzalez, M. B. J. Roeffaers, D. E. D. Vos, J. Hofkens, T. Vosch, and B. F. Sels, Chem. Phys. Chem. **11**, 1627 (2010).

[86] E. Coutino-Gonzalez, M. B. J. Roeffaers, B. Dieu, G.D. Gremer, S. Leyre, P. Hanselaer, W. Fyen, B. Sels, and J. Hofkens, J. Phys. Chem. C **117**, 6998 (2013).

[87] J. Texter, Phys. Reav. B **23**, 4407 (1981).

[88] R. Seifert, R. Rytz, and G. Calzaferri: J. Phys. Chem. A **104**, 7473(2000).

[89] G. Calzaferri, C. Leiggener, S. Glaus, D. Schurch, and K. Kuge: Chem. Soc. Rev. **32,** 29 (2003).

[90] P. Pimputkar, J. S. Speak, S.P. DenBaars, S. Nakamura, Nature Photonics **3**, 180 (2009).

[91] J. Kido, H. Shionoya, K. Nagai, Appl. Phys. Lett. **67**, 2281 (1995).

[92] P. Waltereit, O. Brandt, A. Trampert, H.T. Grahn, J. Menniger, M. Ramsteiner, M. Reiche, K.H. Ploog, Nature **406**, 865 (2000).

[93] S. Nakamura, G. Fasol, The Blue Laser Diode: GaN Based Light Emitters and Lasers, Springer, Berlin, (1997).

[94] A. A.Setlur,W. J.Heward, Y.Gao, A. M.Srivastava, R. G.Chandran, M. V .Shankar, Chem. Mater. **18,** 3314 (2006).

[95] H. S. Jang, Y. H.Won, D. Y.Jeon, Appl. Phys. B: Lasers Opt. **95**, 715 (2009).

[96] W. Lu, Z. Hao, X. Zhang, Y. Luo, X. Wang, and J. Zhang, Inorg. Chem. **50**, 7846 (2011).

[97] S. Neeraj, N. Kijima, A.K. Cheetham, Solid State Communications **131**, 65 (2004).

[98] R. Wang, W. Pan, J. Chen, M. Fang, Z. Cao, Y. Luo, Mater.Chem. Phys. **79**, 30 (2003).

[99] F. J. Berry, M. Carbucicchio, A. Chiari, C. Johnson, E. A. Moore, M. Mortimer, F. F. F. J. Vetel, J. Mater. Chem. **10**, 2131 (2000).

[100] S. B. Hong, J. S. Seo, C. H. Pyun, C. H. Kim, and Y. S. Uh , Catalysis Letters **30**, 87 (1997).

[101] S. B. Hong, E. W. Shin, S. H. Moon, C. H. Pyun, C. H. Kim, Y. S. Uh, J. Phys. Chem. **99**, 12274 (1995).

[102] M. F. Hazenkamp, A. M. H. van der Veen, N. Feiken and G. Blasse, J. Chem. Soc. Faraday Trans., **88**, 141 (1992).

[103] S. Yan, J. Zhang, X. Zhang, S. Lu, X. Ren, Z. Nie, and X. Wang, J. Phys. Chem. C **111**, 13256 (2007).

[104] M. L. Pang, W. Y. Shen, and J. Lin, J. Appl. Phys. **97**, 033511 (2005).

[105] M. Eichelbaum, and K. Bademann: Adv. Funct. Mater. **19**, 1 (2009).

[106] S. Paje, M. García, J. Llopis, and M. Villegas: J. Non-Cryst. Solids **318**, 239 (2003).

[107] A. Pillonnet, A. Berthelot, A. Pereira, O. Benamara, S. Derom, G. Colas des Francs, and A. M. Jurdyc: Appl. Phys. Lett. **100**, 153115 (2012).

Part Ⅰ Near infrared luminescence of Bi doped oxidized porous silicon thin films

Chapter 2

Luminescence properties of Bi-doped oxidized porous silicon thin films

In this chapter, luminescence properties of Bismuth (Bi) doped oxidized porous silicon (Si) thin films are studied. It is found that this material shows two broad luminescence bands centered at 845 nm with the FWHM of 120 nm and at 1410 nm with that of 220 nm under 488 nm excitation. The Photoluminescence (PL) spectra depend on the Bi concentration and oxidation temperature. The oxidation temperature dependence reveal that oxidation of silicon into silica is indispensable to activate the Bi NIR active centers in oxidized porous Si. On the other hands, PL properties of Bi doped porous silica thin films annealed at various temperatures and in different atmospheres are studied. The near infrared (NIR) luminescence depends strongly on the annealing atmosphere and temperature. To reveal the origin of the NIR luminescence, comprehensive PL studies including steady state and time-resolved PL measurements at 8-300 K in wide excitation (250-500 nm) and detection (400-1550 nm) wavelength ranges are performed. It is revealed that multiple Bi luminescence centers, such as Bi^{3+}, Bi^{2+}, Bi^{+}, and Bi dimer, are stabilized in porous silica.

2.1 Introductions

With the rapid development of the optical fiber communication networks in recent years, the wavelength division multiplexing system demands fiber amplifiers with broader gain bandwidth in the telecommunication window. Great efforts have been devoted to explore and synthesize new gain media which possess much broader luminescence bands than conventional rare earth ions doped gain media [1-4]. One successful example is Bi doped

silica-based glasses. Fujimoto and Nakatsuka [5, 6] reported a novel infrared luminescence from Bi doped silica-based glasses and realized the optical amplification in the 1.0 μm to 1.6 μm region. Since this broadband gain has a potential to improve transmission capacity and transportation speed of optical fiber communication, Bi doped silica-based glasses have attracted great attention today [7-10].

On the other hand, thin film integrated optics are becoming more and more important in optical communication technology. The technology for the fabrication of passive devices such as planar optical waveguides is well developed now [11]. One next step is the development of waveguide optical amplifiers that can be integrated in passive devices. Recently, oxidized porous Si has attracted great interest as a candidate material for a waveguide optical amplifier [12, 13]. This material can be integrated with other optical devices by conventional microelectronic technology. Furthermore, due to the high open porosity, luminescent materials such as erbium ions can be easily incorporated into the oxidized porous Si thin films. Therefore, oxidized porous Si provides the possibility of fabricating a small size optical amplifier which can be integrated in thin film optical devices [14, 15].

For many years, it is believed that addition of extra elements such as Al is indispensable to obtain NIR emission from Bi-doped bulk glasses [6,16,17]. However, Razdobreev et al. recently demonstrated that Bi doped pure silica glass can exhibit NIR luminescence when the silica glass is porous [18]. Furthermore, we have also found that Bi doped oxidized porous Si shows NIR luminescence without additional elements [19]. Oxidized porous Si is a promising material as a host for different kinds of optical centers. Especially, during the past years, Er-doped oxidized porous Si waveguide type amplifiers have been studied and they are considered to be promising for integrated optical filters, amplifiers/modulators, light-emitting diodes and other optoelectronic devices [12,13,20]. The broadband NIR luminescence from Bi-doped oxidized porous silica may pave the way for the development of broadband waveguide type optical amplifiers operating in the NIR range. However, the research on Bi-doped oxidized porous silica is still limited and the relation between preparation parameters and PL properties is not fully clarified. Furthermore, the origin of the NIR PL is not fully elucidated.

In this chapter, optical properties of Bi-doped oxidized porous Si thin films are studied for the first time. The samples are prepared by a solution-based simple method, consisting of conventional anodizing etching of Si wafer and dip coating. The obtained thin films show broad near infrared (NIR) luminescence which covers the whole telecommunication window, and the electronic configuration of the luminescence centers are discussed. Furthermore, comprehensive PL studies of Bi-doped oxidized porous silica thin films annealed in different atmospheres at different temperatures in wide excitation (250-500 nm) and detection

(400-1550 nm) wavelength ranges are performed. The temperature dependence of the NIR PL spectra and the lifetime for the NIR PL bands are also studied. Based on these results, it is shown that the temperature quenching of the NIR PL is very small, and two different kinds of Bi NIR active centers (Bi^+ and Bi dimer) co-exist in the Bi-doped porous silica. The ultra-broadband of the NIR luminescence with the lifetime of few hundreds microseconds suggests that the porous Si thin film is a promising material for a Si based waveguide type optical amplifier at optical telecommunication wavelengths.

2.2 Experiment details

(100) oriented P-type Si wafers with the resistivity of 20 mΩ·cm are used as initial substrates for the preparation of porous Si. 100 μm thick free standing porous Si monolayers are prepared by electrochemical anodization in the mixture of hydrofluoric (HF) (46 wt. % in water) and ethanol (HF: ethanol = 1: 1) with the anodic current density of 70 mA/cm^2. At the end of the etching process, a high current pulse (300 mA/cm^2, 1.6 s) is applied to detach the porous Si layer from the substrate. Figure 2.1 shows the plain view transmission electron microscope (TEM) image of the as-prepared free standing porous Si. The dark regions correspond to porous Si skeletons, while the bright regions to pores. The pore size is several tens of nanometers. The porosity of the porous Si estimated from the effective refractive index is about 58 % [21, 22].

The obtained porous Si film is oxidized at 850 – 1100 ^oC in air for 1 h. The oxidized thin films are soaked in the doping solutions of $Bi(NO_3)_3{\cdot}5H_2O$ for 48 h at ambient condition. The PH value of the doping solution is controlled to be 3.0 by adding HNO_3 to increase the solubility of $Bi(NO_3)_3{\cdot}5H_2O$. The concentration of $Bi(NO_3)_3{\cdot}5H_2O$ in doping solution is changed from 0 to 3.0 mol/L. For the activation of Bi, the samples are annealed in air or N_2 gas at the temperatures ranging from 1000 to 1300 ^oC. The compositions of the samples are determined by energy-dispersive x-ray spectroscopy (EDS). However, Bi concentration is below the detection limit (~0.1 at. %) for all the samples. PL spectra are measured by using a single grating monochromator equipped with a liquid-nitrogen-cooled InGaAs diode array. Excitation source is a 488 nm line of an argon ion laser. Time-resolved PL measurements are performed by detecting the modulated luminescence signal with a photomultiplier tube (Hamamatsu, R5509-72), and then analyzing the signal with a photon-counting multichannel scaler. The excitation source for the lifetime measurements is the 488 nm light from an optical parametric oscillator pumped by the third harmonic of a Nd:YAG laser. The measurements of NIR PL and decay time are performed in the temperature range of 8-300 K. PLE spectra are measured by the spectrofluorometer equipped with an InGaAs diode array as a detector and xenon lamp (450 mW) as an excitation source at wavelength between 200 nm and 800 nm.

All the measurements are carried out at room temperature. For all the PL spectra, the spectral response of the detection system is corrected by the reference spectrum of a standard tungsten lamp.

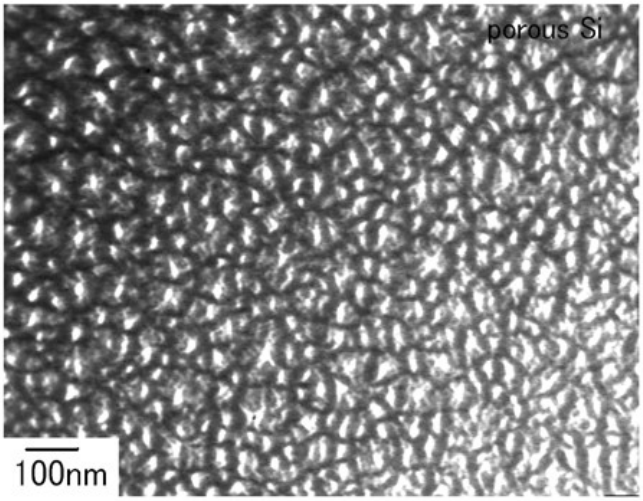

Figure 2.1: TEM image of as-prepared porous Si.

2.3 Results and discussion

First of the study, the PL spectra of host material oxidized porous Si are measured. In the Figure 2.2 (a), the PL spectra of porous Si oxidized from 800-1100 ^{o}C under the excitation of 488 nm are shown. The broad NIR PL observed in the oxidized porous Si, the peak position is in the range from 790 to 900 nm. The PL intensity and the peak position strongly depend on the annealing temperature because it arises from the defect of porous Si [23]. From the normalized PL spectra (Figure 2.2 (b)) we can see that the PL peak first blue shift from 850 ^{o}C drastically, and then red shift gradually.

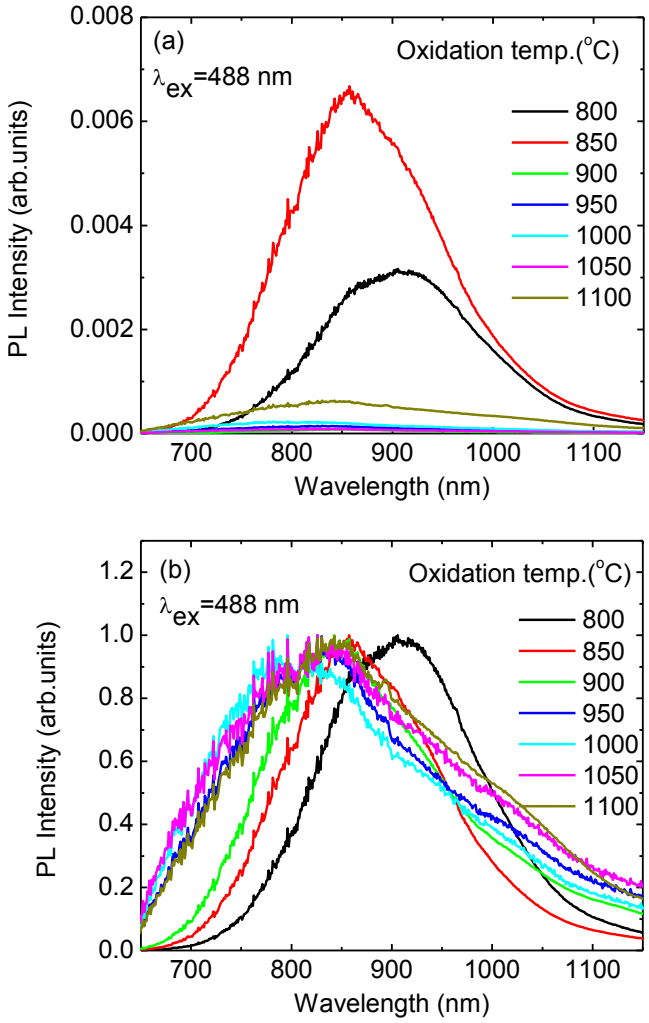

Figure 2.2: (a) PL spectra of the pure oxidized porous Si *at various oxidation temperatures from 800-1100 °C. The excitation wavelength is 488 nm. (b) Normalized PL of the samples.*

2.3.1 Bi concentration dependence of the NIR PL

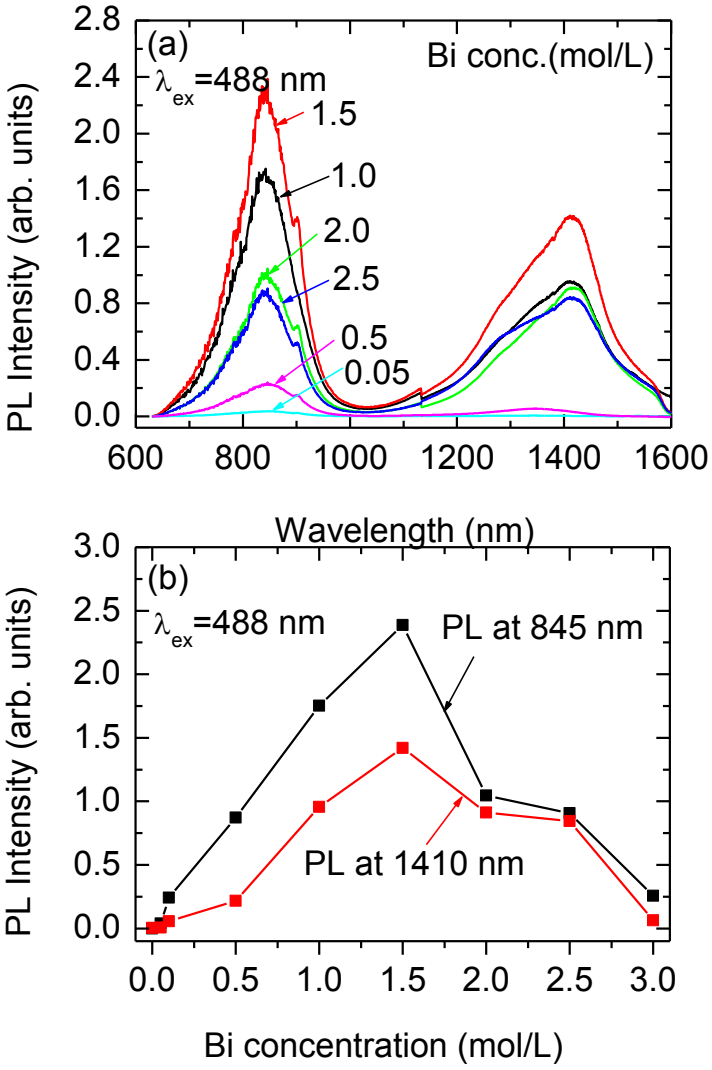

Figure 2.3: (a) Bi concentration dependence of PL spectra of Bi-doped oxidized porous Si *thin films; Bi concentration in doping solution is changed from 0.05 mol/L to 2.5 mol/L. (b) Bi concentration dependence of integrated intensities of the PL bands.*

Figure 2.3(a) shows NIR PL spectra of Bi-doped oxidized porous Si films oxidized at 950 ^{o}C. Bi concentration in doping solution is changed from 0.05 mol/L to 2.5 mol/L. We can see two broad PL bands, one at 1410 nm with the full width at half maximum (FWHM) of 220 nm and the other at 845 nm with the FWHM of 120 nm. Figure 2.3(b) shows the integrated PL intensities of the PL bands as a function of Bi concentration in doping solution. These PL bands are not observed for the samples without Bi doping, thus the PL bands can be ascribed to Bi ions. Since the detailed origin of the NIR PL of Bi ions is still not clarified, hereafter we call them Bi NIR active centers. In Figure 2.3(b), it can be seen that the intensities of the two different bands exhibit similar Bi concentration dependence; with

increasing Bi concentration, the intensities first increase and then decrease. At present, the mechanism of the decrease in intensities at high Bi concentration range is not clear. Considering the very low Bi concentration in the present samples (less than 0.1 at. %), it is not due to concentration quenching. In fact, in Bi doped B_2O_3-Al_2O_3-BaO glasses, the concentration quenching occurs above the Bi concentration of 2.0 mol% [17]. Although the reason is not clear, the quenching is probably due to the decrease of the number of Bi NIR active centers at high Bi concentration range.

It is interesting to note that the PL spectra in longer wavelength side (in Figure 2.3(a)) are much different from those of Bi doped silica-based bulk glasses (such as SiO_2-Al_2O_3 glasses, SiO_2-P_2O_5 glasses, and SiO_2-BaO glasses) [5, 8, 9]. When exited at 488 nm, they show PL with the maximum around 1100 – 1200 nm, while the present samples have the maximum around 1410 nm. The PL spectra observed in our samples are similar to those in a silica glass prepared from a nano porous xerogel [10].

2.3.2 Oxidation temperature dependence of the NIR PL

In order to clarify the condition for the activation of Bi ions in oxidized porous Si thin films, we study the oxidation temperature dependence of the PL spectra. Figure 2.4(a) presents PL spectra of the samples oxidized at 850 – 1100 ^oC. Below 800 ^oC, the samples show no Bi-related NIR luminescence (data was not shown here). In these samples, the Bi concentration in the doping solution is 1.5 mol/L. The PL intensity depends on the oxidation temperature despite the same doping procedure. Figure 2.4(b) plots the integrated PL intensities as a function of the oxidation temperature. With increasing the oxidation temperature, the intensities increase, until the oxidation temperature reaches 1000 ^oC, and then decrease. Note that the samples are oxidized before Bi-doping. When the oxidation temperature is below 800 ^oC, porous Si films are not fully oxidized and brownish, transmittance spectra of oxidized porous Si films are shown in our previous work [19]. The result that the samples oxidized below 800 ^oC show no Bi-related NIR luminescence suggests that high temperature oxidation of Si into silica is necessary to activate Bi NIR active centers. The increase in the PL intensity in the lower oxidation temperature range (<1000 ^oC) is probably due to the higher degree of oxidation of oxidized porous Si films [19, 20]. On the other hand, the decrease in the PL intensity in higher oxidation temperature range is considered to be due to the decrease of porosity of oxidized porous Si thin films. The decrease of the size and number of pores in oxidized porous Si might make Bi doping inefficient, resulting in the decrease of the PL intensities. The decrease of the porosity of oxidized porous Si films by high temperature oxidation is shown by TEM observation [24].

It should be noted that pure oxidized porous Si also exhibit a PL band around 845 nm with the full width with half maximum of about 150 nm (Figure 2.2) [23,25-26]. This is very similar to that observed in Bi doped oxidized porous Si. However, the PL properties of pure oxidized porous Si are much different from those of Bi-doped oxidized porous Si. The Figure 2.2 revealed that the PL intensity of pure porous silica is more than 300 times weaker than that of Bi doped porous silica [19]. In addition, the shape and peak position of the PL from the Bi active center is very insensitive to oxidization conditions of porous Si (Figure 2.3). This is in a sharp contrast with that the peak position of PL from porous silica strongly depends on the oxidation condition [23,25-26]. Thus the origin of the PL at 845 nm can be ascribed to Bi NIR active center.

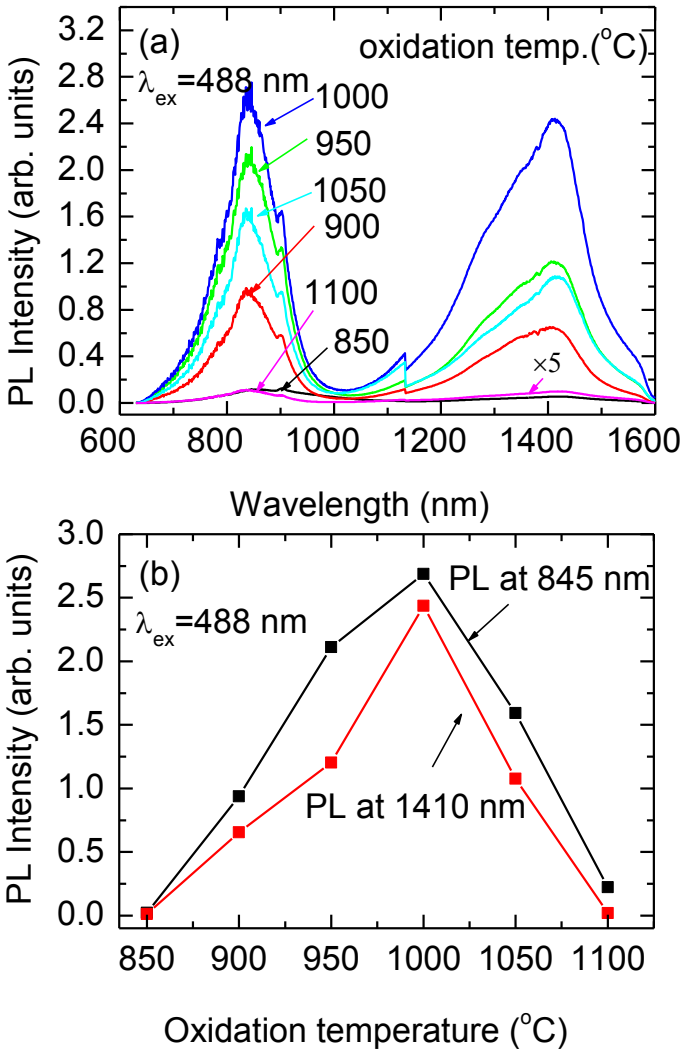

Figure 2.4: (a) PL spectra of Bi-doped oxidized porous Si *thin films as a function of oxidation temperature. (b) The integrated intensities of the PL bands as a function of oxidation temperature.*

2.3.3 Excitation wavelength dependence of the NIR PL

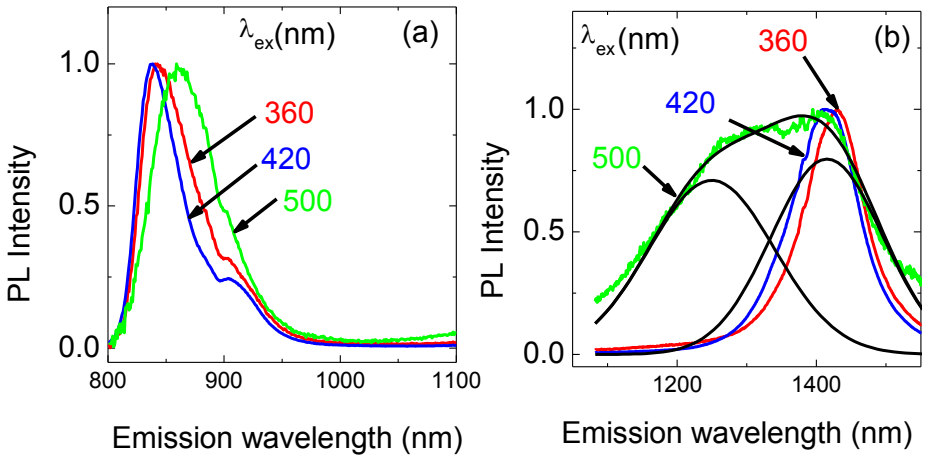

Figure 2.5: (a) (b) Normalized NIR PL bands of Bi doped oxidized porous Si at excitation wavelengths 360, 420, and 500 nm.

Figures 2.5(a) and 5(b) show the normalized PL spectra of Bi-doped oxidized porous Si thin films oxidized at 950 ^{o}C measured with various excitation wavelengths. The both PL strongly depend on the excitation wavelengths. In Figure 2.5(a), the PL at about 840 nm excited by the 360 and 420 nm are almost identical, while that excited at the 500 nm is significantly different. Similar phenomenon is observed in the PL at about 1400 nm (Figure 2.5(b)). As shown in Figure 2.5(b), PL spectrum excited by the 500 nm is much broader than those excited at the 360 or 420 nm. The PL band excited at 500 nm can be decomposed into two Gaussian bands (black lines) with the maximum at 1250 nm and 1400 nm. The PL band at 1400 nm is almost identical to those observed under the 360 and 420 nm excitations, while the PL band at 1250 nm is observed only under the 500 nm. This excitation wavelength dependence of NIR PL suggests that there are at least two different kinds of Bi NIR active centers in our samples. This is consistent with the previous report [10].

2.3.4 Annealing conditions dependence of PL

2.3.4.1 Annealing atmosphere dependence of PL

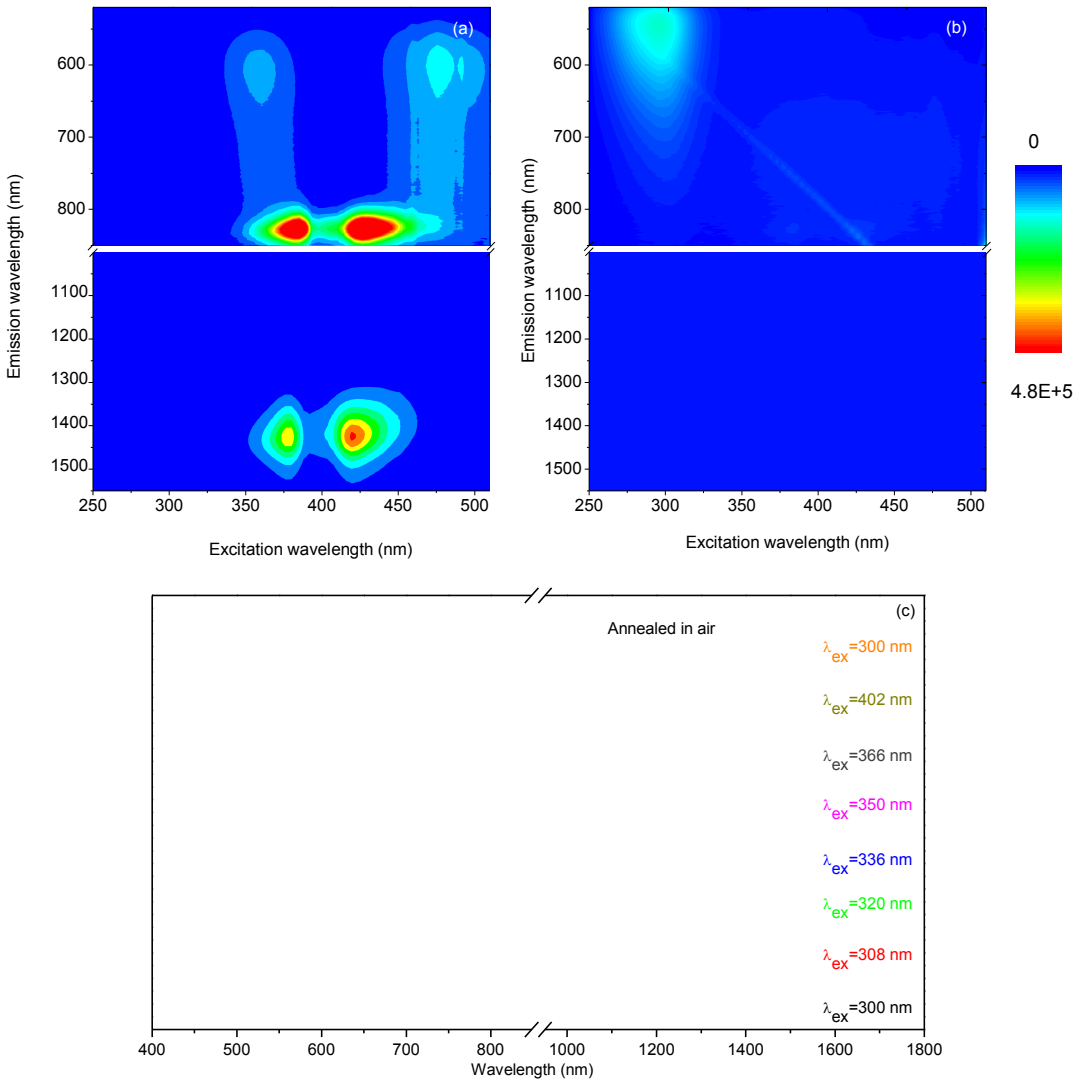

Figure 2.6: (a) and (b) are the 3D plots of the PL intensity versus excitation and emission wavelengths of Bi doped porous silica annealed in N_2 and air. (c) Normalized visible to NIR PL spectra of Bi doped porous silica under the various excitation wavelengths.

Figure 2.6 (a) shows a 3D mapping of the visible to NIR PL intensity of the sample annealed at 1300°C in N_2 gas. The oxidation temperature of the porous Si is 1000 °C. The oxidized porous Si can be called to be porous silica, since the porous Si is fully oxidized while the temperature is above 1000 °C. The ordinate is the excitation wavelength and the abscissa is the emission wavelength. Three PL emission bands, one in the visible range and two in the NIR range, can be seen. For the PL emission band around 606 nm, the PL excitation bands appear around 352 and 475 nm. For the NIR PL emission band around 845 and 1410 nm, two PL excitation bands are seen around 374 and 420 nm. The PL emission

bands around 845 and 1410 nm are similar to those observed for Bi doped pure silica glass fiber perform [3,10].

In contrast to the sample annealed in N_2 gas, the sample annealed in air at 1300 ^oC did not show NIR PL (Figure 2.6(b)). It exhibits a PL emission band around 530 nm with a PL excitation band around 290 nm. Bi-related luminescence is known to be very sensitive to the annealing atmosphere. Recently, Bi doped alkali borosilicate porous silica glass annealed in various atmosphere including oxygen, argon, and hydrogen gases has been reported [9]. It revealed that only the glass annealed in oxygen did not exhibit NIR luminescence. The present results are thus consistent with those in the previous reports [7,27,28].

For more detailed analysis, normalized PL spectra of the sample annealed in N_2 excited at various wavelengths are shown in Figure 2.6(c). For comparison, PL spectrum of the sample annealed in air (orange) is also shown. When excitation wavelengths are shorter than 300 nm, both samples show broad PL around 530 nm. The PL and the PLE features shown in Figure 2.6(b) are very similar to those of Bi doped germinate glass and it is in general assigned to Bi^{3+} [29]. When the excitation wavelength is 320 nm, a PL peak appears around 606 nm for the sample annealed in N_2 gas. In figure 2.6(a), we can see the PL excitation bands around 352 and 475 nm for the PL emission band at 606 nm. This orange emission has been reported for various materials, e.g., SrB_4O_7, and is usually assigned to Bi^{2+} [30]. In addition to these visible PL assigned to Bi^{3+} and Bi^{2+}, the sample annealed in N_2 at 1300^oC exhibits NIR PL around 845 and 1410 nm. These PL emission bands have similar excitation bands around 374 and 420 nm.

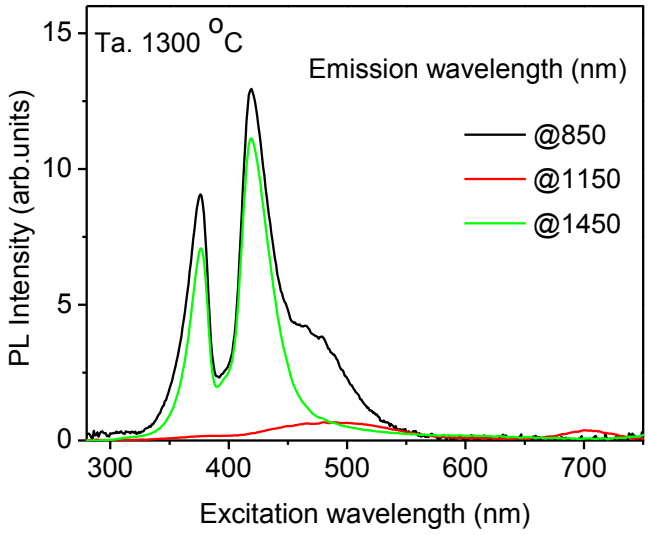

Figure 2.7: Excitation wavelengths dependence of PL intensity of the sample annealed in N_2 at 1300 ^oC. Scale up the intensity of PL for 1150 nm.

To elucidate the mechanism of NIR luminescence, the excitation wavelength dependence of the PL intensity is measured, as shown in Figure 2.7. At the emission wavelength of 1150 nm, we can see two broad PL excitation bands at 500 and 700 nm. This is very similar to those of Bi^{+} in multi-component glasses [17,27-28]. On the other hand, at the emission wavelengths of 850 nm and 1450 nm, sharp PL excitation bands at about 374 and 420 nm are observed. These bands are similar to the absorption bands in Bi doped porous silica glass [10]. Very recently, the similar absorption bands were reported in crystals and glasses, in which the absorption was ascribed to Bi dimer [31, 31]. Thus Bi dimer can be considered to be the origin of the PL emission bands at 850 nm and 1450 nm.

2.3.4.2 Annealing temperature dependence of PL

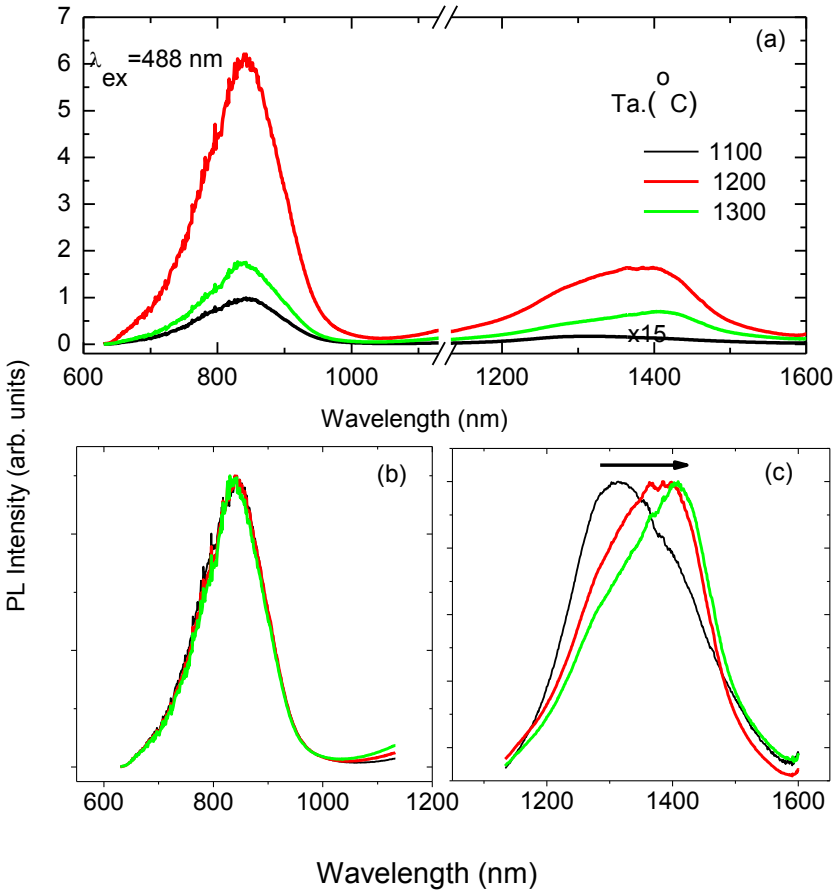

Figure 2.8: (a) NIR PL spectra of the sample at various annealing temperatures 1100-1300 ^{o}C in N_2 gas. (b) and (c) are the normalized spectra of NIR PL bands.

Figure 2.8(a) shows the PL spectra of Bi-doped porous silica annealed in N_2 from 1100 to 1300 ^oC. The excitation wavelength is 488 nm. We can see two broad PL bands. Both PL bands are strongest when the annealing temperature (Ta.) is 1200 ^oC. The full width at half maximum of the long wavelength side PL spectra at 1410 nm (annealing temperature is 1300 ^oC) is comparable to those reported for Bi-doped multi-component bulk glasses [17,28]. Figures 2.8(b) and 2.8(c) are the normalized spectra of the two PL bands. It is interesting that the shape of the shorter wavelength PL peak around 850 nm is independent of the annealing temperature, while that the longer wavelength PL peak shifts from 1310 to 1410 nm with increasing the annealing temperature. This result suggests that the PL intensity of Bi^+ (at around 1270 nm) decreases while that of Bi dimer (at around 1420 nm) increases with increasing the annealing temperature. This implies that Bi ions aggregate and becomes Bi dimer when the annealing temperature is high.

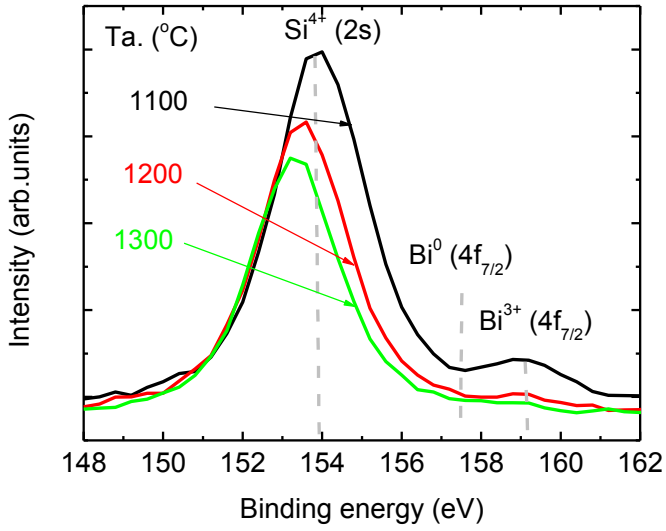

Figure 2.9: XPS spectra of Bi doped porous silica annealed in N_2 from 1100 to 1300 ^oC.

In order to clarify the valence state of Bi, the X-ray photoelectron spectroscopy (XPS) spectra are measured. Figure 2.9 shows the XPS spectra of Bi-doped porous silica annealed in N_2 from 1100 to 1300 ^oC. The samples show Si^{4+} (2s) peak and Bi^{3+} ($4f_{7/2}$) peak, which reveals that 3+ is the dominant valence state of Bi in these samples. Other valence states of Bi are under the detection limit. Unfortunately, due to the low Bi concentration, it is difficult to obtain more information on the valence states of Bi active centers. The XPS intensity of Bi^{3+} peak decreases with increasing the annealing temperature. This is probably due to the

evaporation of Bi during the annealing at high temperatures [27]. As shown in figure 2.8(a), the PL intensity at 845 and 1450 nm of our samples is the strongest when the annealing temperature is 1200 ^{o}C. Probably, this optimum annealing temperature is determined by the trade-off between the activation rate of Bi NIR active centers and evaporation of Bi during the high temperature annealing.

2.3.5 Temperature dependence of the NIR PL

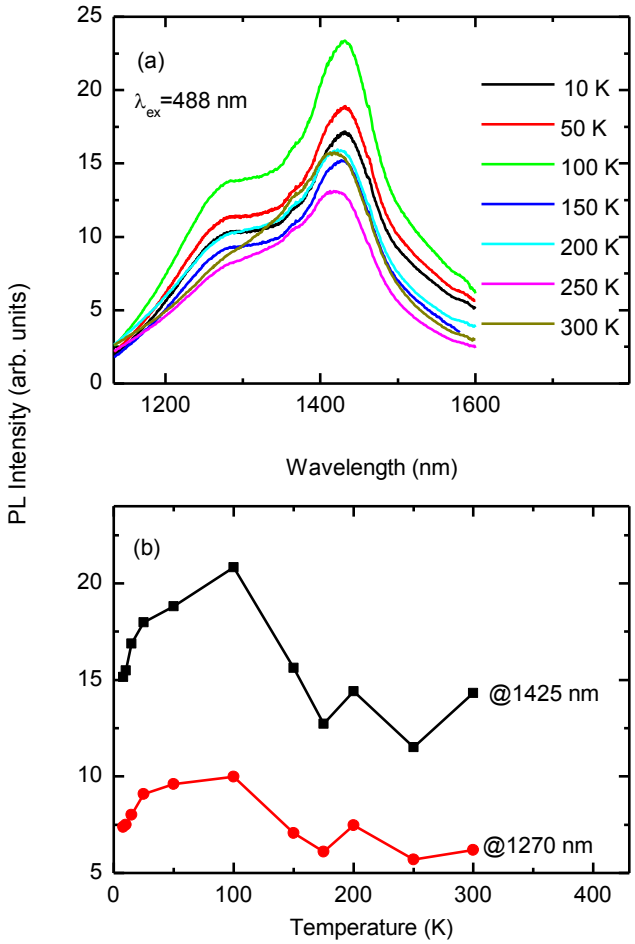

Figure 2.10: (a) IR PL spectra upon photo-excitation with a wavelength of 488 nm at various temperatures 10-300 K of the sample annealed in N_2 at 1300 ^{o}C. (b) Temperature dependence of integrated intensity of the two Gaussian peaks at 1270 and 1420 nm.

For further study of the NIR PL properties, the NIR PL spectra of the sample annealed at 1300 ^{o}C in N_2 atmosphere is measured as a function of temperature. Figure 2.10 shows the results. For all the temperatures, we can see broad NIR PL spectra. The PL spectra can be

decomposed into two Gaussian bands centered at 1270 and 1425 nm. The temperature dependence of the PL intensities of the two PL bands is shown in Fgure 2.10. Both the PL intensities first increases, and then decreases. Qualitatively similar results were reported in a previous work on the NIR PL from $Bi_4Ge_3O_{12}$ crystal [34]. In that work, the PL intensity increased as the temperature increases from 8 to 100 K, then the intensity dropped by 90% as the temperature raised to 300 K. On the other hand, in present work, it drops by only 40%. This small temperature quenching is a promising feature for applications such as optical amplifiers at optical telecommunication wavelengths.

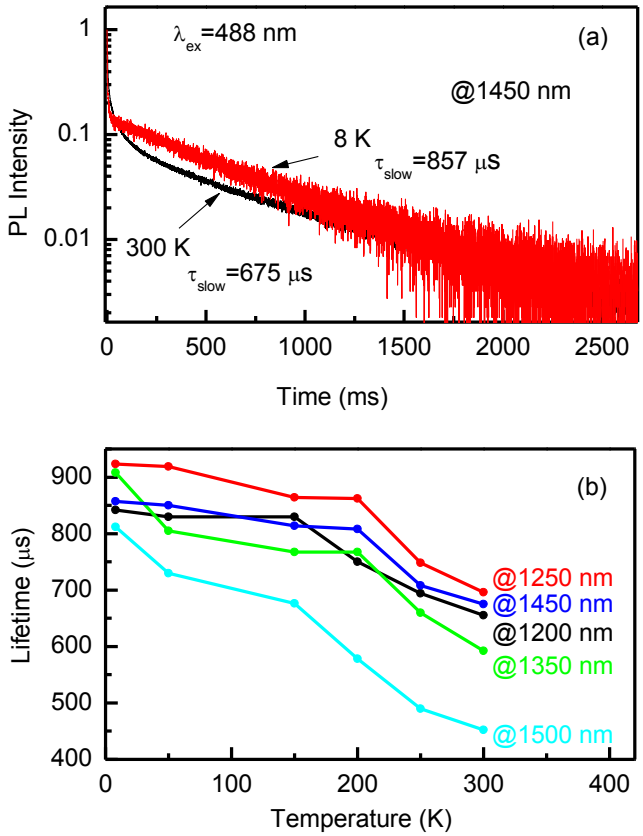

Figure 2.11: (a) decay curves of the sample annealed in N_2 at 1300 ^oC measured at 8 and 300 k, detection and excitation wavelengths are 1450 and 488 nm, respectively. (b) Temperature dependence of slow component's lifetimes at various detection wavelengths under the excitation wavelength of 488 nm.

To draw more information from the NIR PL properties, time resolved PL is measured as a function of temperature. Figure 2.11(a) shows decay curves of the sample annealed in N_2 at 1300 ^oC measured at 8 and 300 K. The detection and excitation wavelengths are 1450 and 488 nm, respectively. The PL decay curves consist of two components, i.e., fast and slow

components. The lifetime of the fast components is shorter than 4 μs, which is independent on the detection wavelengths (data was not shown). This component probably arises from defects in porous silica. The lifetime of the slow component at room temperature is 675 μs, which is comparable to those reported for Bi doped glasses and crystals. The lifetime increases to 857 μs at low temperature (8 K). In Figure 2.11(b), the lifetime of the slow component is plotted as a function of the temperature at various detection wavelengths (1200 – 1550 nm). At all the detection wavelengths, the lifetime decreases gradually with increasing the temperature. The decrease in the lifetime in the temperature range from 8 K to 300 K was about 30 %. This value is much smaller than that of $Bi_4Ge_3O_{12}$ crystal, which has been reported to be about 90 % [34]. The observed small temperature dependence of the lifetime is consistent with the small temperature quenching of the PL.

2.4 Conclusion

PL properties of Bi-doped oxidized porous Si thin films are studied for the first time. Two broad PL bands peaking at 845 nm under 488 nm excitation are observed. The PL spectra depend on the Bi concentration and oxidation temperature. The oxidation temperature dependence revealed that oxidation of silicon into silica is indispensable to activate the Bi NIR active centers in oxidized porous Si. Bi doped porous silica thin films are annealed at various temperatures in air or N_2 gas atmosphere. NIR PL of these samples is measured as a function of excitation wavelengths. It was found that the annealing in N_2 is necessary for the activating NIR emission from Bi in pure porous silica thin films. The multiple Bi centers would be stabilized in various forms as Bi^{3+}, Bi^{2+}, Bi^{+}, and Bi dimer. Robustness of NIR PL intensity against temperature is shown by measuring the steady state and time-resolved PL at 8 to 300 K.

References

[1] Y. Arai, T. Suzuki, and Y. Ohishi, Appl. Phys. Lett. **90**, 261110-1 (2007).

[2] G. A. Thomas, B. I. Shraiman, P. F. Glodis, and M. J. Stephen, Nature. **404**, 262 (2000).

[3] I. Razdobreev, L. Bigot, V. Pureur, A. Favre, G. Bouwmans, and M. Douay, Appl. Phys. Lett. **90**, 031103-1 (2007).

[4] I.A. Bufetov, E.M. Dianov, Laser Phys. Lett. **6**, 487 (2009).

[5] Y. Fujimoto and M. Nakatsuka, Jpn. J. Appl. Phys. **40**, 279 (2001).

[6] Y. Fujimoto and M. Nakatsuka, Appl. Phys. Lett. **82**, 3325 (2003).

[7] V. G. Truong, L. Bigot, A. Lerouge, and M. Douay, I. Razdobreev, Appl. Phys. Lett. **92**, 041908-1 (2008).

[8] V. V. Dvoyrin, V. M. Mashinsky, L. I. Bulatov, I. A. Bufetov, A. V. Shubin, M. A. Melkumov, E. F. Kustov, and E. M. Dianov, Opt. Express. **31**, 2966 (2006).

[9] J. Ren, J. Qiu, D. Chen, C. Wang, X. Jiang and C. Zhu, J. Mater. Res. **22**, 1953 (2007).

[10] I. Razdobreev, H. El Hamzaoui, V. Yu. Ivanov, E. F. Kustov, B. Capoen, and M. Bouazaoui1, Opt. Lett. **35**, 1341 (2010).

[11] P. Nebolova , J. Spirkova , V. Perina , I. Jirka , K. Mach ,G. Kuncova, Solid State Ionics. **141–142**, 609 (2001).

[12] M. Balucani, V. Bondarenko, G. Lamedica, A. Ferrari, L. Dolgyi, N. Vorozov, V. Yakovtseva, S. Volchek, V. Petrovich, N. Kazuchits, Thin Solid Films. **396**, 201 (2001).

[13] E.J.Teo, A.A.Bettiol, P.Yang, M.B.H.Breese, G.Z.Mashanovich, W.R.Headley, and G.T.Reed, Opt. Lett. **34**, 659 (2006).

[14] V. Bondarenko, N. Kazuchits, M. Balucani, A. Ferrari, Opt. Mater. **27**, 894 (2005).

[15] A. Najar, J. Charrier, H. Ajlani, N. Lorrain, H. Elhouichet, M. Oueslati, L. Haji, J. Lumin. **121**, 245 (2006).

[16] V. Sokolov, V. Plotnichenko, and E. Dianov, Opt. Lett. **33**, 1488 (2008).

[17] X. Meng, J. Qiu, M. Peng, D. Chen, Q. Zhao, X. Jiang, and C. Zhu, Opt. Express. **13**, 1635 (2005).

[18] I. Razdobreev, H. El Hamzaoui, V. Ivanov, E. Kustov, B. Capoen, and M. Bouazaoui1, Opt. Express. **35**, 1341 (2010).

[19] Sa chu rong gui, K. Imakita, M. Fujii, Z. Bai, and S. Hayashi, Opt. Mater. **34**, 1161 (2012).

[20] L. Luo, X. Zhang, K. Li, K. Cheah, J. Shi, W. Wong, and M. Gong, Adv. Mater. **16**, 1664 (2008).

[21] N. Ishikura, M. Fujii, K. Nishida, S. Hayashi, and J. Diener, Opt. Express. **16**, 15534 (2008).

[22] L. Meng , C. P. Moreira de Sa and M. P. dos Santos, Thin Solid Films. **239**, 117 (1994).

[23] T. Nakamura, T. Ogawa, N. Hosoya, S. Adachi, Journal of luminescence **130**, 682 (2010).

[24] S. Shichi, M. Fujii, and S. Hayashi, Opt. Lett. **36,** 1 (2011).

[25] D. Xu, G. Guo, L. Gui, and Y. Tang, J. Phys. Chem. B **103**, 5468 (1999).

[26] P. Yu, L. Su, Q. Wang, H. Zhao, X. Guo, Q. Yang, and J. Xu, Nuclear Instruments and Methods in Physics Research A. **631**, 40 (2011).

[27] H. Sun, A. Hosokawa, Y. Miwa, F. Shimaoka, M. Fujii, M. Mizuhata, S. Hayashi, and S. Deki, Adv. Mater. **21**, 3694 (2009).

[28] S. Zhou, N. Jiang, B. Zhu, H. Yang, S. Ye, G. Lakshminarayana, J. Hao, and J. Qiu, Adv. Funct. Mater. **18**, 1407 (2008).

[29] G. Boulon, B. Moine, and J. Bourcet, Phys. Rev. B. **22**, 1163 (1980).

[30] G. Blasse, A. Meuerink, M. Nommes, and J. Zuidema, J. Phys. Chem. Solids. **22**,171 (1994).

[31] L. Su, H. Li, L. Zheng, X. Fan, X. Jiang, H. Tang, G. Ren, J. Xu, W. Ryba-Romanowski, R. Lisiecki, and P. Solarz, Opt. Mater. Express. **2**, 757 (2012).

[32] V. Sokolov, V. Plotnichenko, V. Koltashov and E. Dianow, J. Phys. D: Appl. Phys. **42**, 095410 (2009).

[33] J.C. Vial, S. Billat, A. Bsiesy, G. Fishman, F. Gaspared, R. Herino, M. Ligeon, F. madeore, I. Mihalcescu, F. Muller and R. Romestain, Phyisica B **185**, 593 (1993).

[34] P. Yu, L. Su, Q. Wang, H. Zhao, X. Guo, Q. Yang, and J. Xu, Nuclear Instruments and Methods in Physics Research A. **631**, 40 (2011).

Part Ⅱ

Photosensitization of rare earth ions by silver cluster/ions in zeolites

Chapter 3

Photosensitization of Eu ions by Ag clusters in zeolite Y

In this chapter, photosensitization of trivalent europium (Eu^{3+}) ions by silver (Ag) clusters is achieved by simultaneously doping Eu and Ag in zeolite cages. The photoluminescence (PL) due to the $^5D_0 \rightarrow ^7F_2$ transition of Eu^{3+} ions at 613 nm is significantly increased by the presence of Ag clusters. The excitation wavelength dependence of the PL intensity coincided well with the absorption spectrum of Ag clusters, indicating that Eu^{3+} ions are excited by the energy transfer from Ag clusters.

3.1 Introductions

Rare-earth (RE) ions are well-known fluorescence materials, which are practically used for many kinds of commodities, such as lighting, display, laser and so on [1-5]. Most of them show sharp luminescence arising from the intra-4f shell transitions. Past years, the optical properties of Eu^{3+} ions doped into various host materials have been extensively studied since the Eu^{3+} ion is a best choice for red emitting phosphors in white light emitting diodes (LEDs) [4]. However, the optical absorption of the Eu^{3+} ion is very week. Since the 4f shell of RE ions is shielded by outer shells, the luminescence is little affected by their surrounding environment, and thus highly efficient in a variety of host materials [6, 7]. Recently, Eichelbaum et al. [8] reported that PL of RE ions in silicate glasses were significantly enhanced by metal clusters precipitated by synchrotron X-ray irradiation. The enhancement was found to be energy transfer from metal clusters to RE ions. Their results indicate that

metal clusters have a great potential to enhance the effective excitation cross section of RE ions, which is intrinsically small due to the dipole forbidden process.

In the chapter, zeolite as a host material to study the photosensitization effect of metal clusters. Zeolite, possessing a cage structure consisting of orthosilicate ion (SiO_4^{4-}) and orthoaluminate ion (AlO_4^{5-}) structural units, is one of the most suitable host materials for the formation of metal clusters [9-12]. Metal clusters are known to be chemically stable in the nano-sized pores in the cage, and can be formed by a simple ion exchange process followed by a thermal treatment [13-16]. In this chapter, the effect of Ag clusters on the PL properties of Eu ions in zeolite is investigated for the first time. PL of Eu ions in the visible region can be significantly increased by Ag clusters in zeolite, due to the photosensitization effect. The results suggest that zeolite is a promising host material for the sensitization of RE ions by metal clusters.

3.2 Experimental details

Eu and Ag doped zeolite is prepared by an ion exchange process. The NH_4 form of faujasite-type zeolite (zeolite Y, SiO_2/Al_2O_3 = 7) is purchased from Tosoh Co. Japan. As shown in Figure 3.1, the average diameter of particles zeolite is about 800 nm. The zeolites are stirred in the aqueous solution of $EuCl_3.6H_2O$ at room temperature for 24 h. The products are filtered, washed with deionized water, and dried in air at 100 ^oC. To activate the Eu ions, the Eu doped zeolite (zeolite:Eu) is annealed in air at 800 ^oC for 2 h. The crystalline structure of zeolite Y is not destroyed at this temperature as confirmed by a XRD measurement [17]. For Ag doping, zeolite:Eu is stirred in aqueous solution of $Ag(NH_3)^{2+}$ at 70 ^oC for 24 h. $Ag(NH_3)^{2+}$ is prepared by reaction of Ag nitrate with aqueous ammonia [10]. After 24 h of stirring, Eu and Ag codoped zeolites (zeolite:Eu,Ag) are filtered, washed and dried in air at 100 ^oC for 24 h. The co-doped zeolite powders are then annealed at 350 ^oC for 1 h in air. This low temperature annealing forms Ag clusters in the cages of zeolite [13,18]. As a reference sample, Ag singly doped zeolites (zeolite:Ag) are also prepared, and annealed at from 300 to 600 ^oC. The sample preparation process was illustrated in Figure 3.2. It is possible for Eu ions to migrate into the sodalite cages by annealing at 800 ^oC [19]. The Ag clusters are most possible to be formed in small cage: prism [13, 20-21]. The concentrations of Eu and Ag in zeolites are determined by energy-dispersive x-ray spectroscopy (EDS). Concentration of doped Ag is varied from 4.7 to 6.8 at.% by changing Ag concentration in doping solutions. The concentration of Eu is varied from 1.0 to 2.0 at.% , which is also controlled by changing Eu concentration in doping solutions. The samples are kept in air. PL spectra are measured by a spectrophotometer (Horiba Jobin Yvon, Flourolog). The diffuse reflectance spectra are measured by a UV-VIS-NIR spectrophotometer (Shimadzu, Solid Spec-3700) and the data are

converted using the Kubelka–Munk function. Morphologies of the samples are studied by a field emission scanning electron microscopy (FE-SEM) (JEOL, JSM-7001F).

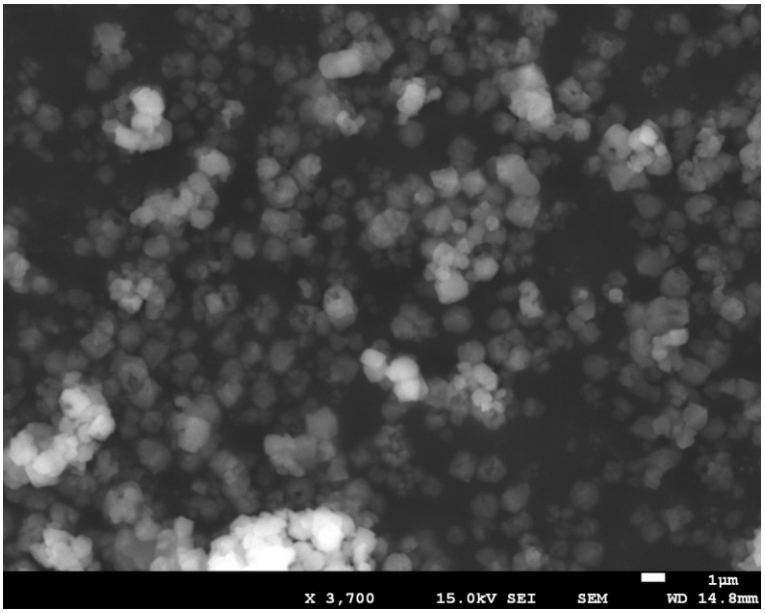

Figure 3.1: FE-SEM image of zeolite.

Time resolved PL spectra are measured by a monochromator equipped with a charge-coupled device with an image intensifier (ICCD) (Princeton Instrument, PI-Max). The third harmonic of a Nd:YAG laser (355 nm, pulse width 5 ns, repetition frequency 20 Hz) is used as the excitation source. The ICCD array is gated by a trigger signal from the exciting laser. The time resolution of the measurement system is 5 ns. For these optical measurements, the powder is put in a sample holder loosely. All the measurements are carried out at room temperature.

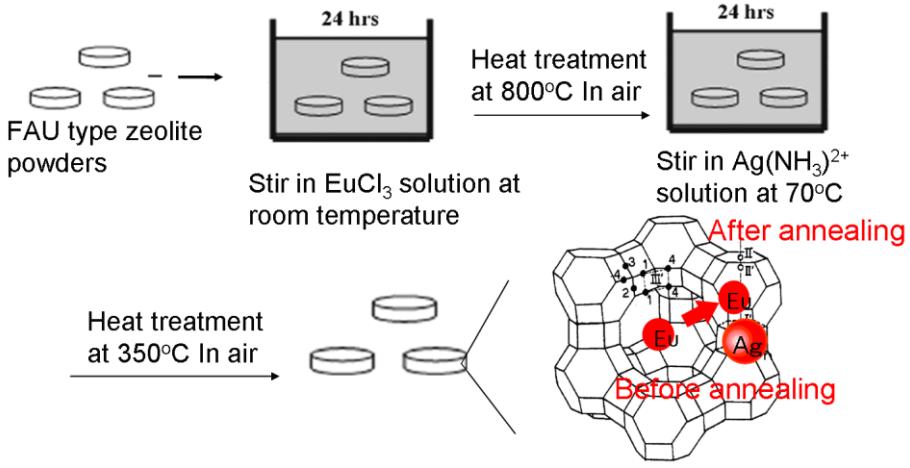

Figure 3.2: Schematic of the sample preparation procedures.

The external quantum efficiency (EQE) is determined by an integrating sphere method [20]. The measurement set up is similar to that in the report [20]. Excitation is provided by Hd-Cd laser (325 nm). The schematic view of the experiment is shown in Figure 3.3. To measure the EQE, three steps are performed. First (a), a Teflon sample holder (without sample) is positioned inside the integrating sphere; the exact incident photon flux at the excitation wavelength (La) and the background signal at the emission wavelengths can be observed from this measurement. Afterward (b and c), the sample holder is filled with the samples. The excitation and emission intensity of the sample is measured when the sample is out and in the laser beam. These two steps measurements yield the photon flux not absorbed by the sample at excitation wavelengths due to indirect (Lb) and direct absorption (Lc) and the photon flux emitted by the sample at emission wavelengths (Pb and Pc) (Figure 3.4), and the EQE is calculated using Equation 1.

$$\eta_{ext} = \frac{P_c - (1-A)P_b}{L_a A}$$

$$Where, A = 1 - \frac{L_c}{L_b}$$

Eq.1

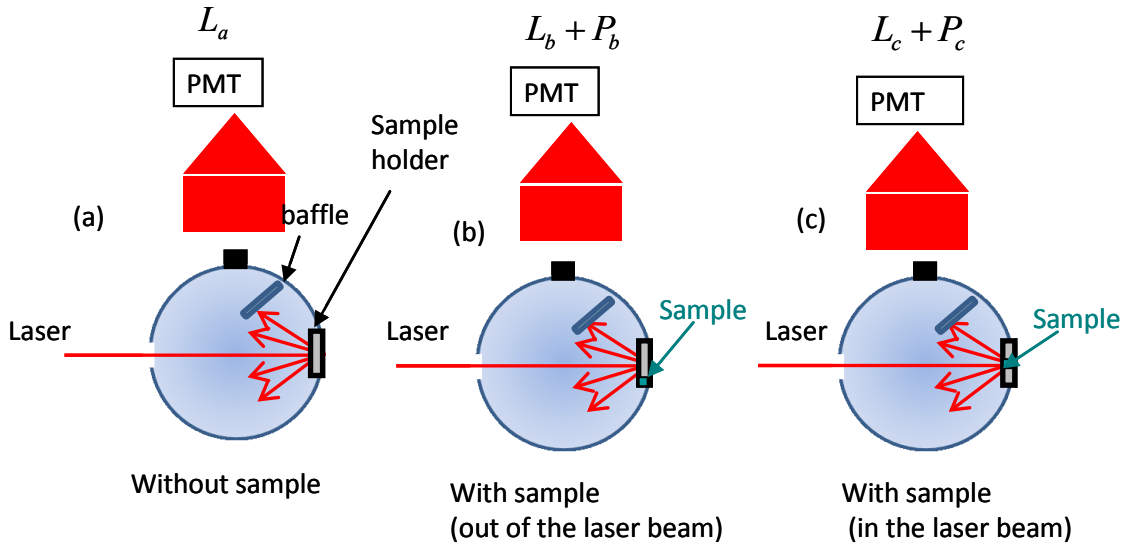

Figure 3.3: schematic view of EQE measurement.

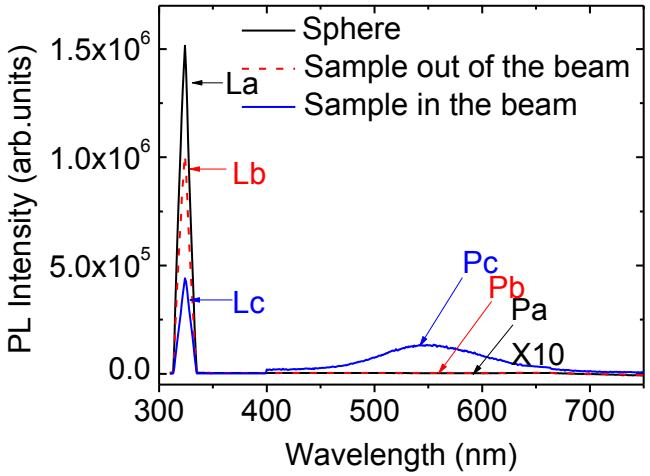

Figure 3.4: PL spectra of the EQE measurement of the sample zeolite:Eu(1.0),Ag(6.1). (L) Excitation range and (P) emission range. Excitation wavelength is 325 nm.

3.3 Results and discussion

3.3.1 Ag singly doped zeolite Y

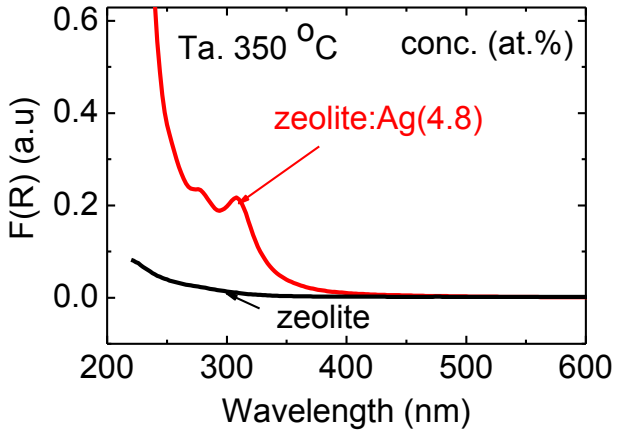

Figure 3.5: Diffuse reflectance ultraviolet to visible spectra, plotted as the Kubelka-Munk function (F) of the reflectance (R) of zeolite, zeolite:Ag(4.8).

The color of the annealed high concentration Ag doped zeolite sample is brownish, while it is white looking for the low concentration samples. The ultraviolet (UV) to visible diffuse reflectance spectra plotted as the Kubelka-Munk function (F) of the reflectance (R) of zeolite, zeolite:Ag(4.8), are shown in Figure 3.5. The numbers in the parentheses represent the Ag

concentration (at. %). The annealing temperature of the samples is 350 °C. Zeolite shows a very weak absorption band below 300 nm. Zeolite:Ag(4.8) exhibits a broad strong UV absorption around 310 nm. This peak is very similar to that reported for Ag clusters in hydrated zeolite Y. In Ref. [16], Ag_2 has been proposed as the possible origin of the absorption, which was formed by an Ag atom and an Ag ion. In other reports [13, 21], Ag_3 has been also proposed as possible Ag clusters in hydrated zeolite Y, which are formed by a Ag atom in prism and two Ag ions in sodalite cages in zeolite Y (see Figure 1.16). The cluster configuration still seems controversial, however, it is generally accepted that the absorption arises from Ag clusters. Note that Ag ions in hydrated zeolite Y show the absorption only below 250 nm, which is quite different from that observed in this work [22, 23]. Thus Ag ion is not considered to be the origin of the absorption.

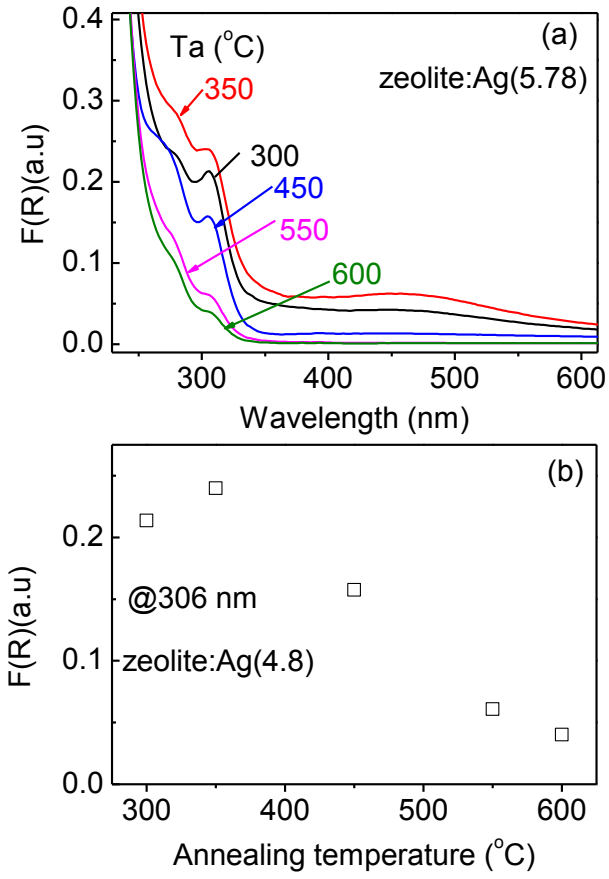

Figure 3.6: Diffuse reflectance ultraviolet to visible spectra, plotted as the Kubelka-Munk function (F) of the reflectance (R) of zeolite:Ag(4.8) under various annealing temperature.

Annealing temperature dependence of the UV to visible diffuse reflectance spectra plotted as the Kubelka-Munk function (F) of the reflectance (R) of zeolite:Ag(5.78), are shown in Figure 3.6(a). The UV absorption peak almost does not depend on the annealing temperature. The optimum annealing temperature for the absorbance at about 310 nm is 350 ^{o}C. In the Figure 3.6(b) plotted the annealing temperature dependence of the absorbance at 310 nm. It is indicated that the absorbance strongly depends on the annealing temperature, which first increases and then decreases with increasing the annealing temperature. This suggests that the Ag cluster is not stable under high temperature annealing. It is consistent with the results of previous report [24].

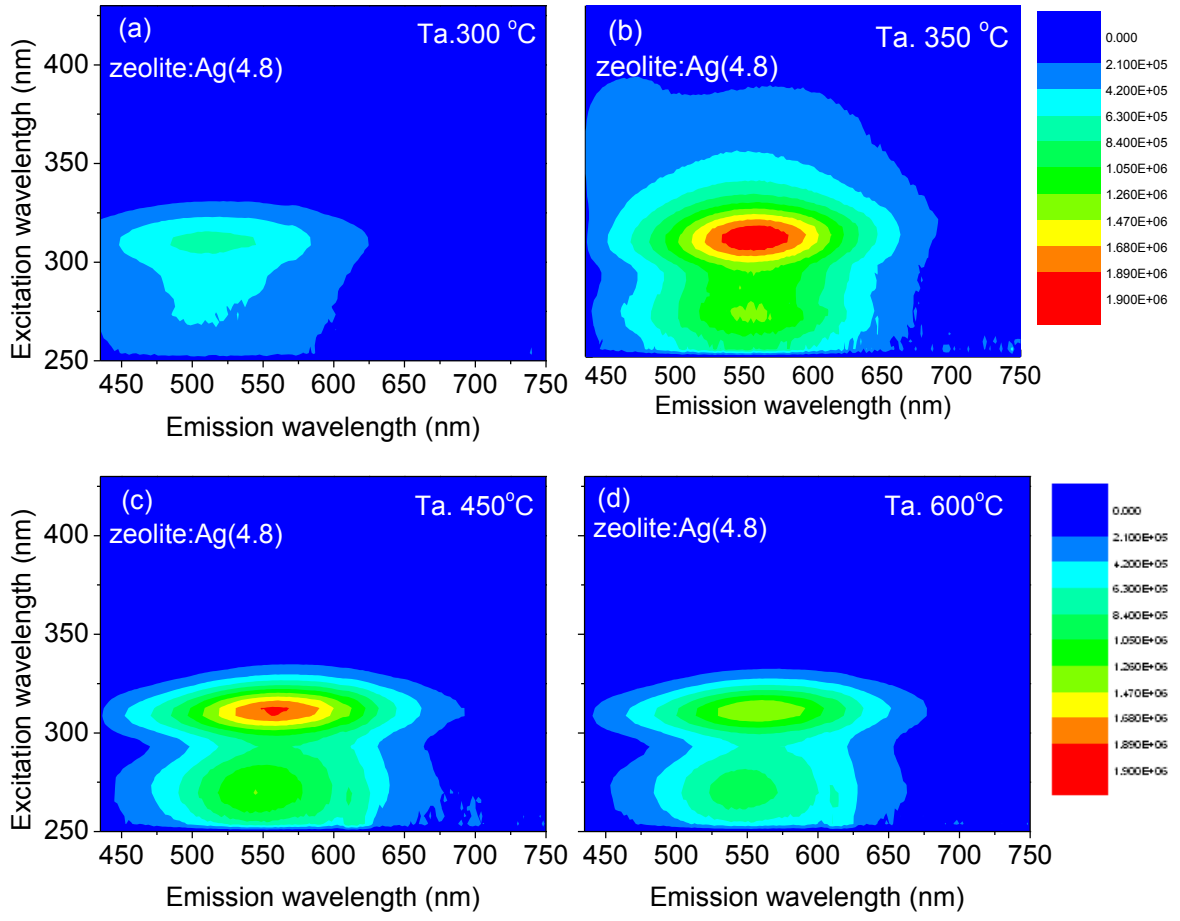

Figure 3.7: 2D exciation-emisson graph of zeolite:Ag(4.8) annealed from 300 to 600 ^{o}C.

Generally, the rehydrated white looking powders are known to hardly fluorescence. Fortunately, strong luminescence under low-power UV excitation is observed in our samples (Figure 3.7). 2D exciation-emisson graphs of zeolite:Ag(4.8) under various annealing

temperature are measured. All the graphs show a broad emission band around 550 with an excitation band around 310 nm. In common, which is very similar to that observed for Ag clusters in zeolite Y prepared in a similar method [13, 21]. The excitation band is consistent with the position of Ag absorption in zeolite Y, as shown in Figure 3.5. The position of excitation-emission bands almost do not depend on the annealing temperature. However, the intensity strongly depends on the annealing temperature, which first increase and then decrease with increasing the annealing temperature. This indicates that the number of Ag cluster reaches maximum at lower temperature 350°C.

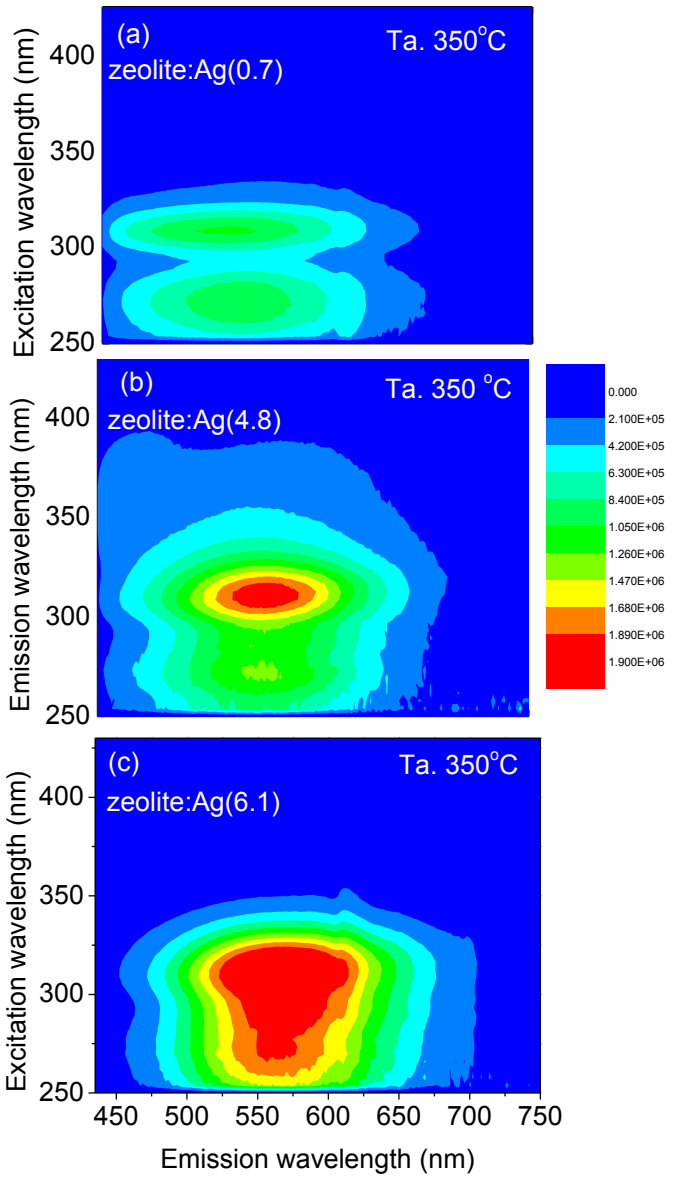

Figure 3.8: 2D exciation-emisson graph of zeolite:Ag with Ag concentration from 0.7 to 6.1 at.%.

2D emission-excitation graph of the Ag singly doped sample with various Ag concentrations are also measured, as shown in Figure 3.8. Ag concentration is changed from 0.7 to 6.1 at.%. The emission and the excitation bands do not depend on the Ag concentration, which is consistent with the previous reports [13]. But the emission intensity strongly depends on the Ag concentration, which reached maximum in zeolite:Ag(6.1).

3.3.2 Eu and Ag co-doped zeolite Y

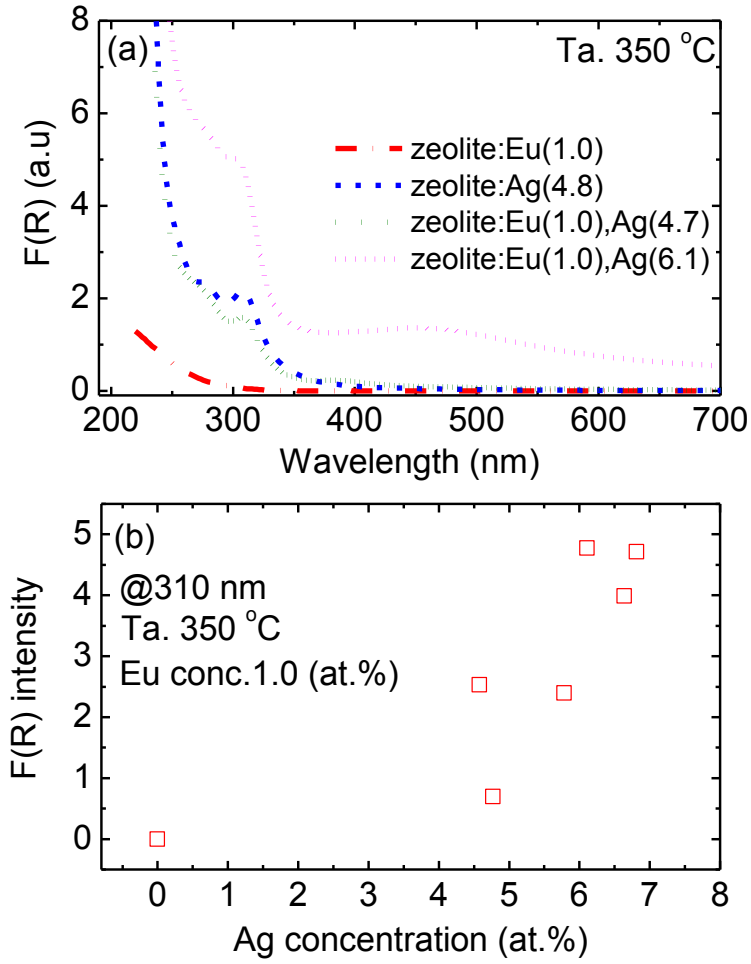

Figure 3.9: (a) UV-visible diffuse reflectance spectra, plotted as the Kubelka-Munk function (F) of the reflectance (R) of zeolite:Eu(1.0), zeolite:Ag(4.8) and zeolites:Eu,Ag. (b) F(R)

intensity (absorption optical intensity) versus plotted as a function of Ag concentration of zeolite:Eu,Ag.

The ultraviolet to visible (UV-visible) diffuse reflectance spectra plotted as the Kubelka-Munk function (F) of the reflectance (R) of zeolite:Eu(1.0), zeolite:Ag(4.8), zeolite:Eu(1.0),Ag(4.7) and zeolite:Eu(1.0),Ag(6.1) are shown in Figure 3.9(a). Zeolite:Eu(1.0) has a weak absorption band below 300 nm due to the charge transfer state of O^{2-} to Eu^{3+} [4]. Zeolite:Ag(4.8) and zeolite:Eu(1.0),Ag(4.7) exhibits a strong and broad UV absorption around 310 nm of Ag cluster. In addition to the 310 nm peak, the high concentration sample zeolite:Eu(1.0),Ag(6.1) has a broad absorption band around 450 nm, which can be assigned to the surface plasmon resonance of Ag nanoparticles (NPs) [25, 25]. To clarify the Ag NPs formation, the morphology of the sample is observed by FE-SEM measurement. The FE-SEM images of zeolites (a) and zeolite:Eu(1.0),Ag(6.1) (b) are shown in Figure 3.10. Large Ag NPs are observed at the surface of crystals. In Figure 3.9(b), the values of F(R) at 310 nm are plotted as a function of the Ag concentration. While the Eu concentration is fixed to 1.0 at. %, the increase of the F(R) value with increasing the Ag concentration can be seen.

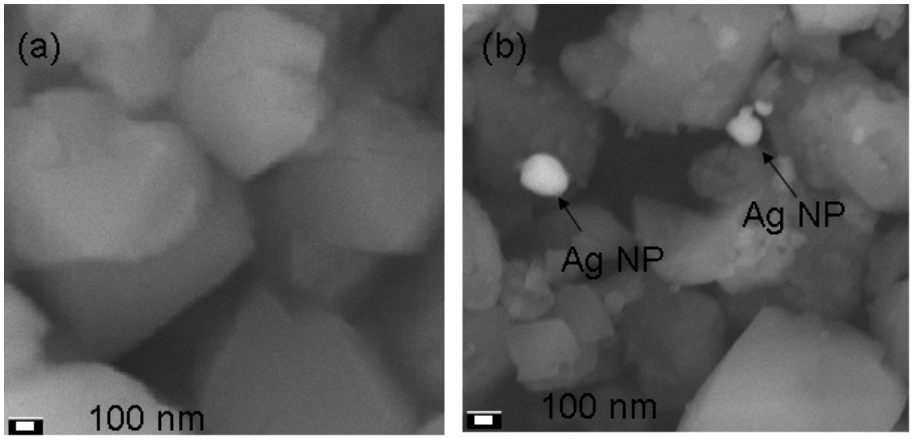

Figure 3.10: FE-SEM image of (a) zeolites and (b)zeolite:Eu(1.0)Ag(6.1).

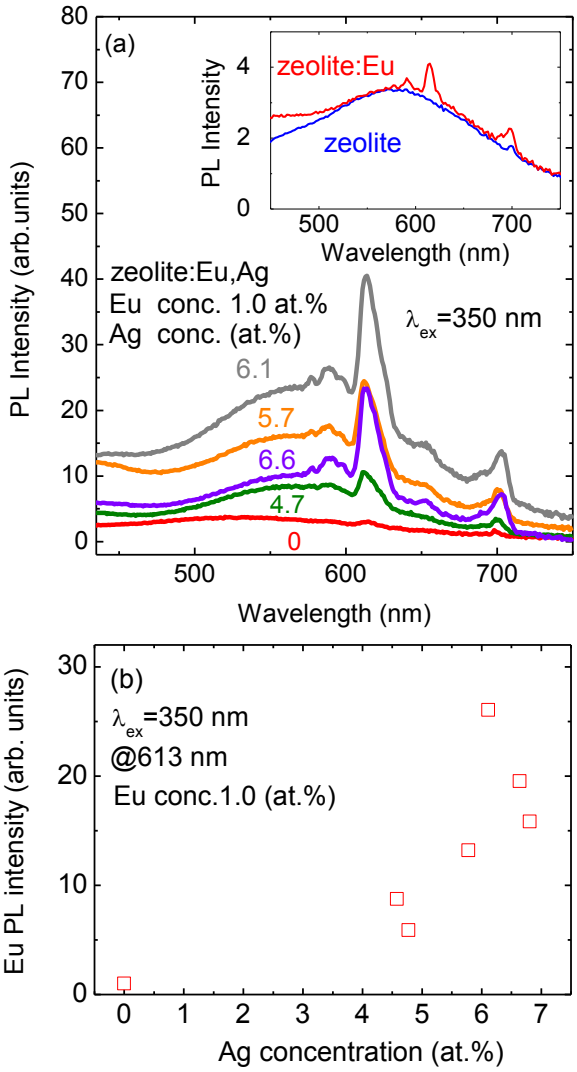

Figure 3.11: (a) PL spectra of zeolite, zeolite:Eu and zeolite:Eu,Ag of various Ag concentrations. The inset of the figure is enlarged PL spectra of zeolite and zeolite:Eu. (b) Ag concentration dependence of Eu-PL intensity.

Figure 3.11(a) shows the PL spectra of the zeolite:Eu,Ag. The Eu concentration is fixed at about 1.0 at.%, and the Ag concentration is changed from 0 to 6.8 at.%. The excitation wavelength is 350 nm. The PL of the sample without Ag doping zeolite: Eu(1.0) is enlarged in the inset of the Figure 3.11(a), together with that of zeolites as a reference. The zeolite shows weak and broad PL centered around 570 nm, which probably arises from oxygen-vacancies in the zeolite [27]. In addition, zeolite:Eu(1.0) shows a sharp PL peak around 613 nm due to the $^5D_0 \rightarrow {}^7F_2$ transition of Eu^{3+} ions (Eu-PL). In zeolite:Eu,Ag samples,

a broad PL centered at 550 nm is observed and the intensity increases with increasing Ag concentration. In the same way of the increase of the 550 nm band, Eu-PL at 613 nm increases with increasing Ag concentration. Figure 3.11 (b) shows the integrated Eu-PL intensitiy as a function of Ag concentration. The intensity is normalized to that of zeolite:Eu(1.0). We can see that the Eu-PL is at most 27 times increased by co-doping Ag. The Ag concentration dependence of the Eu-PL intensity is very similar to that of the absorbance in Figure 3.9(b). This strongly suggests that Ag clusters sensitize Eu ions and increase the effective excitation cross section.

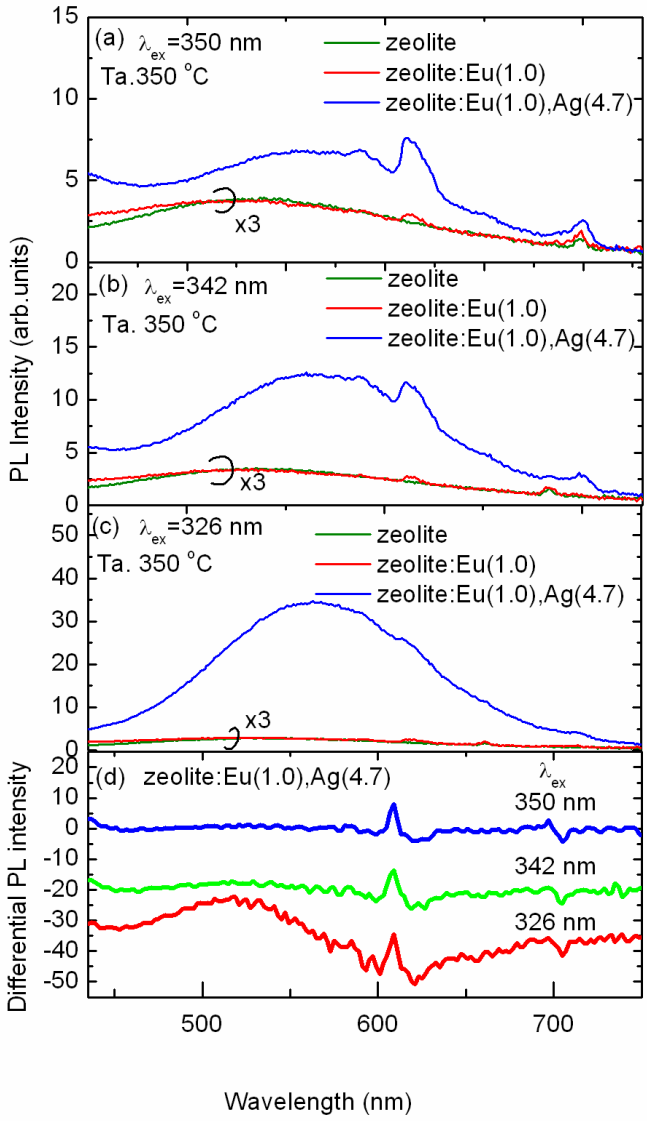

Figure 3.12: (a-c) PL spectra of zeolite, zeolite:Eu(1.0), and zeolite:Eu(1.0),Ag(4.7) under the

excitation of 350, 342, and 326 nm. (d) First derivative PL spectra of zeolite:Eu(1.0),Ag(4.7) at various excitation wavelengths.

To elucidate the mechanism causing the increase in PL, the excitation wavelength dependence of the PL spectra is studied. Figure 3.12(a-c) shows the PL spectra of zeolite, zeolite:Eu(1.0) and zeolite:Eu(1.0),Ag(4.7) excited at 350, 342, and 326 nm, respectively. Note that the PL spectra of zeolites and zeolite:Eu(1.0) are multiplied by a factor of 3. When the excitation wavelength is 350 and 342 nm, we can clearly see that the Eu-PL intensity is significantly increased by co-doping Ag. With decreasing excitation wavelengths, the Ag-PL grows very rapidly, and as a result the Eu-PL is almost smeared when excited at 326 nm. In order to estimate the relative intensity of the Eu-PL hidden by the strong background of the Ag-PL, the spectra are differentiated, as shown in Figure 3.12(d). A sharp peak at 613 nm can be seen in the first derivative spectra for all the excitation wavelengths. The derivative technique is known to be an effective tool for quantitative analysis of PL spectra from mixtures of fluorescent compounds [28]. The amplitude of the first derivative spectra depends only on the intensity of the PL if the PL spectral shape is identical. This assumption is in general applicable to the PL from trivalent rare-earth ions. The excitation wavelength dependence of the Eu-PL intensity at 613 nm estimated from the first derivative PL spectra is shown in Figure 3.13. Zeolite:Eu(1.0) has a broad excitation band below 280 nm and two sharp peaks at 320 nm and 394 nm. The sharp peaks at 320 nm and 394 nm correspond to the $^7F_0 \rightarrow ^5H_6$ and $^7F_0 \rightarrow ^5L_6$ transitions of Eu^{3+}, respectively [29, 30]. The broad excitation band below 280 nm is due to the energy transfer from the charge transfer state of O^{2-} to Eu^{3+} [4, 30]. The excitation spectrum of codoped sample zeolite:Eu(1.0),Ag(4.7) is different from that of zeolite:Eu(1.0). It has a very broad PL excitation band and the intensity is much stronger than that of zeolite:Eu(1.0) in the whole wavelength range. The ratio of the Eu-PL intensity of zeolite:Eu(1.0),Ag(4.7) to that of zeolite Eu(1.0) at the same wavelengths are shown in Figure 3.13 on the right axis. An increase in intensity of up to five times in the excitation region centered at around 330 nm is observed. Note that the sharp dip in the Eu-PL intensity ratio around 320 nm is due to the increased PL intensity of zeolite:Eu(1.0).

Comparison between the excitation wavelength dependence of the Eu-PL intensity ratio and the absorption spectra in Figure 3.9 reveals that the PL increase at wavelengths where Ag cluster show absorption. This is clear evidence that the PL increase is due to energy transfer from Ag clusters to Eu ions. The simple energy transfer process was illustrated in Figure 3.14. Ag clusters absorb excitation photons more efficiently than Eu^{3+}, and transfer the excitation energy to Eu^{3+}. The strong increase of the Eu-PL indicates that the energy transfer is the dominant excitation process for Eu^{3+}.

The EQEs of the zeolite:Ag and zeolite:Eu,Ag are measured by the integrating sphere method (as shown Figure 3.3). The EQE of zeolite:Ag (4.8), zeolite:Eu(1.0),Ag(4.7), and zeolite:Eu(1.0),Ag(6.1) are found to be approx 19%, 15% , and 17%, respectively. The values are comparable to those of a previous report [20].

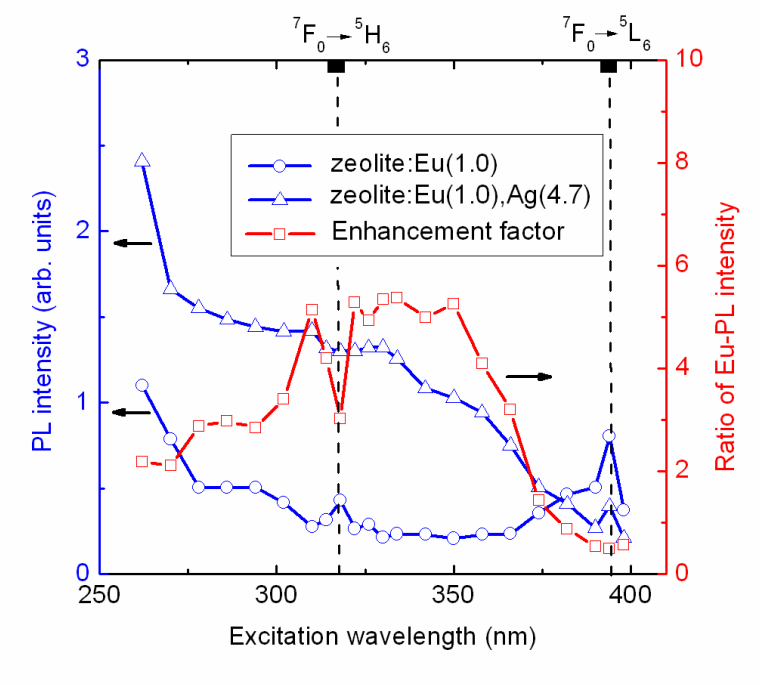

Figure 3.13: The excitation wavelengths dependence of Eu-PL intensity of zeolite:Eu(1.0) and zeolite:Eu(1.0),Ag(4.7), right axis is the ratio of Eu-PL intensity of zeolite:Eu,Ag to that of zeolite:Eu.

To study the energy transfer process in detail, time-resolved PL measurements at excitation of 355 nm are performed. The time-resolved PL spectra of zeolite:Eu(0.1),Ag(4.7) are shown in Figure 3.15. When the delay time is 8 μs, the spectrum is dominated by the broad Ag-PL. The sharp Eu-PL emerges with increasing delay time and it is still observed when delay time is 1928 μs. Figure 3.16(a) shows a PL decay curve of Ag-PL at 520 nm for zeolite:Ag(4.8) and zeolite:Eu,Ag with an Ag concentration of 6.1 at.% and Eu concentration from 1.4 to 2.0 at. %. The decay curves show a fast and a slow component. The decay time of the fast and slow components estimated by fitting the curves to a bi-exponential function is plotted as a function of Eu concentration in Figure 3.16(b). In zeolite:Ag(4.8), the lifetimes of the slow and the fast components are 129 and 12 μs, respectively. By doping Eu, the lifetimes first increase and then decrease with increasing Eu concentration. The increase of the lifetime

may be due to the quenching of nonradiative processes of Ag clusters by isolating them from water molecules by Eu co-doping. The shortening of the lifetime for the Eu concentrations above 1.4 at.% is probably due to the energy transfer from Ag clusters to Eu^{3+} ions. It should be noted here that the observed lifetime is much longer than that reported in previous work (~a few ns) [13, 31]. The fast PL can't be observed because our time resolution (5 ns) is slower than the lifetime. The fast component may also contribute to the energy transfer.

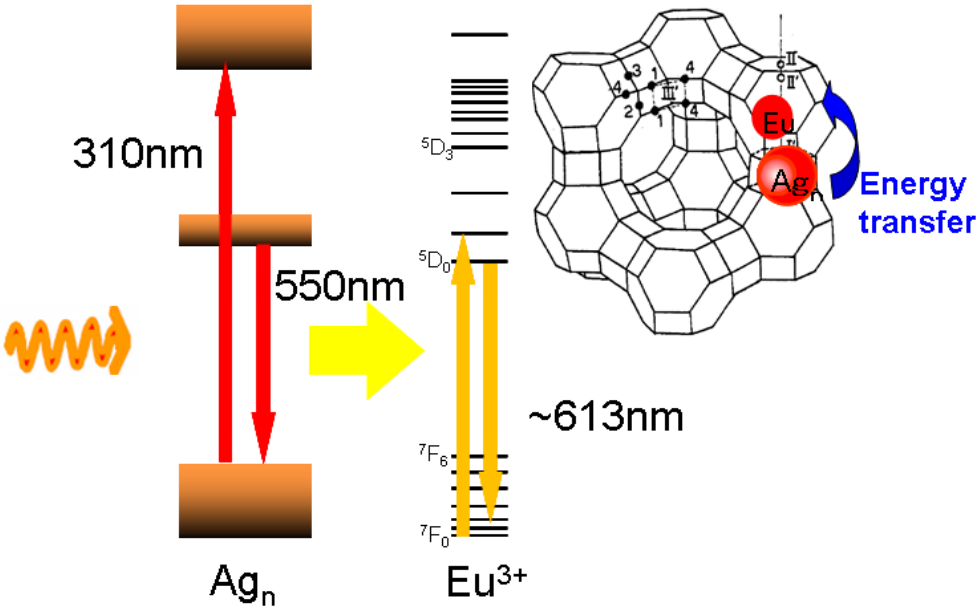

Figure 3.14: Schematic illustrations of the energy transfer process from Ag clusters to Eu^{3+}.

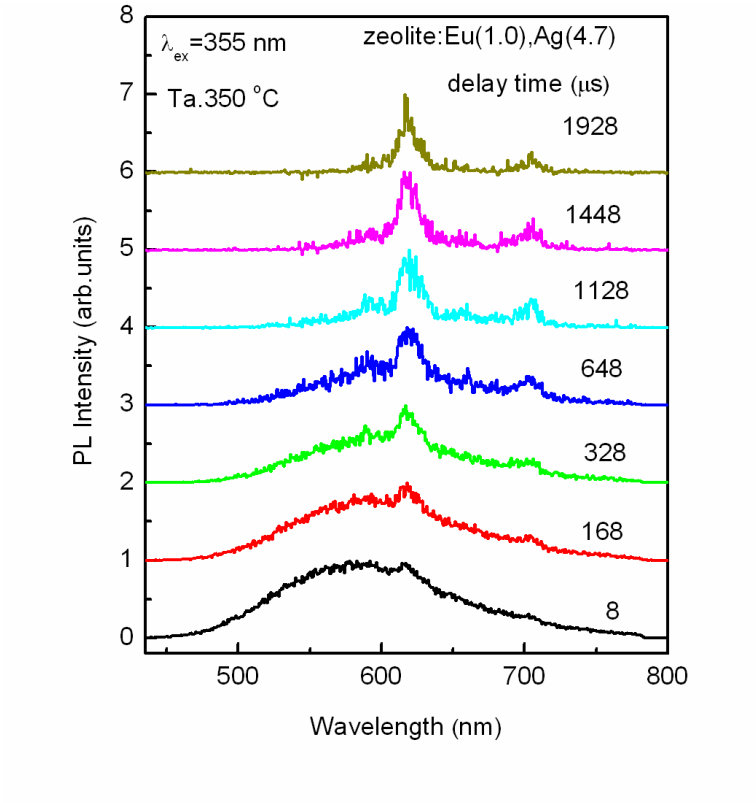

Figure 3.15: Time resolved PL spectra of zeolite:Eu(1.0),Ag(4.7) upon different delay times excited by 355 nm.

In Figure 3.16(c), the PL decay curves of Eu-PL at 617 nm are shown. The Eu concentration is about 1.0 at.% for all the samples and the Ag concentration is changed from 4.7 to 6.1 at.% for the zeolite:Eu,Ag samples. To isolate the Eu-PL from Ag-PL, the background determined from the PL intensities at 604 and 631 nm is subtracted from that at 617 nm. The lifetimes, defined by the time where the PL intensity decreases to 1/e, are plotted as a function of the Ag concentration in Figure 3.16(d). Without Ag doping, the lifetime is about 105 μs. It increases to about 600 μs by co-doping Ag and is almost independent of the Ag concentration. The reason for the increase of the lifetime is considered to be similar to that in the Figure 3.16(b). Ag co-doping may change the environment of Eu^{3+} ions in zeolite cages and may quench nonradiative processes of Eu^{3+} ions by isolating them from water molecules. It is noted here that we could not see a rising part in the time transient of Eu-PL in Figure 3.16(c). This is probably due to strong back ground luminescence from Ag clusters and zeolite.

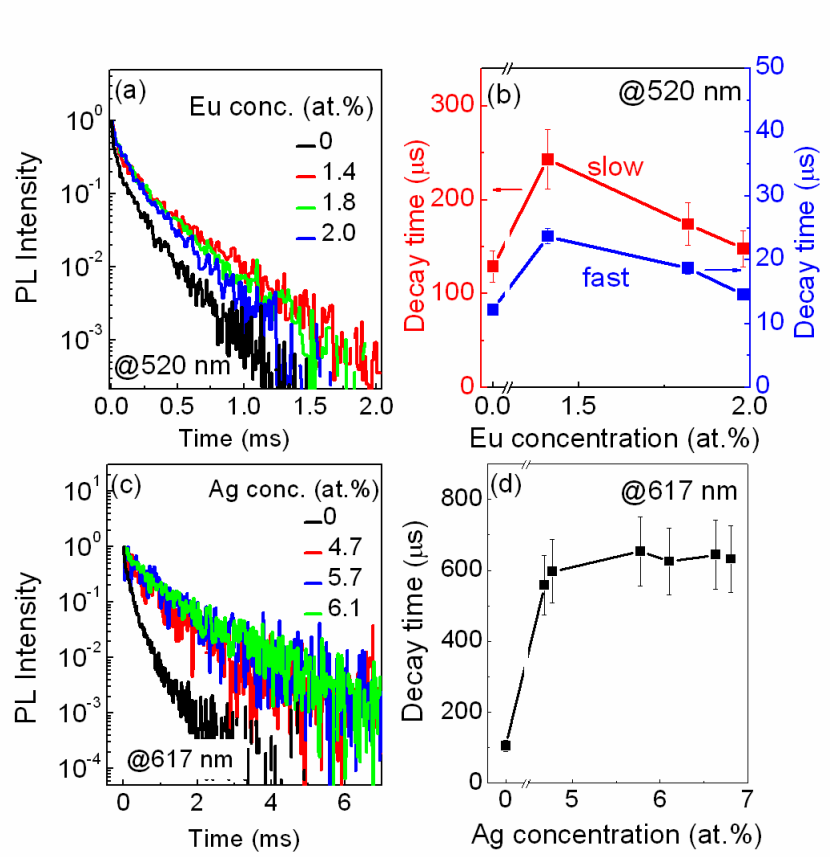

Figure 3.16: (a, c) The PL intensities as a function of delay time of zeolite:Eu,Ag with various concentration of Eu and Ag at excitation of 355 nm. (b, d) the decay time of zeolite:Eu,Ag dependence on the Eu and Ag concentration at 520 and 617 nm.

3.4 Conclusion

The effect of Ag clusters on the PL properties of Eu ions in zeolite is investigated for the first time. The appearance of a new absorption band and the increase of the PL of Eu ions for the sample containing Ag clusters are observed. Ag concentration dependence of the PL intensity revealed that the Eu-PL is increased as high as 27 times. The excitation wavelength dependence of the PL intensity coincides well with the absorption spectrum of the Ag clusters, indicating that the energy transfer from Ag clusters to Eu ions is responsible for the increase of the PL of Eu ions.

References

[1] P. Pimputkar, J. S. Speak, S.P. DenBaars, S. Nakamura, Nature Photonics **3**, 180 (2009).

[2] J. Kido, H. Shionoya, K. Nagai, Appl. Phys. Lett. **67**, 2281 (1995).

[3] P. Waltereit, O. Brandt, A. Trampert, H.T. Grahn, J. Menniger, M. Ramsteiner, M. Reiche, K.H. Ploog, Nature **406**, 865 (2000).

[4] J.J. Li, R.F. Wei, X.Y. Liu, H. Guo, Opt. Express **20**, 10122 (2012).

[5] Y. Wang, J. Tang, L. Huang, Y. Wang. Z. Huang, J. Liu, Q. Xu, W. Shen, and l. A. Belfiroe, Opt. Mater. **35**, 1395 (2013).

[6] S. Fan, C. Yu, D. He, X. Wang, L. Hu, Opt. Mater. Express **2**, 765 (2012).

[7] I. Izeddin, D. Timmerman, T. Gregorkiewicz, Phys. Rev. B **78**, 035327-1 (2008).

[8] M. Eichelbaum, K. Bademann, Adv. Funct. Mater. **19**, 1 (2009).

[9] P. Li, X.H. Sun, N.B. Wong, C.S. Lee, S.T. Lee, B. Teo, Chem. Phys. Lett. **365**, 22 (2002).

[10] S.C. Larsen, J. Phys. Chem. C **111**, 18464 (2007).

[11] L. Tosheva, V.P. Valtchev, Chem. Mater. **17**, 2494 (2005).

[12] D. Bruhwiler, C. Leiggener, S. Glaus, G. Calzaferri, J. Phys. Chem. B **106**, 3770 (2002).

[13] G.D. Gremer, E. Coutino-Gonzalez, M. B. J. Roeffaers, B. Moens, J. Ollevier, M. V. Auwerear, R. Scoonheydt, P. A. Jacobs, F. C. D. Schryver, J. Hofkens, D. E. D. Vos, B. F. Sels, T. Vosch, J. Am. Chem. Soc. **131**, 3049 (2009).

[14] M.C. Kanan, S.M. Kanan, R. Austin, H. Patterson, Environ. Sci. Technol. **37**, 2280 (2003).

[15] R. Kellerman, J. Texter, J. Chem. Phys. **70**, 1562 (1979).

[16] G. A. Ozln, and F. Hugues, J. Phys. Chem. **87**, 94 (1981).

[17] H. Sun, A. Hosokawa, Y. Miwa, F. Shimaoka, M. Fujii, M. Mizuhata, S. Hayashi, S.Deki, Adv. Mater. **21**, 3694 (2009).

[18] R. Kellerman, J. Texter, J. Chern. Phys. **70**, 1562 (1979).

[19] F. J. Berry, M. Carbucicchio, A. Chiari, C. Johnson, E. A. Moore, M. Mortimer, F. F. F. J. Vetel, J. Mater. Chem. **10**, 2131 (2000).

[20] E. Coutino-Gonzalez, M. B. J. Roeffaers, B. Dieu, G. D. Cremer, S. Leyre, P. Hanselaer, W. Fyen, B. F. Sels, and J. Hofkens, J. Phys. Chem. C **117**, 6998 (2013).

[21] G. D. Gremer, E. Coutino-Gonzalez, M. B. J. Roeffaers, D. E. D. Vos, J. Hofkens, T. Vosch, and B. F. Sels, Chem. Phys. Chem. **11**, 1627 (2010).

[22] R. Seifert, R. Rytz, and G. Calzaferri, J. Phys. Chem. A **104**, 7473 (2000).

[23] G. Calzaferri, C. Leiggener, S. Glaus, D. Schurch, and K. Kuge, Chem. Soc. Rev. **32**, 29 (2003).

[24] R. Kellerman et al., J. Chem. Phys. **70**, 1562 (1979).
[25] I. S. Lee, H. Suzuki, K. Ito, Y. Yasuda, J. Phys. Chem. B **108**, 19368 (2004).
[26] K.A. Bogle, S.D. Dhole, V.N. Bhoraskar, Nanotechnology **17**, 3204 (2006).
[27] A. Mech, A. Monguzzi, F. Cucinotta, F. Meinard, J. Mezyk, L.D. Cola, R. T ubino, Phys. Chem. Chem. Phys. **13**, 5605 (2011).
[28] G.L. Green, T.C. O'Haver, Anal. Chem. **46**, 2191 (1974).
[29] M. Puchalska, E. Zych, Journal of luminescence **132**, 2879 (2012).
[30] J. Yang, Z. Quan, D. Kong, X. Liu, J. Liu, Crystal Growth & Design **7**, 730 (2007).
[31] G. D. Cremer, Y. Antoku, M. B. J. Roeffaers, M. Sliwa, J. V. Noyen, S. Smout, J. Hofkens, D. E. D. Vos, B. F. Sels, and T. Vosch, Angew. Chem. **120**, 2855 (2008).

Chapter 4

Enhanced red photoluminescence of Sm ions in zeolite A by interaction with Ag ions

In this chapter, photosensitization of samarium (Sm^{3+}) ions by silver (Ag) ions is studied by simultaneously doping Sm and Ag in zeolite A cages. Photoluminescence (PL) from the $^4G_{2/5} \rightarrow {}^6H_{2/7}$ transition of Sm^{3+} ions at 600 nm is found to be more than 30 times enhanced by the presence of Ag ions. The excitation wavelength dependence of the PL intensity coincided well with the absorption spectra of Ag ions in the ultraviolet region, indicating that Sm^{3+} ions are excited by the energy transfer from Ag ions.

4.1 Introduction

As an important lighting source, light-emitting diodes (LEDs) have been widely used in many commodities such as backlights, device indicators, automobile headlights, displays, and so on [1-3]. Recently, an ultraviolet (UV) LED chip combined with red, green and blue phosphors have attracted much attention due to their wide range of color temperature tenability [4-5]. Rare-earth (RE) ions are practically used in phosphor materials for LEDs [6,7]. Among them, trivalent samarium ion (Sm^{3+}) is a preferable choice for red emitting phosphors [8,9]. However, the optical absorption of Sm^{3+} is very weak due to the forbidden nature of intra 4f transition. Thus it cannot be efficiently excited by UV LEDs [10].

Recently, RE ions coupled with silver nanoparticles (NPs) have been widely investigated. It is generally accepted that sensitized luminescence occurs due to the local surface plasmon resonance effect of Ag NPs. The resonant wavelength is around 400 nm, depending on the size and the dielectric constant of surrounding materials [11]. On the other hand, Eichelbaum et al. [12] reported that PL of RE ions in silicate glasses can be significantly enhanced by Ag clusters precipitated by synchrotron X-ray irradiation. The enhancement was found to be

caused by energy transfer from Ag clusters to RE ions. The excitation and emission bands are located in the UV (325-375 nm) and bluish-green (450-700 nm) regions, respectively. It has been also reported that, in oxyflouride glass, doping of Ag ions (Ag^{+}) can greatly enhance the PL of RE ions, due to the energy transfer from Ag^{+} to RE ions. The significant enhancement was observed under the excitation in the UV region. RE ions coupled with Ag species such as Ag particles, Ag clusters, and Ag ions are very promising for the realization of UV LED based white light sources which possess a wide range of color temperature tenability [13].

Zeolites are very promising host materials due to their cage structure, which enables doping of luminescent ions by a simple ion exchange process. The cage consists of orthosilicate ion (SiO_4^{4-}) and orthoaluminate ion (AlO_4^{5-}) structural units with low vibration quanta [14,15], and it is optically transparent from UV to near infrared regions [16,17]. In addition, various Ag species such as Ag nanoparticles, Ag clusters, and Ag ions can be easily stabilized in the cages [18-20]. Therefore, zeolite is a promising host material to realize efficient coupling between Ag species and luminescent ions. In this chapter, the effect of Ag^{+} on the PL properties of Sm^{3+} in zeolite A is investigated. It is shown show that the PL of Sm^{3+} in the visible region can be significantly enhanced by Ag^{+} under the excitation in the UV region. The results suggest that the metal ions doped zeolite A is very promising as phosphor materials for UV LEDs.

4.2 Experimental details

Sm and Ag doped zeolite is prepared by an ion exchange process. Sodium (Na) form of LTA zeolite (zeolite A, SiO_2/Al_2O_3 = 1) is purchased from Tosoh Co. Japan. The zeolite is stirred in the aqueous solution of $SmCl_3.6H_2O$ at room temperature for 24 h. The products are filtered, washed with de-ionized water, and dried in air at 80 ^{o}C. Sm doped zeolite (zeolite:Sm) is annealed in air at 600 ^{o}C for 2 h. For Ag doping, Zeolite:Sm is stirred in aqueous solution of Ag $(NO)_3$ at 40 ^{o}C. After 5 h stirring, Sm and Ag codoped zeolite (zeolite:Sm,Ag) is filtered, washed and dried in air at 80 ^{o}C. The sample preparation process was illustrated in Figure 4.1. It is possible for Sm ions to migrate into the sodalite cages by annealing the sample at 600 ^{o}C. The Ag ions are most possible to locate in supercage after ion exchanging [21,22]. As a reference sample, Ag singly doped zeolite (zeolite:Ag) is also prepared. In Ag and Sm codoped sample, the concentration of Ag is varied from 0.5 to 1.2 at.% and that of Sm is fixed to about 2.0 at.%, with respect to the total amount of atoms. These values are determined by X-ray photoelectron spectroscopy measurements [23,24]. PL spectra are measured by a spectrofluorometer (Horiba Jobin Yvon, Flourolog). The diffuse reflectance spectra are measured by a spectrophotometer equipped with an integrating sphere (Shimadzu, Solid Spec-3700). Time resolved PL spectra are measured using a

monochromator equipped with a charge-coupled device with an image intensifier (ICCD) (Princeton Instrument, PI-Max). Third harmonic of a Nd:YAG laser (355 nm, pulse width 5 ns, repetition frequency 20 Hz) and a modulated light (405 nm) of a laser diode are used as excitation sources for time resolved PL measurements. The ICCD array is gated by a trigger signal from the exciting lasers. For these optical measurements, the powder is packed in a sample holder loosely. All the measurements are carried out at room temperature.

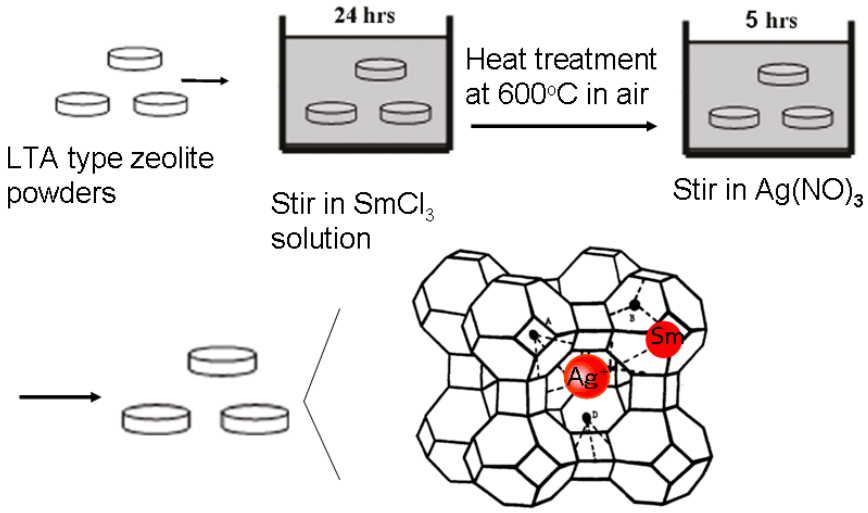

Figure 4.1: Schematic of the sample preparation procedures.

4.3 Results and discussion

4.3.1 Ag singly doped zeolite A

Figure 4.2 shows the diffuse reflectance spectra plotted as the Kubelka-Munk function (F) of the reflectance (R) of zeolite:Ag without annealing steps. Ag concentration is changed from 1.1 to 13.9 at.%. As shown in Figure 4.2(a), the without annealed samples have a UV absorption blow 320 nm. Similar absorption has been observed in numerous reports on Ag doped hydrated zeolite A. Generally it is attributed to a charge transfer transition from Ag^+ coordinated water molecules to the empty 5s state of Ag^+ [18, 23]. The enlarged spectra are shown in the inset of the Figure. The weak absorption at about 370 nm is observed in some high concentration samples. It may form Ag cluster by increasing the Ag concentration. The Ag concentration dependence on the absorbance F(R) intensity at 280 nm is plotted in the Figure 4.2(b). With increasing Ag concentration, the absorption increases.

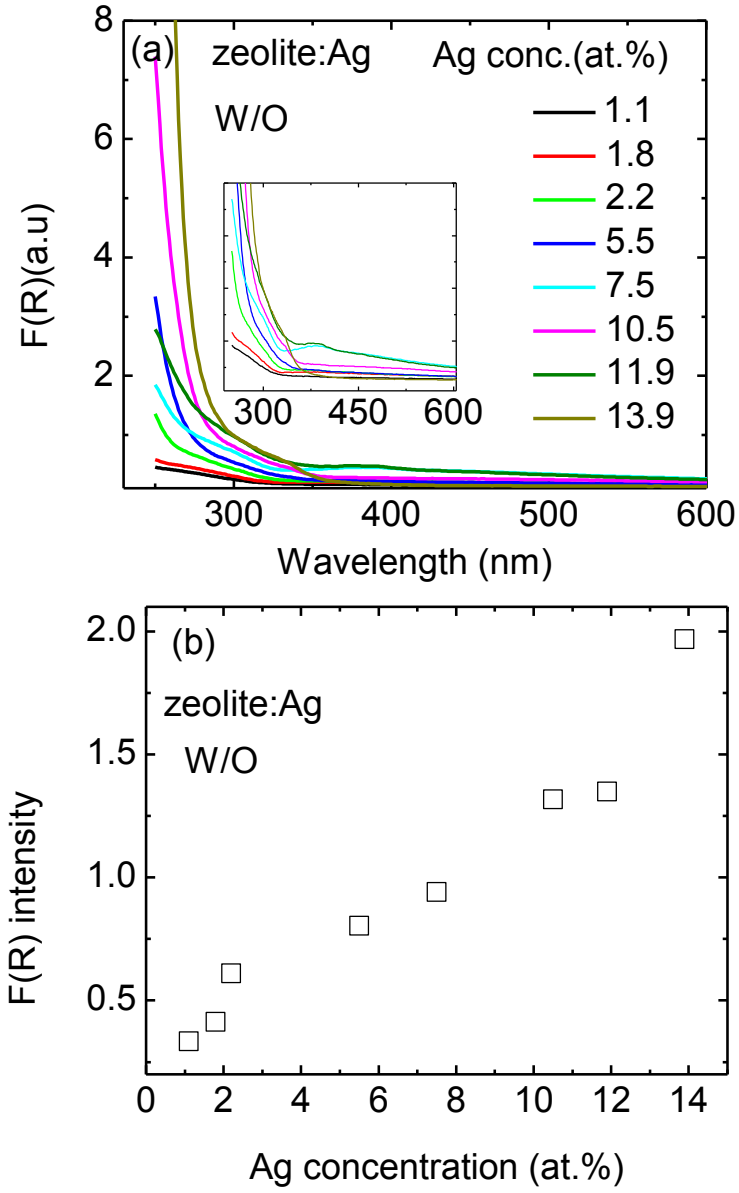

Figure 4.2:(a) Diffuse reflectance spectra plotted as the Kubelka-Munk function (F) of the reflectance (R) of without annealed zeolite:Ag with various Ag concentrations. (b) F(R) intensity plotted as a function of Ag concentration of zeolite:Ag.

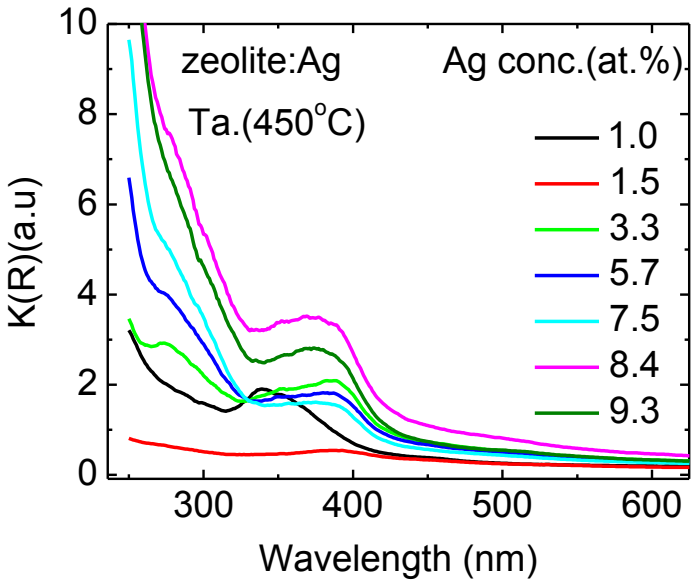

Figure 4.3: Diffuse reflectance spectra plotted as the Kubelka-Munk function (F) of the reflectance (R) of zeolite:Ag with various Ag concentrations annealed at 450 °C.

The diffuse reflectance spectra plotted as the Kubelka-Munk function (F) of the reflectance (R) of zeolite:Ag with various Ag concentration annealed at 450 °C is shown in Figure 4.3. Ag concentration is changed from 1.0 to 9.3 at.%. As shown in Figure 4.3, the zeolite:Ag shows broad absorption at longer wavelength after annealing process. The zeolite:Ag(1.0) shows absorbance at about 350 nm, and the absorption shows red shift with increasing concentration. Generally, the absorption at about 350 nm of Ag in zeolite A is ascribed to Ag trimer [25].

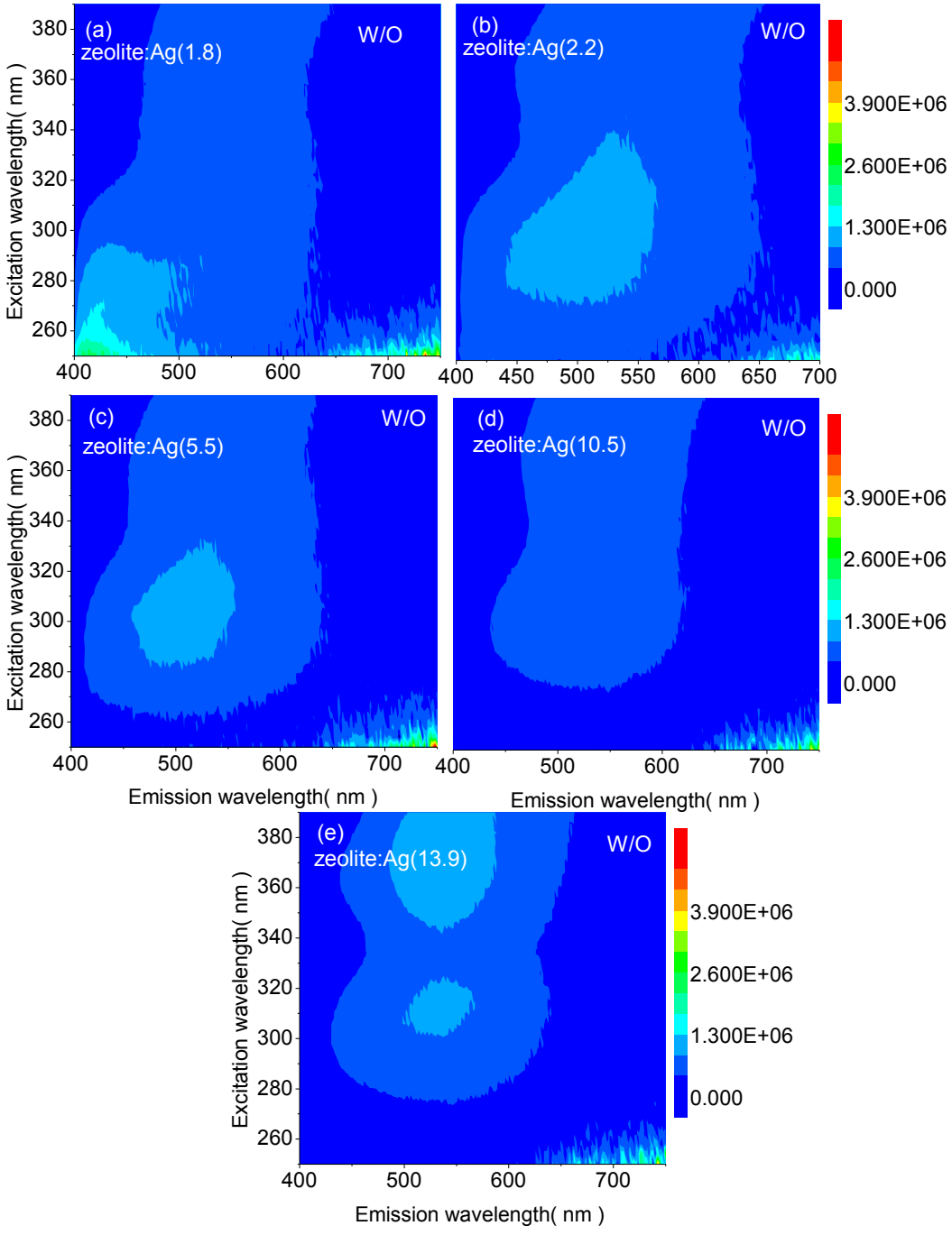

Figure 4.4: 2D emission-excitation graphs of various concentration of Ag of zeolite:Ag without annealing steps.

2D emission-excitation graphs of various concentration of Ag of zeolite:Ag under without annealing are shown in Figure 4.4. The zaolite:Ag(1.0) shows an excitation band

below 260 nm and an emission band below 450 nm. Generally, this UV excitation with an emission at low wavelength in zeolite is ascribed to Ag ions. [18,23] The excitation and emission points show red shift with increasing Ag concentration. As a result, the zeolite:Ag(13.9) shows emission at about 550 nm with excitation band peak at about 310 and 370 nm. The long wavelength excitation and emission is consistent with which in Ag cluster (trimer). But it could not be proved by these measurements.

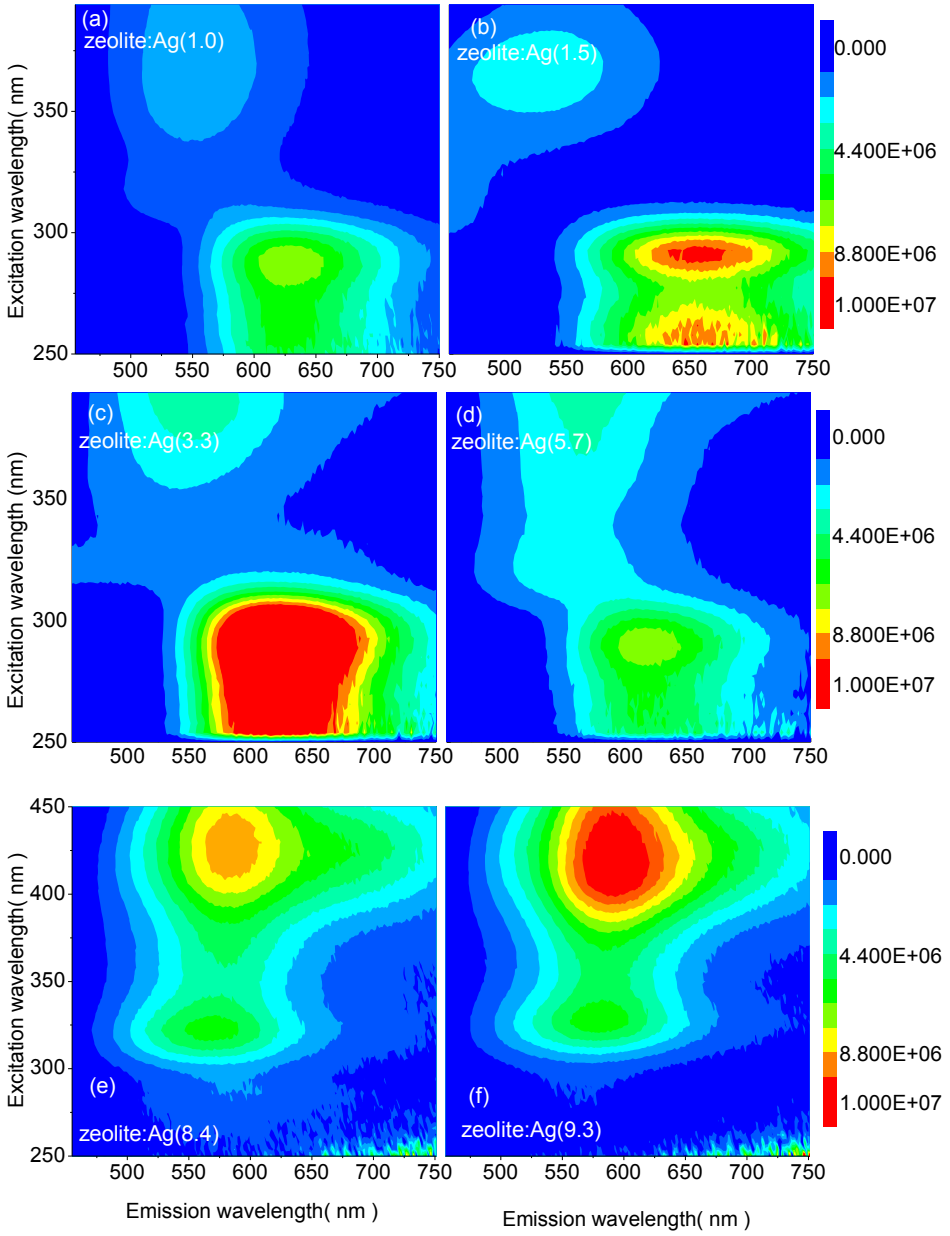

Figure 4.5: 2D emission-excitation graph of various concentration of Ag of zeolite:Ag annealed at 450°C.

Annealing the zeolite:Ag at 450 °C produced colored powders with a spectrum ranging from yellow to orange. The color turns the white and then to yellowish again, while the sample is exposed to air immediately. The first color change has been ascribed to a Ag ions coordinating to the oxygen atoms in the zeolite lattice. In the dehydrated sample, a ligand-to-metal charge transfer from the zeolite lattice to the empty 5s orbital of the Ag ion is responsible for the yellow color [19]. Under rehydration, the absorption is strongly blue-shifted, resulting in a white-looking powder. Such ionic Ag species generally shows weaker fluorescence at about 350 nm as shown in the without annealed zeolite:Ag(1.0) (Figure 4.4). On contrast, strong luminescence under low power UV excitation is observed in annealed samples (as shown in Figure 4.5). Since cluster formation has been proven in Ag exchanged zeolites upon thermal treatment, the luminescence can be ascribed to oligoatomic silver clusters [19]. Yellow and red emissions are observed in the zeolite:Ag, and intensities of the emissions strongly depend on the Ag concentration. In most cases at intermediate silver loadings, a yellow fluorescent band around 550 nm is observed with likely a Ag_3^+ cluster as representative species [26,27]. A red emission at about 630 nm with UV excitation as formed in the low Ag concentration region, which diapered in high concentration sample. Generally, for LTA zeolites at higher loadings a possible candidate species emitting around 690 nm was formed. The luminescence of the 690 nm emitter was ascribed to a Ag_6^+ cluster in the report [19]. However, the UV excitation of our sample is not consistent with the blue excitation of 690 nm emission. Thus the Ag_6^+ is probably not origin of the red emission. The positions of emission-excitation bands in zeolite:Ag with various concentration of Ag under without annealing and annealing at 450 °C are summarized in Figure 4.6. From Figure 4.6, we can see that the emission peaks are red shifted by annealing the samples. Three main emission-excitation bands shown in the samples, such as 500 nm emission with excitation of 300 nm, 550 nm emission with excitation of 370 nm, and 630 nm emission with excitation of 290 nm.

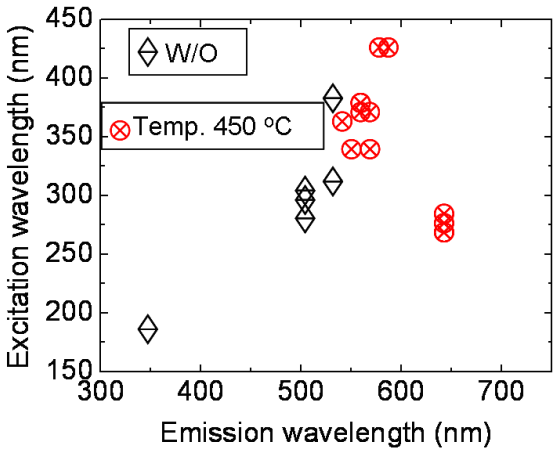

Figure 4.6: positions of emission-excitation bands in zeolite:Ag with various concentrations of Ag under annealing and without annealing steps.

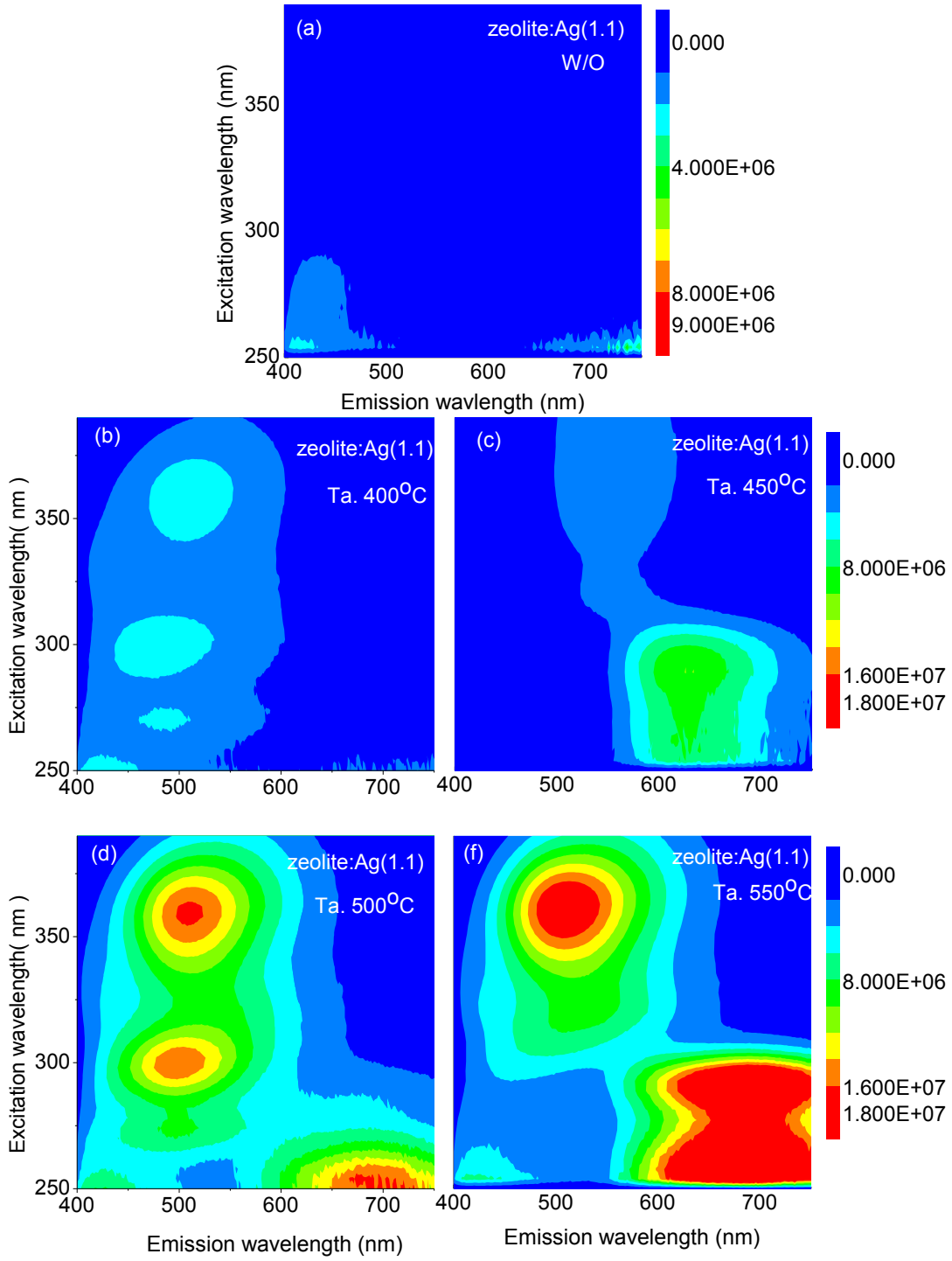

Figure 4.7: Annealing temperature dependence of 2D emission-excitation graph of zeolite:Ag (1.1).

On the other hand, the emission and excitation bands and intensities depend on the annealing temperature. As shown in the Figure 4.7, a blue emission from Ag ions is shown in the sample without annealing. After annealing, new yellow emission with few excitation bands is observed, while a red emission was shown in the high temperature annealed sample. For sensitizing RE ions, the zeolite:Ag without annealing with high energy excitation and low background luminescence is described in next work.

4.3.2 Sm and Ag singly co-doped zeolite A

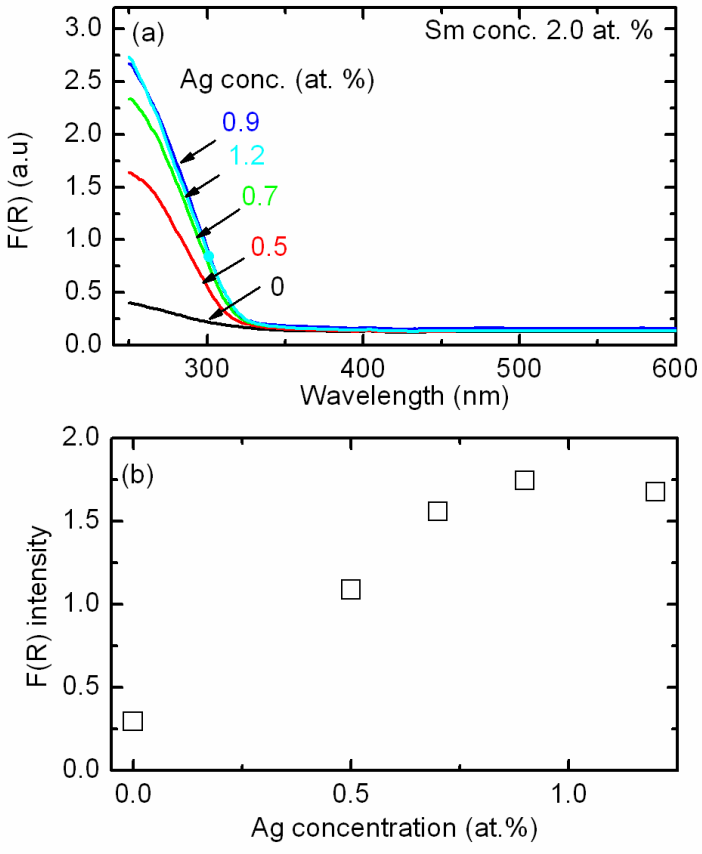

Figure 4.8: (a) Diffuse reflectance UV-visible spectra, plotted as the Kubelka-Munk function (F) of the reflectance (R) of zeolite:Sm,Ag with various Ag concentrations. (b) F(R) intensity plotted as a function of Ag concentration of zeolite:Sm,Ag.

Figure 4.8 shows the Ag concentration dependence of the diffuse reflectance spectra plotted as the Kubelka-Munk function (F) of the reflectance (R) of zeolite:Sm,Ag. With increasing Ag concentration, the absorption below 300 nm increases. Generally the absorption is attributed to a charge transfer transition from Ag^+ coordinated water molecules to the empty 5s state of Ag^+ [20, 28]. The sample without Ag doping has a weak absorption band below 300 nm. This arises from the charge transfer state (CTS) of O^{2-} to Sm^{3+} [29]. The Ag concentration dependence of the absorbance (F(R) intensity) at 280 nm is shown in Figure 4.8(b). The absorbance increases until the Ag concentration reaches 0.9 at. %, and then saturates.

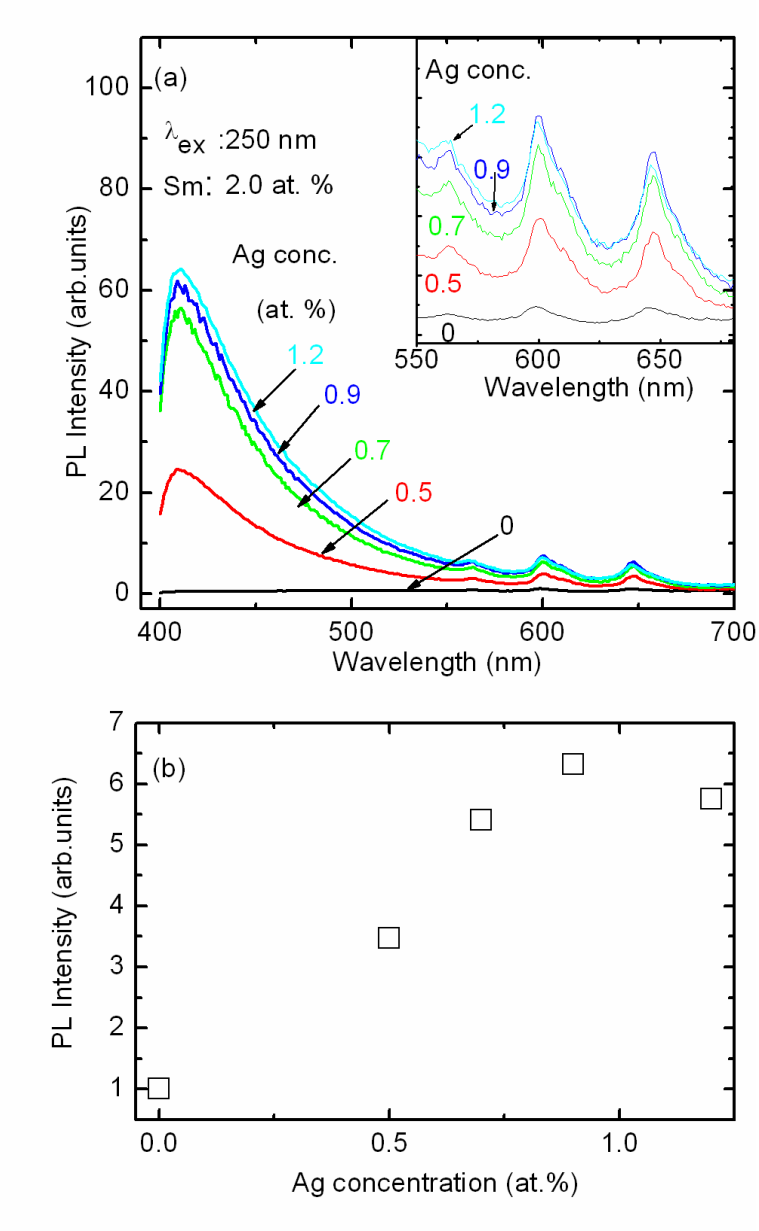

Figure 4.9: (a) PL spectra of zeolite:Sm,Ag with various Ag concentrations under the excitation of 250 nm. The inset shows the enlarged spectra of the Sm-PL. (b) Ag concentration dependence of the Sm-PL intensity.

Figure 4.9(a) shows the PL spectra of zeolite:Sm,Ag with different Ag concentrations. The excitation wavelength is 250 nm. By Ag codoping, a broad PL appears below 500 nm. Note that the decrease in the PL intensity below 410 nm is due to the long-pass filter to cut the excitation light. With increasing Ag concentration, the intensity increases. Similar PL have been reported in Ag^+ doped zeolite and glasses [30,13]. In addition to the broad PL band, we can see some small peaks at 560, 600 and 646 nm. These peeks are enlarged in the inset. These peaks arise from the $^4G_{5/2}\rightarrow{}^6H_{5/2}$, $^4G_{5/2}\rightarrow{}^6H_{7/2}$, and $^4G_{5/2}\rightarrow{}^6H_{9/2}$ transitions of Sm^{3+}, respectively [31, 32]. Hereafter, the PL from Ag and Sm are referred to as Ag-PL and Sm-PL, respectively. In the inset, we can see that the Sm-PL is significantly enhanced by the Ag codoping. Figure 4.9 (b) shows the Sm-PL intensity as a function of Ag concentration. The Sm-PL intensity is estimated by subtracting the broad Ag-PL as a background signal. The intensity is normalized to that of the sample without Ag doping. We can see that the Sm-PL is at most 6.3 times enhanced by the Ag codoping. The Ag concentration dependence of the Sm-PL intensity is very similar to that of absorbance F(R) in Figure 4.8(b). This implies that the enhancement of the Sm-PL is due to the energy transfer from Ag ions in zeolite A cages.

Figure 4.10(a) shows the PL spectra of zeolite:Ag,Sm with various Sm concentration. The excitation wavelength is 250 nm, and the Sm concentration is changed from 0 to 8.4 at.%. Figure 4.10(b) plots the Sm-PL intensity (left axis) and the Ag-PL intensity (right axis) as a function of Sm concentration. With increasing the Sm concentration, the Ag-PL intensity decreases, while the Sm-PL intensity increases, in the low Sm concentration region (< 3.8 at. %). This strongly indicates that the energy transfer is responsible for the increased Sm-PL. In the high Sm concentration region (>3.8 at. %), both the Ag-PL and Sm-PL decreases. This is probably due to concentration quenching. To clarify the effect of re-absorption of the Ag-PL, the PL spectra of zeolite:Sm,Ag and the mixture of zeolite:Sm and zeolite:Ag (zeolite:Sm / zeolite:Ag = 1 in wt%) under the excitation at 250 nm are shown in the Figure 4.11. The Sm concentration in zeolite:Sm is about 2.0 at.%, Ag concentration in zeolite:Ag is 0.5 at.%. In zeolite:Sm,Ag, concentrations of Sm and Ag are 3.8 and 0.5 at.%, respectively. We can see that the zeolite:Sm,Ag shows strong Sm-PL around 600 nm. In contrast, the Sm-PL of the mixture of zeolite:Sm and zeolite:Ag is negligibly weak. This indicates that re-absorption of the Ag-PL does not contribute to the enhancement of the Sm-PL of zeolite:Sm,Ag.

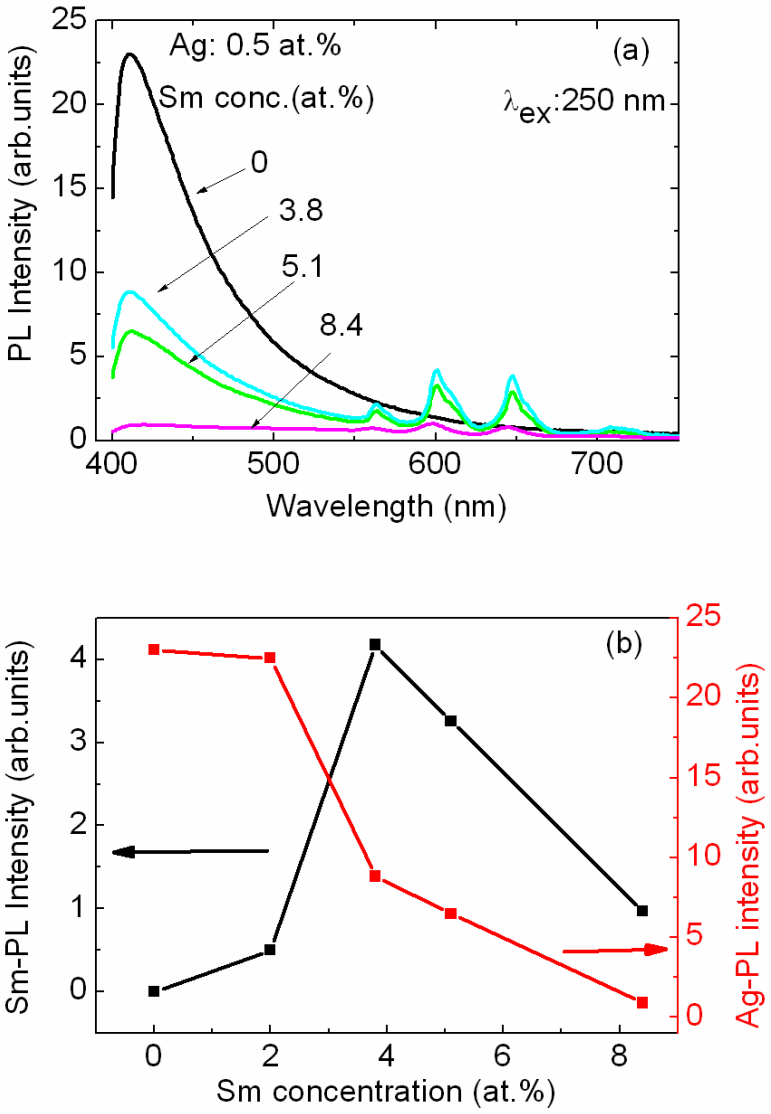

Figure 4.10: (a) PL spectra of zeolite:Sm,Ag with various Sm concentration under the excitation of 250 nm. (b) Sm concentration dependence of Sm-PL intensity (left axis) and Ag-PL intensity (right axis).

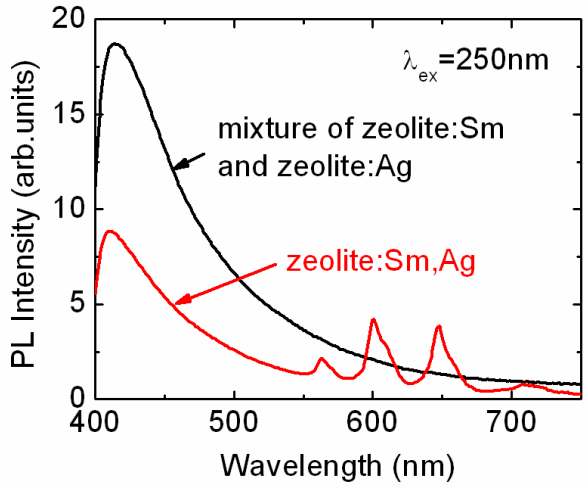

Figure 4.11: PL spectra of zeolite:Sm,Ag and the mixture of zeolite:Sm and zeolite:Ag under the excitation at 250 nm.

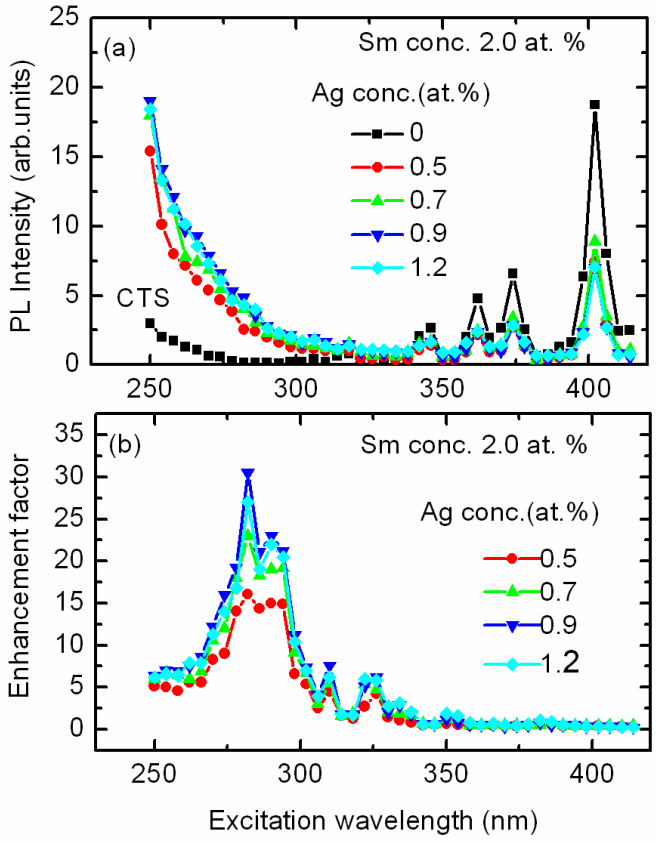

Figure 4.12: (a) PL excitation spectra of the Sm-PL of zeolite:Sm,Ag with Ag concentrations from 0 to 1.2 at.%. (b) Excitation wavelength dependence of the enhancement factor of the Sm-PL of zeolite:Sm,Ag with different Ag concentrations.

Figure 4.12(a) shows the Sm-PL intensity as a function of excitation wavelengths. The sample without Ag doping shows a broad small excitation band below 280 nm. This is due to the energy transfer from the CTS from O^{2-} to Sm^{3+}. All the samples exhibit 4 sharp peaks at 344, 361, 375, and 402 nm, arising from 4f-4f transitions of Sm^{3+} [31]. By Ag codoping, we can see that the excitation band in the UV region is significantly enhanced. In addition, compared to Figure 4.8, we can notice that the Ag concentration dependence of the excitation band is very similar to that of the absorption band. This strongly suggests that the PL enhancement is due to the energy transfer from Ag^{+} to Sm^{3+}. The Ag^{+} absorbs excitation photons more efficiently than Sm^{3+}, and transfers the excitation energy to Sm^{3+}. The simple energy transfer process was illustrated in the Figure 4.13. Under UV excitation, Ag^{+} ions are excited from ground state to excited state. An excited Ag^{+} ion relaxes from excited state to ground state nonradiatively and transfers the excitation energy to a neighboring Sm^{3+}, promoting it from ground state to excited state. After then, Sm ions in excited level relax from luminescent level to ground level radiatively and result in enhanced red luminescence. The strong enhancement of the Sm-PL indicates that the energy transfer is a dominant excitation process of Sm^{3+}. In Figure 4.12 (b), the enhancement factor defined as the ratio of the Sm-PL of zeolite:Sm,Ag to that of zeolite:Sm are shown. The enhancement factor has a peak at 282 nm and reaches as high as 30 at the maximum. The great enhancement suggests that the Ag and Sm codoped zeolite is very promising as a phosphor material. The decrease of the enhancement factor below 280 nm is due to the increased Sm-PL intensity of the sample without Ag doping by the CTS band.

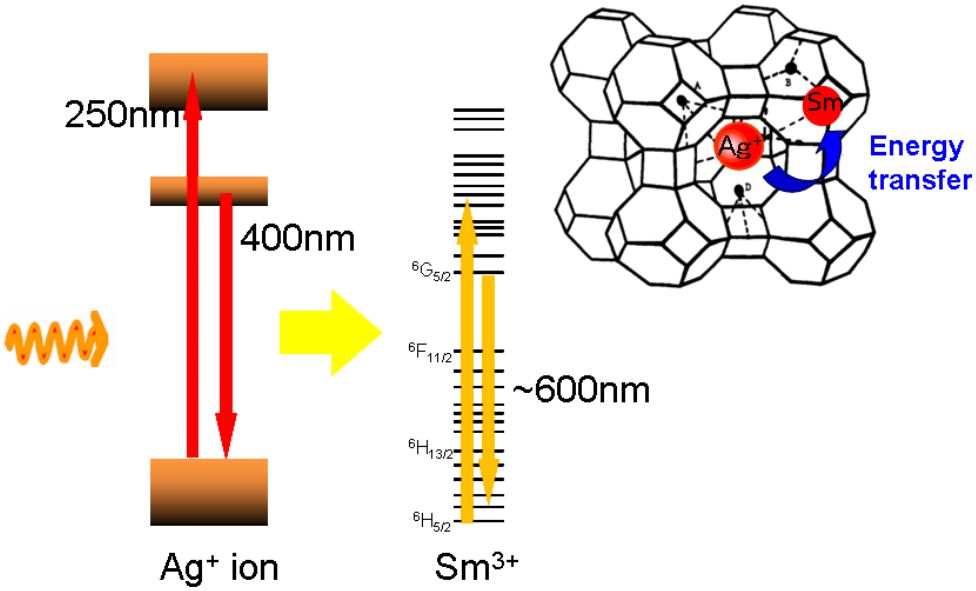

Figure 4.13: Schematic illustrations of the energy transfer process from Ag^{+} to Sm^{3+}.

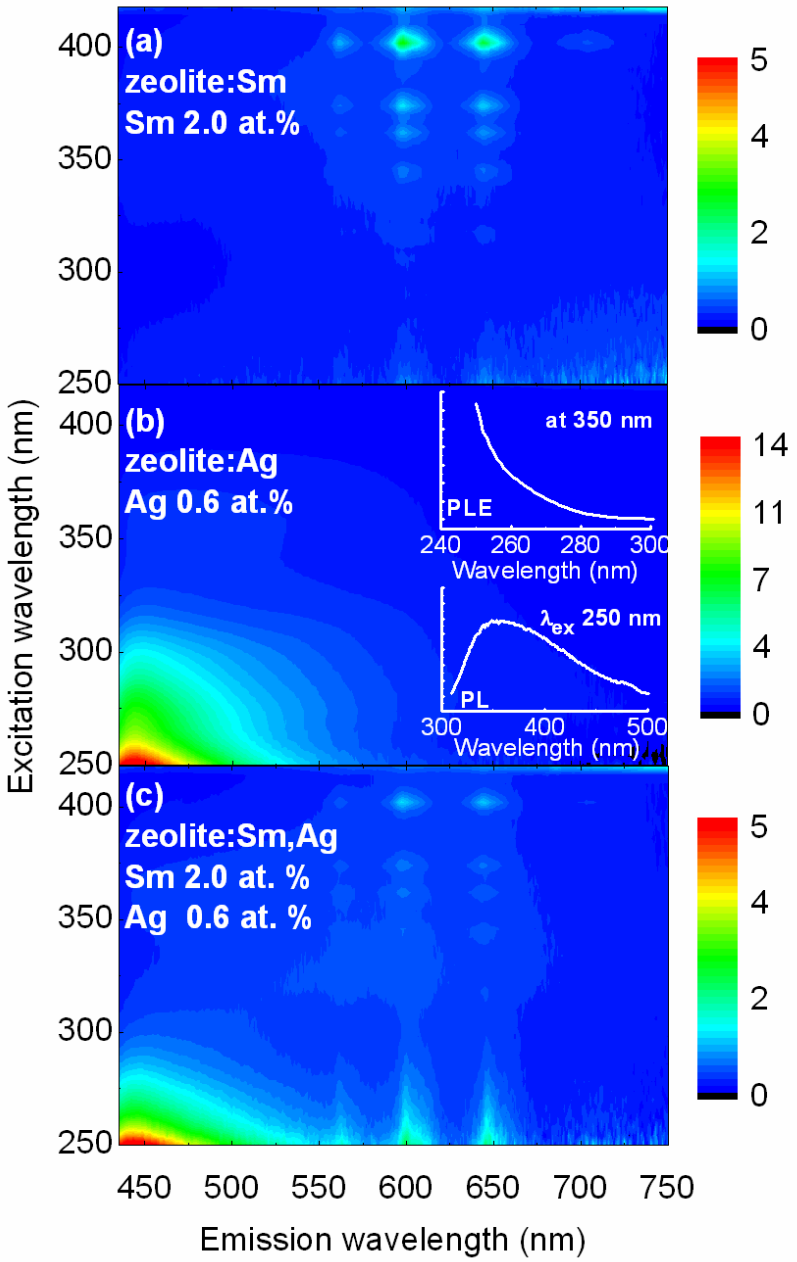

Figure 4.14: (a-c) 2D emission - excitation graphs of zeolite:Sm, zeolite:Ag and zeolite:Sm,Ag, respectively. The inset of Figure 4.11(b) shows PL excitation detected at 350 nm and PL spectra excited at 250 nm.

In order to obtain further insight on the PL properties, 2D excitation-emission measurements are performed. Figure 4.14(a)-(c) show the results of zeolite:Sm, zeolite:Ag,

and zeolite:Sm,Ag, respectively. As shown in Figure 4.14(a), zeolite:Sm possesses sharp emission peaks at 560, 600 and 646 nm under the excitation at 344, 361, 375, and 402 nm. These are related to the 4f-4f transitions of Sm^{3+}. In Figure 4.14(b), zeolite:Ag shows a broad emission below 500 nm with a broad excitation band below 300 nm. To compare this band more in detail with that in previous reports, the PL excitation (PLE) spectrum detected at 350 nm and the PL spectrum excited at 250 nm are displayed in the inset of Figure 4.14(b). The PLE spectrum exhibits a broad band around 250 nm, while the PL spectrum is around 350 nm. Very similar PLE and PL band have been reported for Ag^{+} doped zeolites and glasses [13,31,33,34]. In Figure 4.14(c), we can see the coexistence of both the excitation-emission bands arising from Sm^{3+} and Ag^{+}. This suggests that the codoping of Sm^{3+} does not significantly affect the chemical state of Ag^{+}. By comparing Figure 4.14(a) and 4.14(c), we can notice that the Sm-PL is significantly enhanced when the excitation wavelength is below 300 nm.

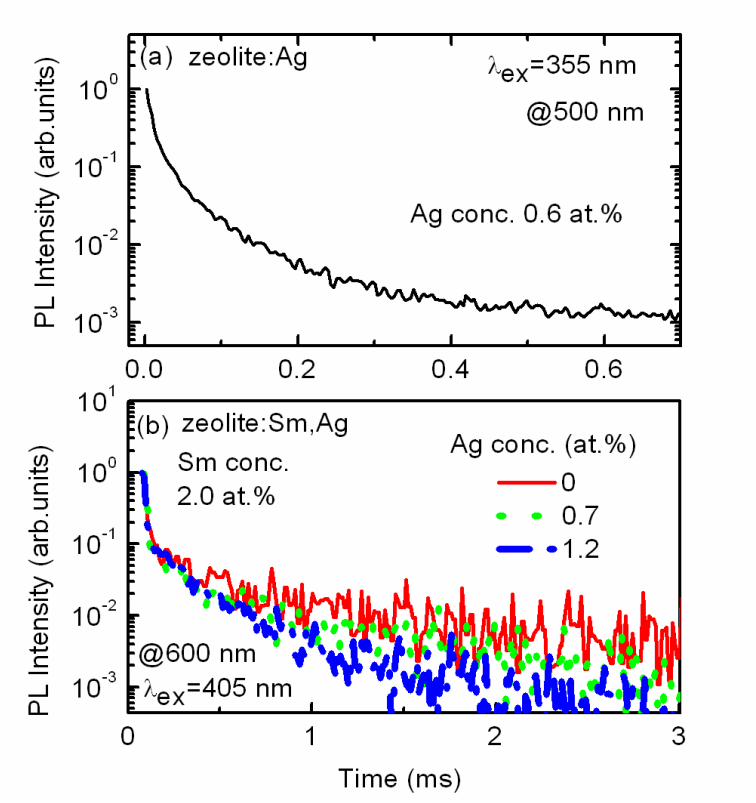

Figure 4.15: (a) PL decay curves of zeolite:Ag at 500 nm under the excitation at 355 nm. (b) PL decay curves of zeolite:Sm,Ag with different Ag concentrations, detected at 600 nm under the excitation of 405 nm.

To draw more information of the PL properties, time resolved PL measurements are performed. Figure 4.15(a) shows a PL decay curve of zeolite:Ag detected at 500 nm under the excitation of 355 nm. The decay curves of the sample is multi-exponential decay, and the mean lifetime can be calculated by equation of $\int_{t0}^{\infty}[I(t)I_0]d(t)$, where *I(t)* is the luminescence intensity as a function of time *t*. the mean lifetime of Ag in zeolite:Ag is 16 μs, which is comparable to that observed for Ag^+ in glasses [34]. This confirms that Ag^+ is responsible for the broad PL in the UV region. Figure 4.15 (b) shows the decay curve of Sm-PL of zeolite:Sm,Ag with different Ag concentrations. The Sm-PL are detected at 600 nm and excited at 405 nm. Note that the Ag^+ does not show PL under this excitation wavelength (see Figure 4.14(b)). The PL decay curves consist of two components, i.e., fast and slow. The lifetime of the fast component is shorter than 10 μs. This does not depend on the Ag concentration. The fast component probably arises from oxygen-vacancies in zeolites [35]. On the other hand, the lifetime of the slow component clearly depends on the Ag concentration. It decreases from 1.6 to 0.7 ms with increasing Ag concentration. This implies that the internal quantum efficiency of the Sm-PL may decrease by the Ag codoping. The detailed mechanism of the shortened lifetime is not clear at present and further discussion will be conducted in the future work.

4.4 Conclusions

In conclusion, the effect of Ag^+ on the PL properties of Sm^{3+} in zeolite A is investigated for the first time. The Sm -PL intensity is more than 30 times enhanced by the Ag codoping. The PLE spectrum detecting the Sm-PL coincides well with the absorption spectrum of Ag^+, indicating that energy transfer from Ag^+ to Sm^{3+} is responsible for the enhancement of the Sm-PL.

Reference

[1] C. Guo, J. Yu, X. Ding, M. Li, Z. Ren, and J. Bai: J. Electrochem. Soc. **158**, J42 (2011).

[2] H. Guo, X. Wang, J. Chen, and F. Li: Opt. Express **18**, 18900 (2010).

[3] H. Y. Chung, C. H. Lu, and C. H. Hsu: J. Am. Ceram. Soc. **93**, 1838 (2010).

[4] S. Kato, T. Fukuda, S. Akiyama, Z. Honda, N. Kamada, and N. Kijima: Jpn. J. Appl. Phys. **50**, 01BF02 (2011).

[5] H. S. Jang, and D. Y. Jeon: Opt. Lett. **32**, 3444 (2007).

[6] H. Guo, H. Zhang, R. Wei, M. Zheng, and L. Zhang: Opt. Express **19**, A201 (2011).

[7] C. Ming, F. Song, C. Li, Y. Yu, G. Zhang, H. Yu, T. Sun, and J. Tian: Opt. Lett. **36**, 2242 (2011).

[8] B. An, M. Gong, M. Li, and J. Zhang: Journal of Molecular Structure **687**, 1 (2004).

[9] C. Koughia, A. Edgar, C. R. Varoy, G. Okada, H. von Seggern, G. Belev, C. Kim, R. Sammynaiken, and S. Kasap: J. Am. Caram. Soc. **94**, 543 (2011).

[10] X. He, J. Zhou, N. Lian, J. Sun, M. Guan: Journal of luminescence **130**, 743 (2010).

[11] A. Pillonnet, A. Berthelot, A. Pereira, O. Benamara, S. Derom, G. Colas des Francs, and A. M. Jurdyc: Appl. Phys. Lett. **100**, 153115 (2012).

[12] M. Eichelbaum, and K. Bademann: Adv. Funct. Mater. **19**, 1 (2009).

[13] S. Paje, M. García, J. Llopis, and M. Villegas: J. Non-Cryst. Solids **318**, 239 (2003).

[14] P. Li, X. H. Sun, N. B. Wong, C. S. Lee, S. T. Lee, and B. Teo: Chem. Phys. Lett. **365**, 22 (2002).

[15] M. Ryo, Y. Wada, T. Okubo, T. Nakazawa, Y. Hasegawa, and S. Yanagida: J. Mater. Chem. **12**, 1748 (2002).

[16] M. Flores-Acosta, R. Perez-Salas, R. Aceves, M. Sotelo- Lerma, and R. Ramirez-Bon: Solid State Commun. **136**, 567 (2005).

[17] H. Sun, A. Hosokawa, Y. Miwa, F. Shimaoka, M. Fujii, M. Mizuhata, S. Hayashi, and S. Deki: Adv. Mater. **21**, 3694 (2009).

[18] J. Talebi, R. Halladj, and S. Askari: J. Mater. Sci. **45**, 3318 (2010).

[19] G. D. Gremer, E. Coutino-Gonzalez, M. B. J. Roeffaers, B. Moens, J. Ollevier, M. V. Auwerear, R. Scoonheydt, P. A. Jacobs, F. C. D. Schryver, J. Hofkens, D. E. D. Vos, B. F. Sels, and T. Vosch: J. Am. Chem. Soc. **131**, 3049 (2009).

[20] R. Seifert, R. Rytz, and G. Calzaferri: J. Phys. Chem. A **104**, 7473 (2000).

[21] F. J. Berry, M. Carbucicchio, A. Chiari, C. Johnson, E. A. Moore, M. Mortimer, F. F. F. J. Vetel, J. Mater. Chem. **10**, 2131 (2000).

[22] M. F. Hazenkamp, A. M. H. van der Veen, N. Feiken and G. Blasse, J. Chem. Soc. Faraday Trans., **88**, 141 (1992).

[23] A. F. Carley and M. W. Roberts: Proc. R. Soc. Lond. A **363**, 403 (1978).

[24] C. Viornery, Y. Chevolot, D. Leonard, B. Anonsson, P. Pechy, H. J. Mathieu, P. Descouts, and M. Cratzel: Langmuir **18**, 2582 (2002).

[25] J. Michalik and L. Kevan, J. Am. Chem. Soc. **108**, 4247 (1986).

[26] L. R. Gellens, W. J. Mortier, R. A. Schoonheydt, J. B. Uytterhoeven, J. Phys. Chem. **85**, 2783 (1981).

[27] L. R. Gellens, W. J. Mortier, J. B. Uytterhoeven, Zeolites, **1**, 11 (1981).

[28] G. Calzaferri, C. Leiggener, S. Glaus, D. Schurch, and K. Kuge: Chem. Soc. Rev. **32**, 29 (2003).

[29] B. Lei, Y. Liu, G. Tang: Mater. Chem. Phys. **87**, 227 (2004).

[30] J. Texter: Phys. Rev. B **23**, 4407 (1981).

[31] Y. Sun, X. Gu, F. Ding, P. F. Smet, E. Gao, D. Poelman, and F. Verpoort: crystal growth & design **10**, 1059 (2010).

[32] B. J. Chen, L. F. Shen, E. Y. B. Pun, and H. Lin: Opt. Express **20**, 879 (2012).

[33] E. Borsella, G. Battaglin, M. A. García, F. Gonella, P. Mazzoldi, R. Polloni, and A. Quaranta: Appl. Phys. A. **71**, 125 (2000).

[34] J. Li, R. Wei, X. Liu, and H. Guo: Opt. Express **20**, 10122 (2012).

[35] A. Mech, A. Monguzzi, F. Cucinotta, F. Meinard, J. Mezyk, L. D. Cola, and R. Tubino: Phys. Chem. Chem. Phys. **13**, 5605 (2011).

Chapter 5

Conclusions

In this thesis, the luminescence properties of Bi doped oxidized porous Si and photosensitizations of rare earth ions by Ag clusters/ions in zeolites are studied. The broadband and strong NIR emission of Bi doped oxidized porous Si covers the whole telecommunication wavelengths. The thin film has potential applications in optical communication. The enhanced red emission of RE ions in the nanostructured powder shows potential application in white LED.

In chapter 2, luminescence properties of Bi doped oxidized porous Si thin films are studied for the first time. The sample is prepared by a solution-based method, consisting of conventional anodizing etching of Si wafer and dip coating. It is found that this material shows two broad luminescence bands centered at 845 nm with the FWHM of 120 nm and at 1410 nm with the FWHM of 220 nm under 488 nm excitation. The NIR PL spectra depend on the Bi concentration and oxidation temperature. The oxidation temperature dependence of PL intensity revealed that oxidation of silicon into silica is indispensable to activate the Bi NIR active centers in oxidized porous Si. PL properties of Bi doped porous silica thin films annealed at various temperatures and in different atmospheres are studied. The NIR luminescence depends strongly on the annealing atmosphere and temperature. Annealing in N_2 at high temperature is necessary for the NIR luminescence. To reveal the origin of the NIR luminescence, comprehensive PL studies including steady state and time-resolved PL measurements at 8-300 K in wide excitation (250-500 nm) and detection (400-1550 nm) wavelength ranges are performed. The samples also show visible orange and red luminescence from Bi. Very small temperature dependence of PL intensity and life time is observed in the Bi doped porous silica. The PL and PL excitation measurements indicate that multiple Bi luminescence centers, such as Bi^{3+}, Bi^{2+}, Bi^{+}, and Bi dimer, are stabilized in porous silica.

In chapter 3, photosensitization of Eu^{3+} ions by Ag clusters is achieved by simultaneously doping Eu^{3+} and Ag in zeolite cages. The Eu^{3+} and Ag doped zeolite is prepared by ion exchange method. Ag cluster is formed by thermally annealed in air at low temperatures. The

absorption and emission-excitation graphs of Ag singly doped zeolite Y are also shown. The emission-excitation graphs indicate that the emission-excitation band positions of Ag cluster do not depend on the concentration of Ag and annealing temperature. A broad absorption around 450 nm is observed in high Ag concentration sample, the FE-SEM image prove that the absorption is responsible to Ag NPs. In the Eu^{3+} and Ag co-doped sample, the PL due to the Eu^{3+}: $^5D_0 \rightarrow {}^7F_2$ transition of ions at 613 nm is significantly increased by the presence of Ag clusters. The enhancement can be tuned by Ag concentration; Eu-PL is at most 27 times increased by co-doping Ag. The excitation wavelength dependence of the PL intensity coincided well with the absorption spectrum of Ag clusters, indicating that Eu ions are excited by the energy transfer from Ag clusters.

In chapter 4, the effect of Ag^+ on the PL properties of Sm^{3+} in zeolite A is investigated. The absorption and emission-excitation graphs of Ag singly doped zeolite are also studied. It is indicated that the samples without annealing show absorption blow 320 nm due to Ag ions in zeolite. New absorption bands appeared in the annealed samples, which are probably due to formation of Ag cluster under thermal oxidation. The Ag concentration and annealing temperature dependence of emission-excitation graphs of Ag singly doped samples are shown in the thesis, which indicates that emission-excitation graphs strongly depend on the Ag concentration and annealing temperature. To sensitize the RE ions, the Sm^{3+} and Ag are simultaneously doped in zeolite A. In the Sm^{3+} and Ag co-doped samples, the PL from Sm^{3+} at about 600 nm is significantly enhanced by the presence of Ag ions. The enhancement increases with increasing Ag concentration. The Sm -PL intensity is enhanced by more than 30 times by the Ag codoping without further annealing steps. The concentration dependence of PL in codoped samples suggests that the enhancement can be optimized by adjusting Ag and Sm concentrations. The excitation wavelength dependence of the Sm-PL coincides well with the absorption spectrum of Ag^+, indicating that energy transfer from Ag^+ to Sm^{3+} is responsible for the enhancement of the Sm-PL.

Acknowledgment

First I would like to thank my supervisor Professor Minoru Fujii, for giving me the opportunity to undertake a PhD study and for their outstanding help and guidance. The discussions and comments at our weekly seminars were always very inspiring and they were the breeding ground to develop many new ideas. I would like to express my thanks to Dr. Kenji Imakita for his fruitful discussions and guidance on my study.

I wish to express my deep acknowledgment to Professor Shinji Hayashi for his insightful comments and good advice. I also would like to thank Professor Takashi Kita and Minoru Mizuhata, for their careful reading and valuable comments on this thesis.

This work has been done at Mesoscopic Materials Laboratory, Department of Electrical and Electronics Engineering, Faculty of Engineering, Kobe University under the direction of Professor Minoru Fujii. I am also grateful to my co-workers in the laboratory, particularly, to Dr. Zhenhua Bai, Mr. Shinsuke Shichi and Koki Omote, for their excellent technical assistance on the study of the optical measurements and discussions. I also thank all colleagues in the Mesoscopic Materials Laboratory. I would like to express my thanks to Dr. Hui Lin for his careful reading on this thesis.

Finally, I am grateful to my parents, to my husband, to my sisters, and to all my friends. Without their continuous love and support, this work would not have been possible.

List of Publications

1. **Sa chu rong gui**, Kenji Imakita , Minoru Fujii, Zhenhua Bai, Shinji Hayashi "Luminescence properties of Bi-doped oxidized porous silicon thin films"
   Optical Materials, Vol. 34, pp.1161-1164 (2012).
   Chapter 2

2. **Sa chu rong gui**, Kenji Imakita , Minoru Fujii, Zhenhua Bai, Shinji Hayashi "Near infrared photoluminescence from bismuth-doped nanoporous silica thin films"
   Journal of Applied Physics, Vol. 114, pp. 033524-1-033524-5 (2013).
   Chapter 2

3. **Sa chu rong gui**, Kenji Imakita , Minoru Fujii, Shinji Hayashi
   "Photosensitization of europium ions by silver clusters in zeolite"
   Optical Materials, (2013) (In press)
   Chapter 3

4. **Sa chu rong gui**, Kenji Imakita , Minoru Fujii, Shinji Hayashi
   "Enhanced red photoluminescence of samarium in zeolite A by interaction with silver ions"
   Japanese Journal of Applied Physics, (2013) (In press)
   Chapter 4

Articles to which the author also contributed

1. Hong-Tao Sun,Tetsu Yonezawa, Miriam M. Gillett-Kunnath, Yoshio Sakka, Naoto Shirahata, **Sa Chu Rong Gui**, Minoru Fujii, and Slavi C. Sevov
   "Ultra-broad near-infrared photoluminescence from crystalline (K-crypt)$_2$Bi$_2$ containing $[Bi_2]^{2-}$ dimers"
   Journal of Materials Chemistry, Vol. 22, pp. 20175-20178 (2012)

2. Jiajia Zhou, Naoto Shirahata, Hong-Tao Sun, Batu Ghosh, Makoto Ogawara, Yu Teng, Shifeng Zhou, **Rong Gui Sa Chu**, Minoru Fujii, and Jianrong Qiu
   "Efficient dual-modal NIR-to-NIR emission of rare rarth ions codoped nanocrystals for biological fluorescence imaging"
   The Journal of Physical Chemistry Letters, Vol. 4, pp. 402-408 (2013)

3. Hui Lin, **Sa Chu Rong Gui**, Kenji Imakita, Minoru Fujii, and Shinji Hayashi
   "Strong near infrared emission enhancement in the Nd^{3+} doped zeolites Y with silver as a dehydration catalyst"
   Journal of Applied Physics, (2013) (In press)

4. Zhenhua Bai, Hui Lin, Jesse Johnson, **Sa chu rong gui**, Kenji Imakita, Reza Montazami, Minoru Fujii, and Nastaran Hashemi
   "Single-band red upconversion luminescence from morphology and size controllable Er^{3+}/Yb^{3+} doped MnF_2 nanostructures"
   Journal of Materials Chemistry C, 2013 (In press)